Simulation Studies on the New Small Wheel Shielding of the ATLAS Experiment and Design and Construction of a Test Facility for Gaseous Detectors

Dissertation zur Erlangung des
naturwissenschaftlichen Doktorgrades
der Julius-Maximilians-Universität Würzburg

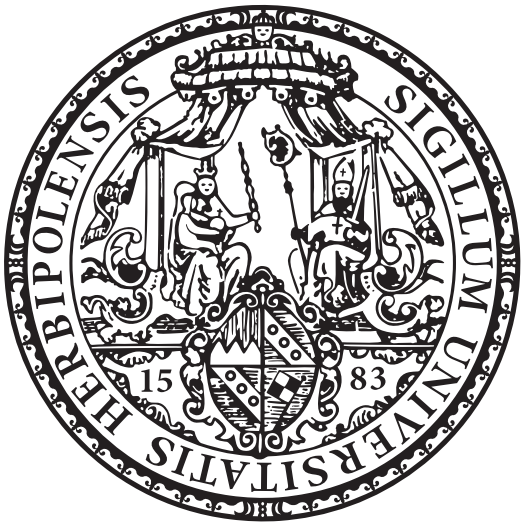

vorgelegt von

Stefan Weber
aus Freiburg im Breisgau

Würzburg, 2016

Eingereicht am 15.02.2016
bei der Fakultät für Physik und Astronomie

1. Gutachter: Prof. Dr. Raimund Ströhmer
2. Gutachter: Prof. Dr. Matthias Schott,
Johannes Gutenberg-Universität Mainz
der Dissertation

Vorsitzender: Prof. Dr. Karl Mannheim

1. Prüfer: Prof. Dr. Raimund Ströhmer
2. Prüfer: Prof. Dr. Matthias Schott,
Johannes Gutenberg-Universität Mainz
3. Prüfer: Prof. Dr. Werner Porod
im Promotionskolloquium

Tag des Promotionskolloquiums: 27.04.2016

Abstract

In this thesis two main projects are presented, both aiming at the overall goal of particle detector development. In the first part of the thesis detailed shielding studies are discussed, focused on the shielding section of the planned *New Small Wheel* as part of the *ATLAS* detector upgrade. Those studies supported the discussions within the upgrade community and decisions made on the final design of the *New Small Wheel*. The second part of the thesis covers the design, construction and functional demonstration of a test facility for gaseous detectors at the University of Würzburg. Additional studies on the trigger system of the facility are presented. Especially the precision and reliability of reference timing signals were investigated.

Kurzdarstellung

In dieser Arbeit werden zwei Projekte vorgestellt, welche beide das gemeinsame Ziel der Entwicklung von Teilchendetektoren verfolgen. Im ersten Teil der Arbeit werden ausführliche Simulationsstudien zur Abschirmung behandelt, die sich auf die Abschirmungsbereiche des geplanten *New Small Wheels* als Teil der *ATLAS*-Detektor Verbesserungen konzentrieren. Diese Studien unterstützten die Diskussionen innerhalb der Upgrade-Gemeinschaft und Entscheidungen, welche für die endgültige Kostruktionsplanung des *New Small Wheels* getroffen wurden. Der zweite Teil der Arbeit umfasst die Konstruktion, den Aufbau sowie den Funktionsnachweis eines Teststandes für Gasdetektoren an der Universität Würzburg. Ebenfalls werden Studien über das Triggersystems des Teststandes dargestellt. Insbesondere wurden die Präzision und Verlässlichkeit von Referenzzeitsignalen untersucht.

Contents

Introduction

The discovery of the Higgs boson in 2012[1] was one of the most recent milestones in a row of outstanding results in particle physics since the discovery of the substructure of atoms. For all these successes the tools for radiation and particles detection were essential to the field of particle physics, but rarely coming to the fore. Those detectors have evolved from comparatively simple ones like cloud chambers, used by Anderson when he discovered the positron in 1932[2] towards huge and complex machines like the *ATLAS* detector at high energy particle accelerators nowadays.

The development of the detectors is not only given by major changes in technology but also by continuous improvements of existing ones. After starting the *Large Hadron Collider* operation, a first data taking period was carried out with a center of mass energy of 7 TeV and a peak luminosity of about $2 \cdot 10^{-32} \frac{1}{\mathrm{cm}^2\mathrm{s}}$ in 2010. During the last years the collider performance increased in a couple of steps and further development including several upgrades over the next decades is planned. The detectors on the other hand have to share this process to make physics research possible. While a continuously increasing understanding of the detectors is valuable, there also have to be hardware improvements at a certain point to be able to handle the development of the collider.

This thesis consists of two parts, both contributing to the further development of particle detector systems. Detailed background simulation studies on the shielding of the planned *New Small Wheel* as part of the *ATLAS* muon spectrometer upgrade are shown in the first part. The second part describes the design and the construction of a local test facility for gaseous detectors, enabling future detector research at the University of Würzburg.

[1] More detailed information on the discovery can be found in [1] and [2], for instance.

[2] Anderson published a paper on the discovery in the Physical Review Letters in March 1933, while the corresponding events, leading to this paper, were already recorded in August 1932. Besides a detailed description of the subject some pictures of particle traces in cloud chambers can also be found in this article [3].

Simulation Studies on the New Small Wheel Shielding of the ATLAS Experiment

1. The Setting of the ATLAS Experiment

The *ATLAS* Experiment is one of several experiments operating at the Large Hadron Collider at *CERN*. For putting *ATLAS* in context a description of the Large Hadron Collider and *CERN* will be given first.

1.1. CERN

CERN is an acronym for *Conseil Européen pour la Recherche Nucléaire*, that translates to *European Council for Nuclear Research*. The information on *CERN* in this chapter is based on [4]. The *Convention for the Establishment of a European Organization for Nuclear Research* entered into force on September 29th 1954, starting *CERNs* story of success. The goal of *CERN* was defined in article 2 of this convention as followed: "The Organization shall provide for collaboration among European States in nuclear research of a pure scientific and fundamental character, and in research essentially related thereto." [5]

Since then *CERN* has grown from 12 founding states to 21 member states in 2015. In addition there are a lot of non European observers and co-operators. Altogether several thousand scientists from 113 countries share common research goals.

At the *CERN* site near Geneva many different experiments are carried out, but the founding convention already explicitly mentioned a proton synchrotron and a synchro-cyclotron to be built. Today collider physics is still a major part of the scientific program of *CERN*. The main accelerator currently used is the *Large Hadron Collider*.

1.2. Large Hadron Collider

The *Large Hadron Collider* (*LHC*) is a hadron accelerator and collider installed in the tunnel of its direct predecessor. The following chapter is based on [6]. The *LHC* has been built as a two ring superconducting hadron accelerator to provide proton proton collisions, as well as heavy ion collisions. In case of proton proton collisions the design center of mass energy is 14 TeV, while the design luminosity is $10^{34} \frac{1}{\mathrm{cm}^2\mathrm{s}^1}$.

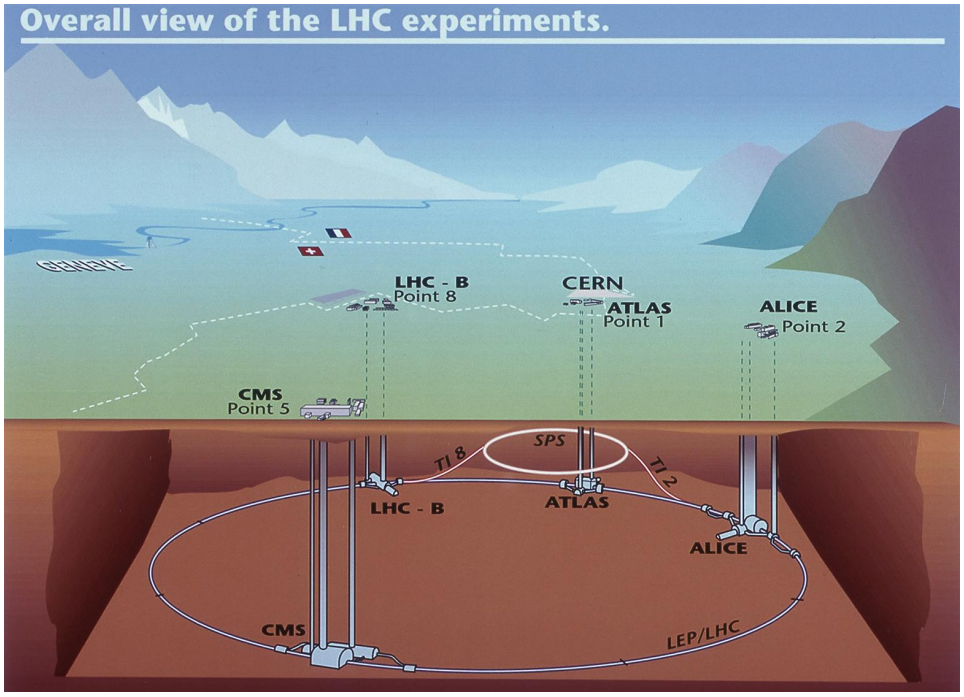

Figure 1.1.: Overview of the main experiments at *LHC* and their position within the accellerator tunnel. The border between France and Switzerland is also shown here, as the ring is crossing it. [7]

The *LHC* ring features four interaction points at which four main experiments are installed, as it can be seen in figure 1.1. *ATLAS* and *CMS* are general purpose detectors, while the other two main experiments are more specialized. On the one hand there is *LHCb* aiming for B-physics studies and on the other hand *ALICE*, which was designed for dedicated ion-ion-collission studies.

Within this work only *ATLAS* will be discussed in more detail (see chapter 2).

2. ATLAS

ATLAS is one of the two multi purpose detector experiments at the *LHC*. The following sections on *ATLAS* and its subsystems are based on [8]. As a multi purpose experiment the *ATLAS* detector is designed to study the full range of physics that can be reached with the high energy and high luminosity provided by the *LHC*. While the search for the Standard Model Higgs Boson was used as one benchmark for the detector performance during its design, there is a wide range of other processes and theoretical predicted particles not less interesting to be probed. High precision tests of flavour physics and QCD, searches for heavy gauge bosons like W' or Z', supersymmetric particles or flavour-changing neutral currents are just a few examples for further study opportunities the detector is designed for.

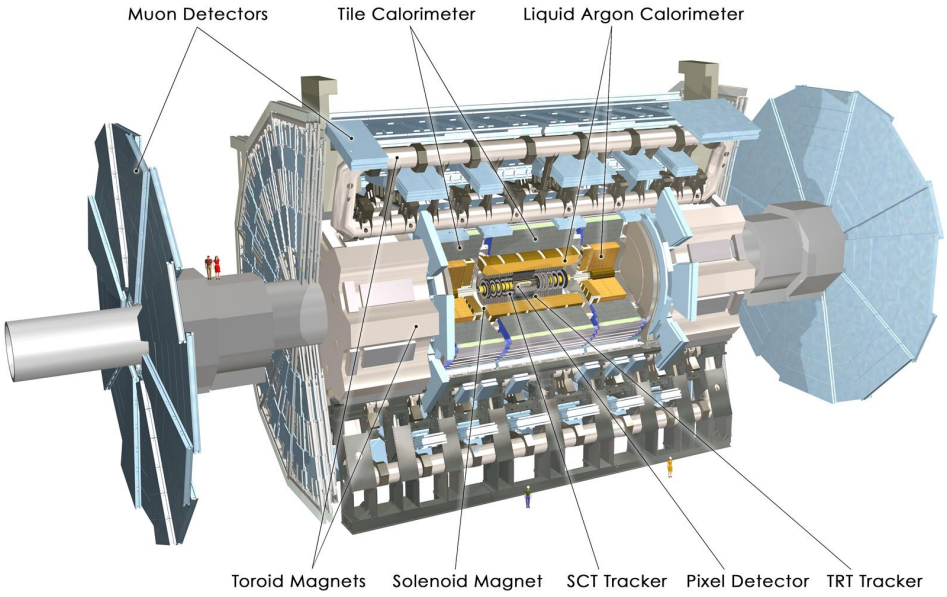

Figure 2.1.: A cut-away view of the *ATLAS* detector showing the sub-detectors [9].

The *ATLAS* detector follows a forward-backward symmetric barrel-endcap design with a superconducting solenoid surrounding the inner-detector and three large

superconducting air-cone toroids around the calorimeters. An overview graphic is shown in figure 2.1. The following sections will give a brief overview of the subsystems of the detector, focusing on the muon spectrometer, which is embedded in the toroidal field.

2.1. The coordinate system of ATLAS

A common right-handed coordinate system with origin in the interaction point in the center of the *ATLAS* detector is usually used by the *ATLAS* collaboration. It is capable to precisely and uniquliy describe positions and directions and will be used throughout this work, too.

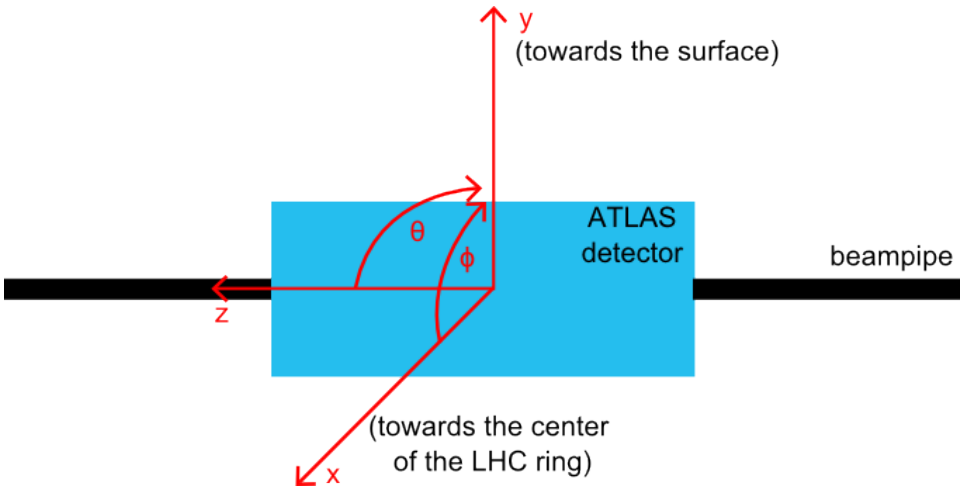

Figure 2.2.: Schematic drawing of the *ATLAS* coordinate system.

The beam line defines the z-axis, while the x-y plane is perpendicular to it. The x-axis is defined by the connecting line between the interaction point and the center of the *LHC* ring and the y-axis points upwards toward the surface (see fig. 2.2). The polar angle θ is measured from the beam axis towards the x-y-plane, while the azimuthal angle ϕ is defined around the beam axis. Instead of using θ it is common to specify the pseudorapitity $\eta = -\ln \tan \frac{\theta}{2}$.

2.2. Inner Detector

The central solenoid of *ATLAS* is able to generate a 2 T magnetic field in a cylindrical region, which measures about 5.3 m and has a diameter of 2.5 m. Therefore it includes almost the whole volume of the Inner Detector. The region $|\eta| < 2.5$ is covered by pixel detectors and silicon microstrip trackers. The pixel detectors are located closest to the interaction point, having the highest detector granularity (see figure 2.3). Furthermore there is a transition radiation tracker counting as part of the inner detector. It is built out of straw tubes and polypropylene as transition radiation material.

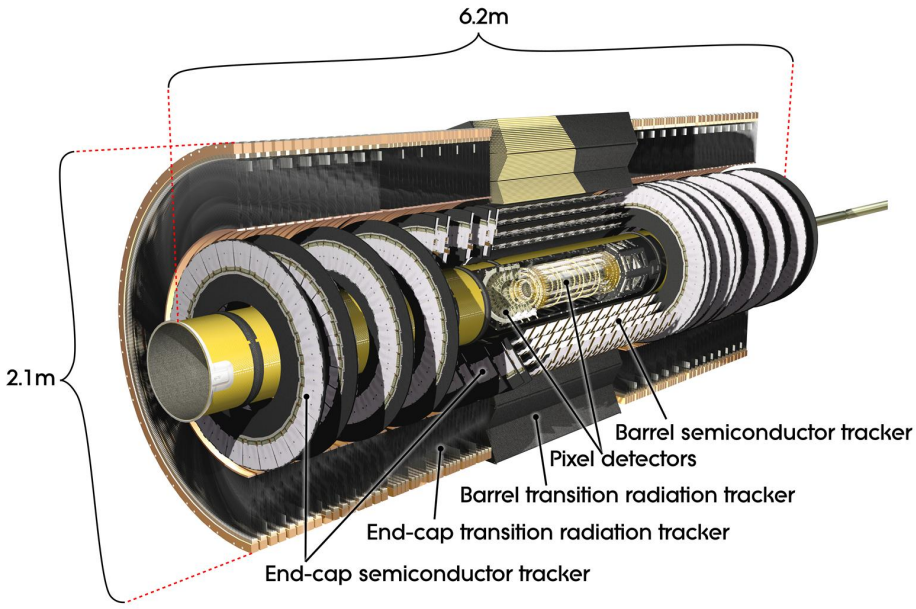

Figure 2.3.: Cut-away view of the inner detector of *ATLAS* [10].

The transition radiation tracker gives only coverage up to $|\eta| = 2.0$. Nevertheless, it contributes significantly to the measurement of momenta of charged particles in this region, since the distance traversed by a particle in the transition radiation tracker is about double the distance in the pixel detector. By this it compensates for the worse spacial resolution with respect to the pixel detectors. It also improves the electron identification, thanks to the information of the transition-radiation.

2.3. Calorimetry

The calorimetry of *ATLAS* uses an electromagnetic calorimeter, a hadronic calorimeter and an additional forward calorimeter. Both, the electromagnetic calorimeter as well as the hadronic calorimeter, are seperated in barrel and endcap components. The calorimetrers are particularly designed to match the physics requirements, which are providing a precise measurement of electron and photon energies, to enable a sufficient jet reconstruction and contribute significantly to the determination of the transverse missing energy. Furthermore it was considered to contain enough material to minimize the amount of punch-throughs of the electromagnetic and hadronic showers into the muon system.

In the electromagnetic calorimeter lead is used as absorber material, while for the active material liquid argon is chosen. This setup requires a high electric field for detecting showers and measuring their energy. The electromagnetic calorimeter covers the region up to $|\eta| = 3.2$ and is designed to be perfectly symmetric in ϕ, while avoiding azimuthal cracks. The radiation length is a reasonable measure for the amount of material in the electromagnetic calorimeter. It is defined as the distance in material over which the energy of an electron is reduced by the factor $\frac{1}{e}$ by loosing the energy by radiation exclusively [11]. In the barrel region the electromagnetic calorimeter has a thickness corresponding to at least 22 radiation lengths, while the endcaps correspond to at least 24 radiation lengths.

The hadronic calorimeter has different designs in the barrel and in the endcaps, together covering a comparable range like the electromagnetic calorimeter up to $|\eta| = 3.2$. The endcaps are using liquid argon as active material, but instead of lead used as absorber material here it is copper. The hadronic calorimeter in the barrel region is using scintillating tiles as active material alternating with steel plates as absorber material. For describing the amount of material in the hadronic calorimeter the interaction length is more reasonable than the radiation length, due to the different processes dominating in the calorimeters. The interaction length is defined as the distance needed to reduce hadrons by the factor $\frac{1}{e}$ by inelastic processes in matter [12]. In total the hadronic calorimeter has a depth of approximately 10 interaction lengths.

The forward calorimeter is surrounding the beamline inside the hadronic calorimeter endcaps and extends the coverage of the calorimeters up to $|\eta| = 4.9$. It provides electromagnetic measurements as well as such regarding hadronic interactions. For achieving this, the forward calorimeter is composed of three modules, rowed up in z-direction. All three modules are using liquid argon as active material, while they differ in the absorber material used. The first module, optimized to measure

electromagnetic interactions, uses copper as absorber. The other two following modules use tungsten as absorber and are optimized to give information on hadronic interactions.

2.4. Muon Spectrometer

The muon spectrometer is a system composed of trigger chambers, precision tracking chambers and magnets, which allow to measure muons and to determine their momentum based on the bending of their tracks due to the magnetic field. The spectrometer consists of three chamber layers in the barrel and in each of the endcaps. Those layers are commonly called barrel inner (BI), barrel middle (BM) and barrel outer (BO), and endcap inner (EI), endcap middle (EM) and endcap outer (EO), respectively. An overview of the *ATLAS* Muon Spectrometer is shown in figure 2.4. This displays nicely, the endcap design with three separate wheels. The EI is next to the endcaptoroid on the side closer to the interaction point and noticeable smaller then the EM and the EO. For this reason the EI is also called the *Small Wheel*.

2.4.1. Magnetic field

The magnets used in the muon spectrometer are three superconducting air-core toroids. One is a barrel toroid and the other two are endcap toroids (see also figure 2.4). All three toroids consist of eight coils positioned symmetrically around the beam axis. The endcap toroid coil systems are rotated by 22.5° with respect to the barrel toroid coils, which makes them fit in the radial spaces of the barrel toroid at each of its ends. One way to characterize the power of the magnetic field to bend the muon trajectory along the direction of propagation is the bending power. It is defined by the field integral $\int B\mathrm{d}l$, where the magnetic field component B is normal to an infinite-momentum muon trajectory from the innermost to the outermost muon chamber. In the *ATLAS* muon spectrometer the bending power varies between approximately 1 Tm and 7.5 Tm. For monitoring the magnetic field some 1800 Hall sensors are positioned in the muon spectrometer volume.

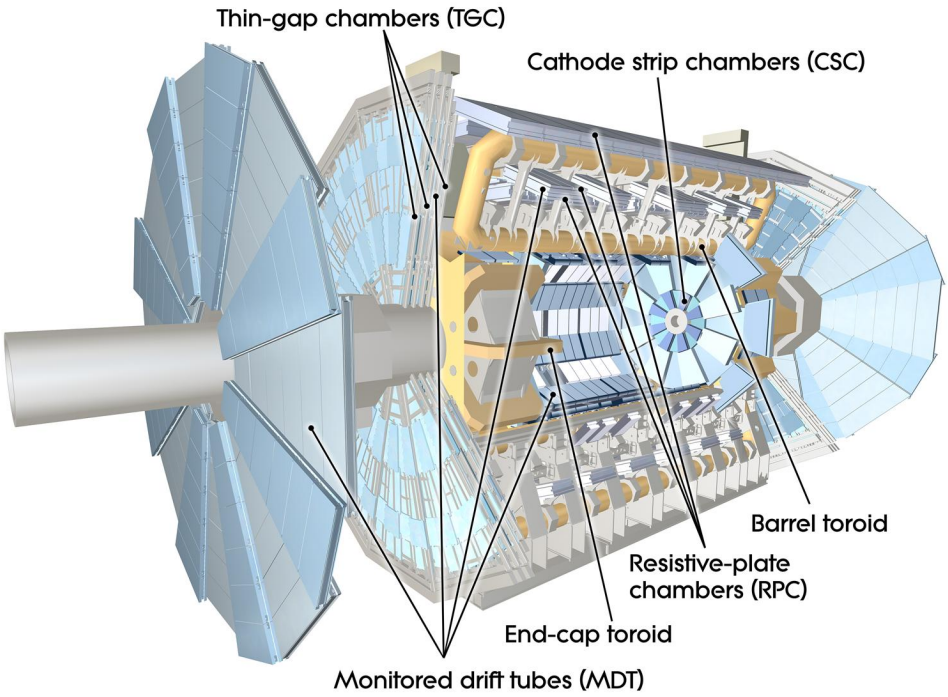

Figure 2.4.: Cut-away view of the muon spectrometer of *ATLAS* [13]. The magnets are indicated in yellow. Neither the inner detector, nor the calorimeters are shown.

2.4.2. Muon detectors

Several detector designs are realized in the *ATLAS* muon spectrometer meeting two purposes: On the one hand there are chambers constructed especially for triggering, on the other hand there are chambers for precision-tracking. The information on these chambers are based on [14] in addition to [8]. For the precision-tracking mainly *Monitored Drift Tubes* (*MDT*) are used, complemented by *Cathode Strip Chambers* (*CSC*) in the EI (see also chapter 3.1). Two different types of trigger chambers are installed: In the barrel *Resistive Plate Chambers* (*RPC*) are mounted, while in the endcaps *Thin Gap Chambers* (*TGC*) are utilized.

The schematic layout of the muon spectrometer is shown in figure 2.5. The *MDTs* are arranged in three barrel station layers and three endcap station layers, almost symmetrically distributed. By this the (*MDTs*) cover a pseudorapidity range $|\eta| < 2.7$, except in the EI where the range is limited to $|\eta| < 2.0$, while for $2.0 < |\eta| < 2.7$ (*CSCs*) are used. Also the three *TGC* station layers in the endcaps and the three *RPC* station layers in the barrel guarantee a complete coverage. However the

trigger chambers are situated differently than the *MDTs*. In the barrel two of the trigger chamber layers are in the BM while one is in the BO. In the endcaps all three chamber layers are in the EM. An additional layer of *TGCs* in the EI was initially used for other than trigger purposes (see also chapter 2.5). Finally there are some additional *MDT* chambers placed at various locations in the *ATLAS* detector for increasing the coverage.

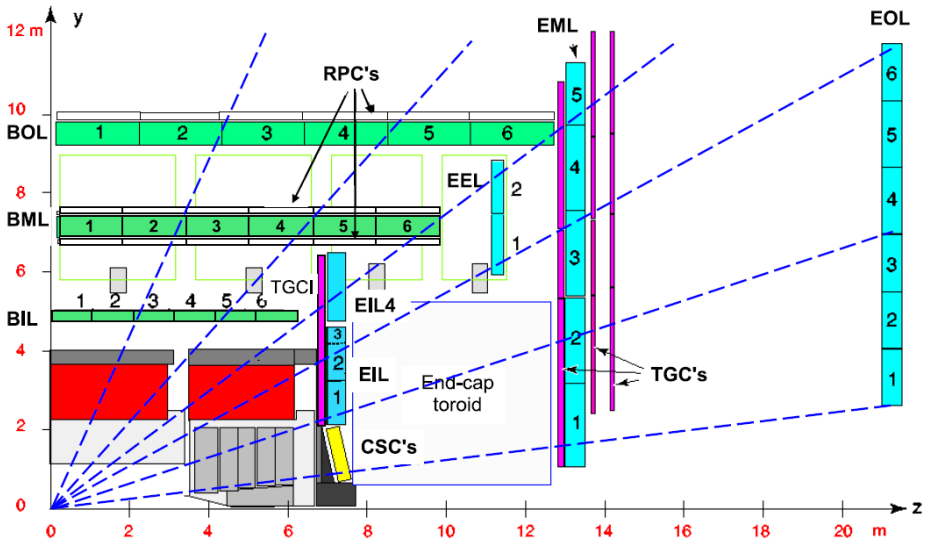

Figure 2.5.: Cut-away view of the *ATLAS* detector [8]. *MDTs* are shown in green in the barrel region and blue in the endcap region. *TGCs* are shown in purple and *RPCs* are shown in white. The *CSCs* in the inner endcap are indicated seperately in yellow. Also the three barrel station layers, as well as the three endcap layers can be seen in this view.

The *MDT* chambers are composed of individual drift tubes with an outer diameter of 29.97 mm, operated with an Argon-CO_2 gas mixture of the ratio 93 to 7. The absolute gas pressure amounts 3 bar and an anode potential of 3080 V is applied. To achieve highest spacial resolution not only the precision of the single tubes is important but also the knowledge about possible deformations and the positions of the chambers with respect to each other. This information is provided by monitoring their internal geometry and relative positions with an optical alignment system. Enviromental parameters like thermal conditions are monitored as well. The importance of the monitoring is stressed, as it is even part of the name.

The *CSCs* are multiwire proportional chambers, where both cathodes are segmented into approximately 1.5 mm strips perpendicular to each other and both are read out. This way a good resolution in ϕ and η is achieved. The *CSCs* are operated with

a voltage of 1900 V and with a ratio of 80 to 20 of Argon and CO_2 at approximately atmospheric pressure. The distance between the anode wires and the cathode strips is the same as from wire to wire, namely 2.5 mm. The advantage of the *CSC* over the *MDT* is the higher maximum counting rate. The maximum electron drift time in an *MDT* is about 700 ns, while the maximum electron drift time in *CSCs* is less then 40 ns. This leads to a maximum counting rate of the *CSC* of 1000 $\frac{\text{Hz}}{\text{cm}^2}$, compared to 150 $\frac{\text{Hz}}{\text{cm}^2}$ in case of the *MDT*. The charge induced by the avalanche in the gas and collected by the cathode strips is distributed over several of them. The peak of this distribution indicates the spatial information. Inclined tracks and resulting spread of the anode charge lead to a worse resolution. To avoid this effect the *CSCs* themselves are tilted toward the interaction point, in a way that an infinite momentum track crosses the chambers perpendicularly.

The trigger chambers provide fast information mainly used for the trigger system (see also chapter 2.5). Only an approximate estimate of the traverse momentum of a crossing muon is needed for the trigger. In addition the trigger chambers are used for bunch-crossing identification and for fast tracking measurements for high-level trigger stages. Eventually those chambers are important to complement the information of the *MDTs*. The main purpose of the *MDTs* is to determine the coordinate of a track in the bending plane. Therefore the coordinate in the non-bending plane is measured more precisely by the trigger chambers. Both coordinate information are matched and combined afterwards for getting best results. In the barrel *RPCs* are used. They are built out of two parallel resistive plastic plates with a distance of 2 mm. On the outside of those plates a graphite coating is utilized as electrodes, creating an electric field of 4.9 $\frac{\text{kV}}{\text{mm}}$ inside the gap. The readout is done with capacitively coupled readout strips. The gas mixture used for *RPC* is $C_2H_2F_4$, Iso-C_4H_{10} and SF_6, in a ratio of 94.7 to 5.0 to 0.3.

The *TGCs* are the trigger chambers installed in the endcaps of the muon spectrometer. *TGCs* are multiwire proportional chambers designed similarly to the *CSCs* mentioned above, however, there are also some important differences. The *TGCs* are built out of two graphite cathodes and anode wires in between. The pitch between the wires is 1.8 mm while the distance from the wires to the cathodes on both sides is 1.4 mm. Electrically isolated from the cathode planes there are readout strips oriented orthogonal to the wires on the one side of the gap and a continuous copper layer on the other side. Besides the strips, the wires are used for readout, too. While the cathodes are grounded, the wires are set to 2.9 kV. The gas-mixture is composed of 55 parts CO_2 and 45 parts n-pentane. As this is a highly quenching gas, the gas gain is relatively low. However, it brings the advantage of preventing the occurrence of streamers in all operating conditions. This gas-mixture is flammable, due to the high amount of n-pentan.

2.5. Trigger system

The data acquisition system recieves and buffers the event data from the detector with more than 1600 readout links. Not all data can be written to hard disks and therefore a trigger system is implemented for reducing the amount by deciding on their relevance for physics analyses. The *ATLAS* trigger system has three levels, called L1, L2 and event filter. While the L1 trigger has to reduce the rate to 75 kHz, the design maximum the readout can handle, the higher levels aim for a reduction to 3.5 kHz and eventually a final rate of 200 Hz.

The hardware based L1 trigger achieves the rate reduction by searching for high transverse momentum muons, electrons, photons, jets or large transverse energy, either reconstructed or missing. A subset of all detector information, the trigger chambers of the muon spectrometer and reduced-granularity information from all the calorimeters, are used for the L1 trigger decisions. In contrast the higher trigger levels are software based and use all available detector information.

2.5.1. Muon trigger

One part of the L1 trigger is a muon trigger pocessing information of the trigger chambers in the muon spectrometer (see also chapter 2.4.2). The basic idea of the trigger algorithm is to look for coincidental hits in those chambers. These hits are required to be found in a road, which tracks the path of a muon through the detector starting at the interaction point. The widths of the roads are related to the transverse momentum threshold for the trigger.

In both, barrel and endcap region, the trigger is physically based on the information of three stations (see figure 2.6). The trigger stations in the barrel cover a region up to $|\eta| = 1.05$ and the trigger stations in the endcap span the region from $|\eta|$=1.05 up to $|\eta| = 2.4$. Besides, there are additional chambers in the endcap. On the one hand the innermost station of the EM extends up to $|\eta| = 2.7$ as a single layer, without increasing the overall trigger acceptance. On the other hand there is a layer of *TGC* chambers at the EI reaching up to $|\eta| = 1.92$. However, it is not used for triggering in run 1.

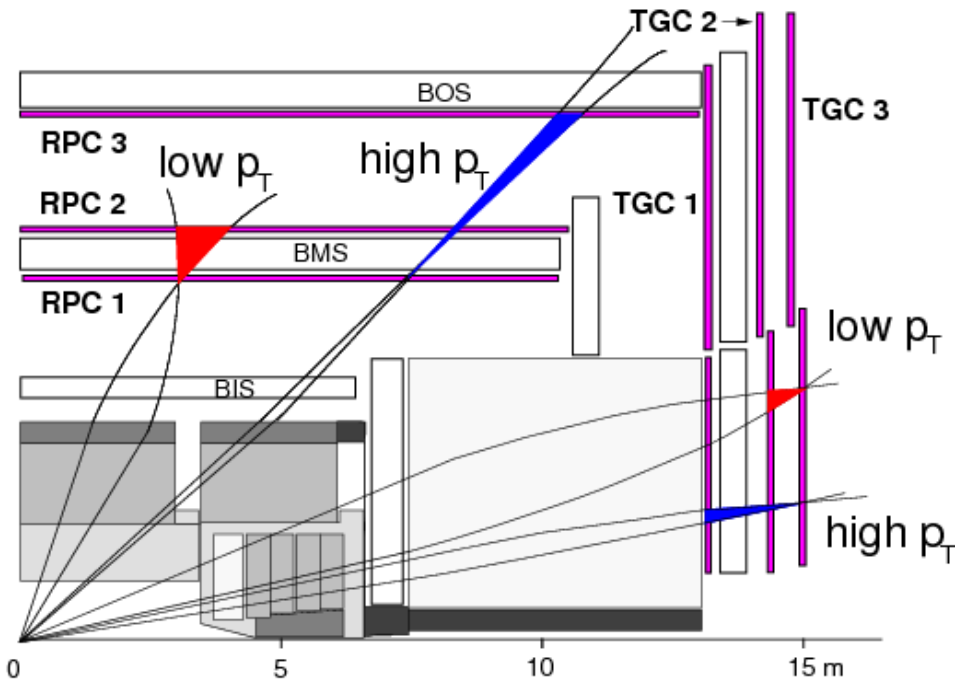

Figure 2.6.: A schematic view of the muon spectrometer [14]. Indicated in purple are the three trigger stations in the barrel as well as in the endcap. Also shown are low and high transverse-momentum roads.

2.6. Background shielding

The high luminosity and center of mass energy of the *LHC* cause challenging experimental conditions. One of those challenges is beam-induced background. In contrast to previous colliders this background is not driven by beam halo particles or beam gas interactions, but by inelastic proton-proton interactions at the collision point. The effect of such background radiation is biggest close to the beam pipe, in the region of the inner detector and the forward calorimeters. It is not only composed of protons or neutrons, though also of secondary radiation resulting from interactions of the primary radiation with detector material. Especially the beam line itself and the detector parts close to it, namely the Inner Detector and the forward calorimeters, are sources of the secondary radiation.

ATLAS contains almost 3000 tonnes of shielding material installed all over the detector, to limit the effects of background radiation on sensitive detector parts. Figure 2.7 gives a fairly complete impression of the variety of shielding components

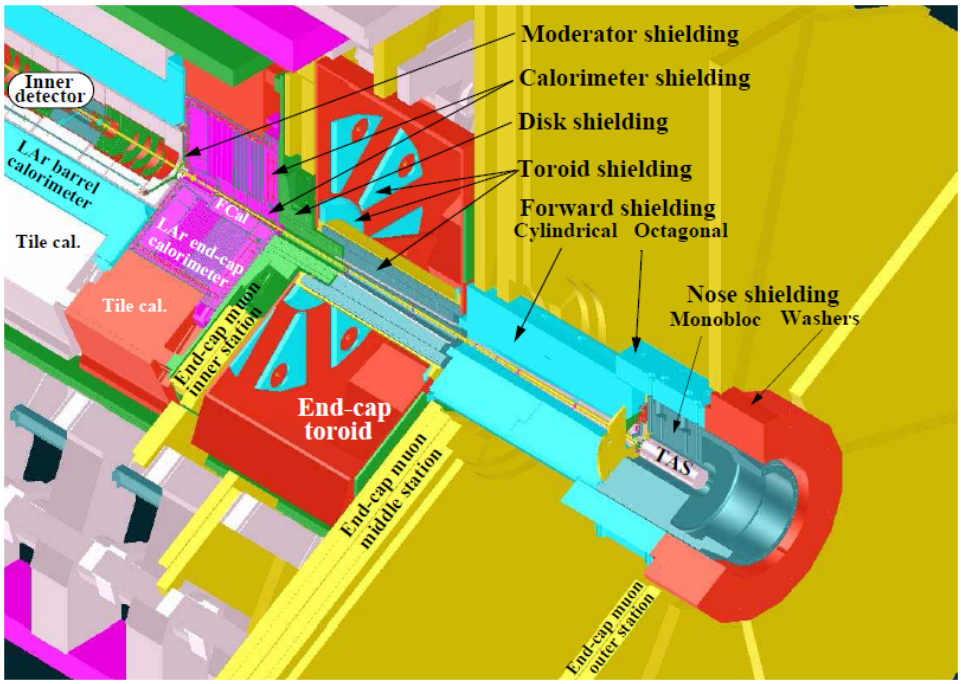

Figure 2.7.: Overview of the variety of different shielding parts inside the *ATLAS* detector [8].

of *ATLAS*. Although there are many different shielding structures, the design strategy is similar for all of them.

Different types of radiation are stopped best by different materials. Furthermore some stopping processes lead to further secondary radiation, which needs to be stopped by a different process subsequently. Detailed information on the interaction processes of different particles in matter can be found in literature, for instance in [12] [11]. Reflecting this, usually a multilayer approach is chosen for shielding in *ATLAS*. The inner layer is usually built from copper, iron or comparable dense materials, which provides a high number of interaction lengths per thickness. The purpose of that layer is to stop high energetic hadrons and their secondaries. The second layer's purpose is to moderate and capture neutrons escaping from the first layer. For moderation of neutrons light nuclei are preferable, as they absorb more neutron recoil energy than bigger one. A suitable choice for the material of this layer is polyethylene doped with boron compounds, often referred to as polyboron. The polyethylene is rich in hydrogen, which makes it highly effective in moderating the neutrons, while the slow neutrons are captured by the boron afterwards. During the neutron stopping process photon radiation is caused. To stop these photons there is a third shielding layer, consisting of material with high atomic numbers, for example lead.

3. The ATLAS New Small Wheel

The *New Small Wheel* is an upgrade project of the *ATLAS* experiment, in particular of the muon spectrometer. The *LHC* will be upgraded in several phases aiming to extent the physics potential by going to higher luminosities and center of mass energies. A timeline of upgrades is presented in figure 3.1, as they were scheduled in fall 2014.

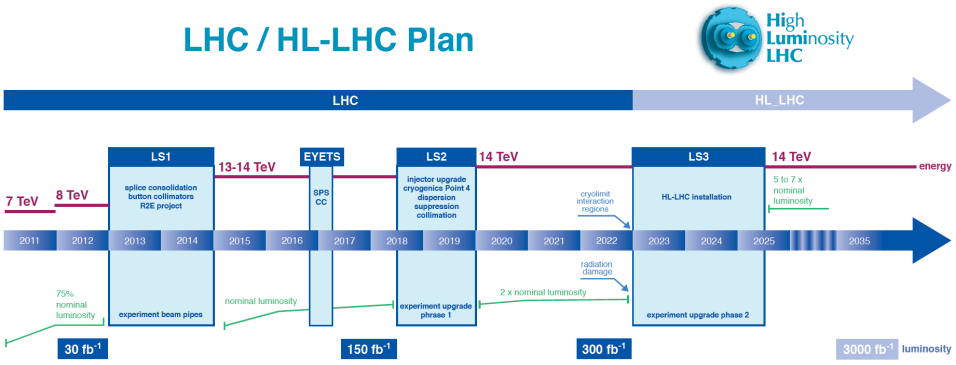

Figure 3.1.: *LHC* upgrade plans [15]. LS is short for Long Shutdown.

3.1. Small Wheel

The *New Small Wheel* upgrade will be an exchange of the currently installed *Small Wheel*. Therefore the *Small Wheel* will be briefly described, first, relying once more on [8].

The *Small Wheel* is the innermost endcap station layer of the muon spectrometer. It is composed of shielding components and three types of chambers. Both can be seen in figure 3.2. The main support structure of the *Small Wheel* is a steel disc with a diameter of 872 cm. At the center of the disc there is a steel tube surrounding the beam pipe. *TGC* trigger chambers are directly mounted on the disc, while the precision tracking chambers are supported by the tube. In the center there are *CSCs*

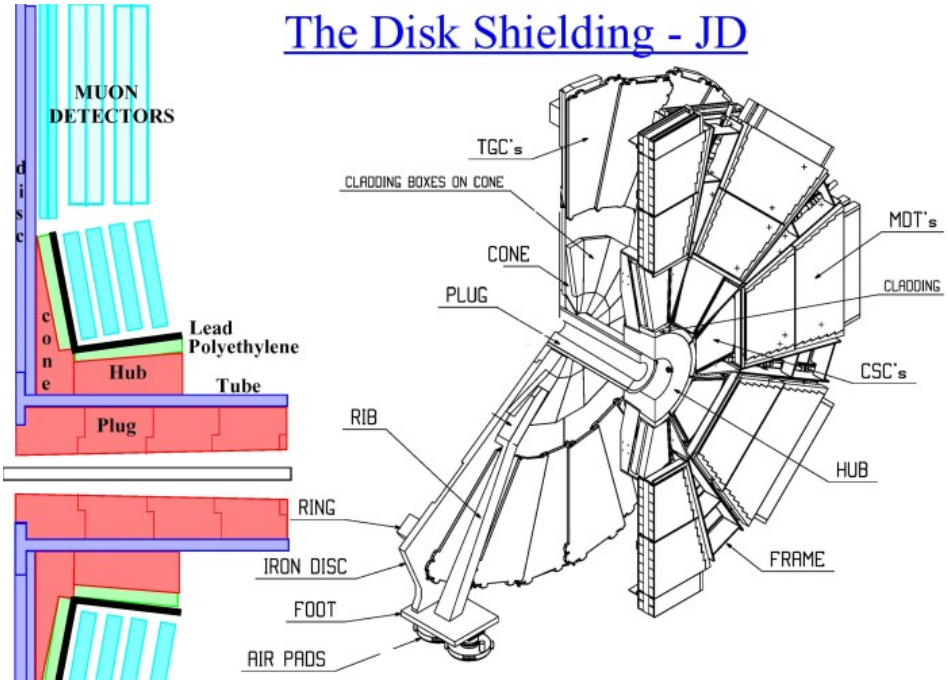

Figure 3.2.: Schema of the *Small Wheel* design [16]. On the right hand side a technical sketch of the *Small Wheel* can be seen. On the left hand side a corresponding cross section shows the shielding with respect to the chambers (indicated in cyan). In figure 2.7 this part of the shielding is labeled as "Disk shielding".

mounted, occupying the radial space between 88.1 cm and 208.1 cm. To increase the performance the *CSCs* are installed tilted towards the interaction-point (see also chapter 2.4.2). *MDTs* follow up the *CSCs* with a higher radial distance to the beam line and complete the *Small Wheel* detectors.

The disc and the tube do not only serve as support structures for the detectors, they are also part of the shielding for the *Small Wheel*. The shielding follows the general multilayer concept, as it is introduced in chapter 2.6. Due to the tilted mounting of the *CSCs* it has a specific geometry (see figure 3.2). Besides the disc and the tube themselves, the shielding parts concentrate in the region of the *CSCs*, as there are the highest rates. The shielding part between the disc and the *CSCs* is commonly called *Cone*, due to its conical shape. The part between the tube and the *CSCs* is called *Hub*.

3.2. Setting of the upgrade

To benefit from the full potential of the improved *LHC* operation the *ATLAS* detector will be upgraded accordingly to the *LHC* itself. During the Phase-I upgrade of *ATLAS* one focus will be on optimizing the L1 trigger, for keeping the trigger rate at a manageable level. In the muon trigger system these efforts focus on the endcap region. There the L1 trigger is based on the EM *TGC* chambers (see chapter 2.5). Low energy background particles, as protons, are generated in the material of the endcap toroid between the *Small Wheel* region and the EM (see chapter 2.6). These particles can produce fake trigger events by hitting the trigger chambers at the same angle like real high momentum muons do. The resulting fake trigger rates can be estimated to be a multiple of the rate of reconstructed muons by looking at figure 3.3. Shown is the distribution of the L1 muon trigger rates for the L1_MU11 setting overlayed with the distributions of the events matched to corresponding muons, which got reconstructed offline. The L1_MU11 trigger setting requires a muon signal formed by a three station coincidence with a transverse momentum threshold of 11 GeV [17] [18]. It is also distinguished between events matched to any reconstructed muon and those matched to muons with a reconstructed transverse momentum higher than 10 GeV. The η-distribution of the muons with transverse momentum higher than 10 GeV is flat, while the trigger is significantly enhanced in the endcap regions above $|\eta| = 1$. To overcome this high fake rates the *TGC* chambers of the *Small Wheel* are integrated in the trigger system as a short term solution.

The tracking chambers' performance also decreases with an increasing background rate and their is no short term solution to overcome it. To solve both problems the present *Small Wheel* will be completely replaced by the so called *New Small Wheel* (*NSW*) in the *Long Shutdown 2* scheduled for 2018. Information on this upgrade described in the following chapter is based on [19].

3.3. Design of the New Small Wheel

The *NSW* will be composed out of 16 detector planes, eight of them utilizing *small-strip TGC* technology (*sTGC*), the remaining eight using *Micromegas* (*MM*). The *sTGCs* are primarily designed for triggering issues, while the *MMs* will be deployed for precision tracking. Nevertheless both detector types are designed to substitute each other up to a certain extent.

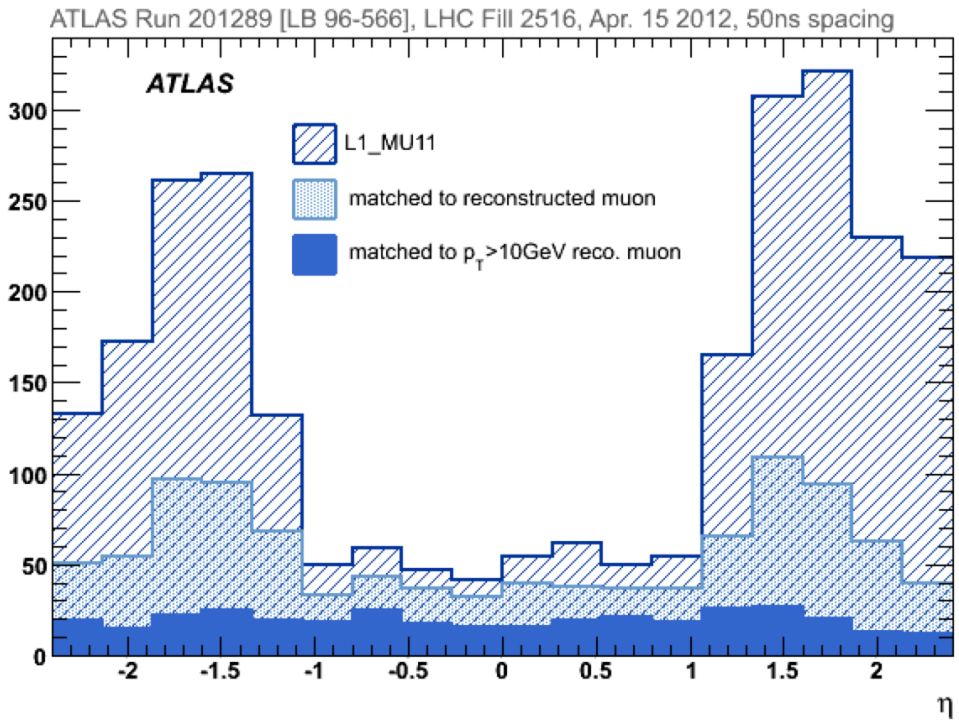

Figure 3.3.: η-distributions of L1 muon trigger rates and the rates of those events matched to corresponding muons, reconstructed offline [19].

The principles of the *sTGC's* design are similar to those of the *TGC* (see chapter 2.4.2). The main difference is the strip pitch. It is 3.2 mm for the *sTGC* and therefore much smaller than the one of a common *TGC* that varies between 14.6 mm and 49.1 mm [14]. The *MM* technology was not used in *ATLAS* before. In general *MM* consist of two thin gas volumes separated by a metallic micromesh. One gas volume serves as a drift region and is located in an electric field between the mesh and an electrode, which are typically several millimeters apart. The second region between the mesh and a readout structure measures only a few hundred micrometers thickness. A strong electric field, however will generate the needed electron avalanches (see figure 3.4). In case of the *MM* foreseen for the *NSW* the readout is provided by capacitively coupled strips with a pitch of approximately 0.4 mm. The distance between the mesh and the readout plane will be 128 µm. A positive high voltage will be applied to the readout strips while the mesh will be laid on ground such that an amplification field of 40 $\frac{\text{kV}}{\text{cm}}$ is created. The drift area will be between the mesh and a drift cathode in 5 mm distance, embedded in a field of 600 $\frac{\text{V}}{\text{cm}}$. The mesh itself will be woven from stainless steel with 325 lines per inch. By this design a special resolution better than 100 µm will be achieved, independent of the particle's incident angle. Additionally a high efficiency even at high background rates will be possible.

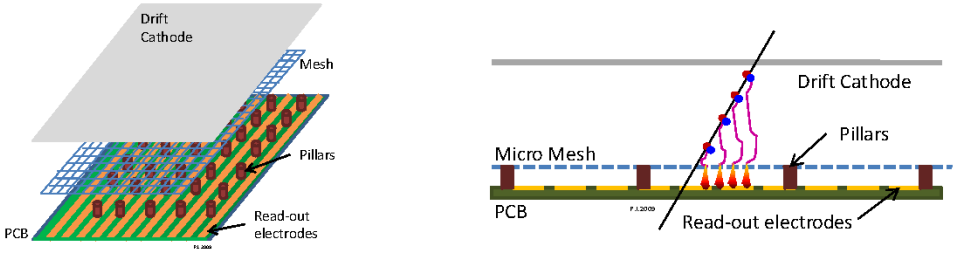

Figure 3.4.: Sketches of the general design and the operating principles of micromegas [19]. On the left hand side a three dimensional sketch is presented, especially showing the different layers of a MM chamber. On the right hand side a cut view can be seen. A particle is indicated, crossing the detector. The red dots along the trajectory indicate primary electrons, while the blue dots are the associated ions. The red lines show the electrons drifting and scattering in the drift region, while the cones between the mesh and the read-out plane represent the electron avalanches.

The whole *NSW* disc will be covered by 8 small and 8 large sectors in ϕ, alternating and overlapping each other. To maximize the lever arm for triggering purposes the outermost 4 detector layers on each side of the overall 16 layers will be *sTGCs*. The 8 inner layers are going to be *MMs*. The trigger acceptance will reach from $|\eta| = 1.3$ up to $|\eta| = 2.5$, while the acceptance for precision tracking will even extent up to $|\eta| = 2.7$. The main geometrical difference to the present *Small Wheel* is the planar structure of the *NSW*, as only two technologies will be used. There will be no inclined chambers as the present *CSCs*. This results in the necessity of adopting the disc shielding (see chapter 2.6). A geometrical adoption of the shielding also provides the opportunity to optimize the shielding dedicated for the new situation. In the subsequent chapters simulation studies will be discussed, addressing such optimizations of the disc shielding of the *NSW*.

4. Tools and parameters for the background simulation

To study the effect of different shielding configurations possible for the *NSW*, a reliable simulation of the background radiation and the resulting rates is necessary. To provide solid results, which are also consistent with other studies, a common application was chosen, that has been used for similar purposes for many years.

4.1. Background simulation application

The studies on the shielding of the *NSW* were done using a well known application for *ATLAS* cavern background simulation [20]. The main background originates from beam remnants of the p-p collision and non-diffractive interactions, whose products enter the detector (see also chapter 2.6). To simulate this processes *Phojet* [21] is used as event generator modeling p-p collisions with a given center-of-mass energy. Subsequently the propagation of the products of these collisions through a dedicated representation of the detector is predicted by *FLUGG* [22]. *FLUGG* is based on *Geant4* [23] to describe the geometries and the materials, while physics modeling is performed by *FLUKA* [24].

Resulting detector signals induced by background are simulated in two steps. The application allows to define logical scoring volumes representing the detector stations of interest. As soon as a tracked particle is entering such a volume it is selected and all relevant particle information is recorded. In a second step the detector hit rate is calculated out of the particle fluxes penetrating a given scoring volume, the path length inside, and the energy-dependent and technology-specific sensitivity of the detector. To enhance the statistics the detector sensitivities for neutrons and photons has been increased by a factor of ten. In the normalization of the rates it is therefore mandatory to correct for this artificial configuration.

Besides the hit rates in selected volumes the cavern background application provides as well the properties of the particles, which cause a hit in a sensitive volume during their passage through the detector. Amongst other features it is possible to store the birth position of particles, too. Due to the fact that only the information of the particles hitting a scoring volume is recorded, the birth positions give specific hints where the shielding can be improved.

4.2. Common parameters throughout the studies

The inputs to the cavern background application are information on the position of the detectors, as well as the detector sensitivity to calculate resulting signal rates due to the particle interactions. Neither the exact positions of the detectors of the *New Small Wheel*, nor the detector sensitivities of the new technologies have been known at the time when the following shielding studies were performed. Therefore the positions of the current detectors were implemented and the *TGC* technology was chosen to substitute all detectors in the *NSW* region (the definition of the scoring volumes can be found in appendix A). In consequence the rates estimated by the studies may differ systematically from the rates, that will be measured in the real *NSW*. Nevertheless, the validity of the studies is not corrupted, as all of the results are interpreted as relative predictions.

The simulation gives the number of hits in chosen detectors for a given amount of generated p-p collisions. For calculating the corresponding rates afterwards additional assumptions have to be made. The event rate is given as

$$\frac{dN}{dt} = \mathcal{L} \cdot \sigma,$$

where $\mathcal{L}$ is the luminosity and σ is the total cross section for inelastic p-p interactions. Knowing them and the absolute number of generated events, the rates of background induced detector signals can be calculated easily. In the following studies the luminosity is assumed to be

$$\mathcal{L} = 10^{34}\,\mathrm{cm}^{-2}\mathrm{s}^{-1},$$

while the cross-section is set to

$$\sigma = 70\,\mathrm{mb}.$$

Once more it should be stressed, the exact values of these quantities are only of minor importance, as the validity of comparative studies is not affected by absolute numbers.

5. Studies on the disc shielding of the NSW

A crucial component of the shielding concept for the muon spectrometer is the disc shielding in front of the *Small Wheel* detector chambers. An overview is displayed in figure 5.1 as well as previously in figure 3.2 in chapter 2.6.

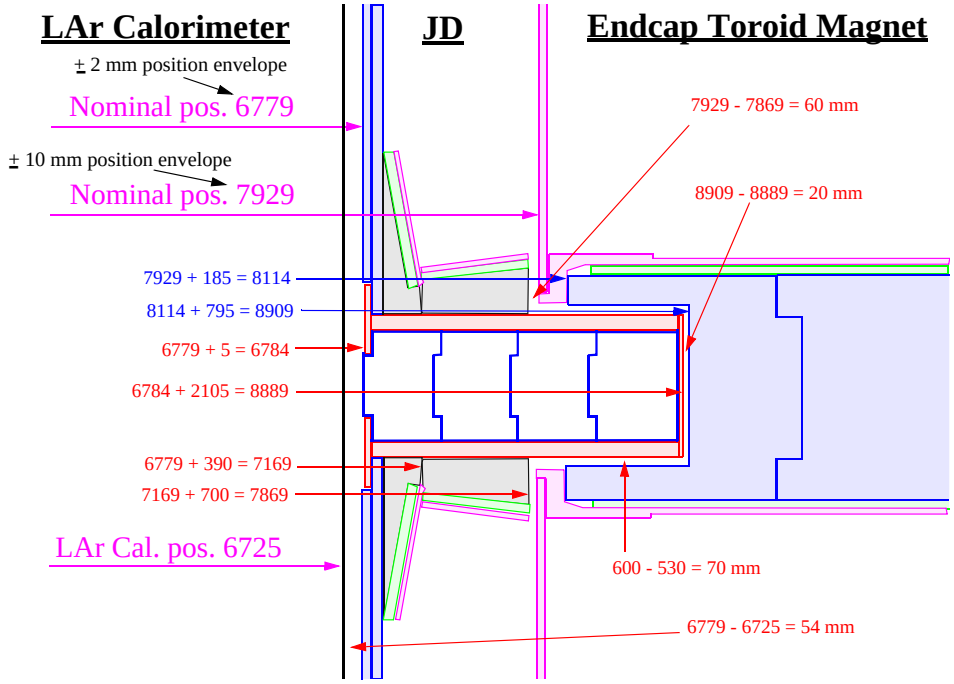

Figure 5.1.: Shielding configuration in front of the *Small Wheel* [16]. The muon chambers are not indicated. They are located in the gap labeled with "JD".Some nominal positions are given as well.

As described in chapter 3.3, the shielding has to be adjusted to the needs of the *NSW* especially regarding the planar geometry of the chambers. At the same time there is the opportunity to optimize the disc shielding, based on various dedicated simulations described in the following.

The studies were done in two phases with different scenarios. The first more general scenario aims for insights regarding the necessary extent of a adapted *NSW* disc shielding in z-direction, respectively the achievable shielding effects for a given extent. Besides, the effects of an extension of the shielding in radial direction were investigated as well. The results of the studies on various such configurations were communicated directly to the *NSW* group, enabling substantiated design discussions. In addition the results were summarized in an *ATLAS* internal note [25].

Int a second step of the studies focused was on specific shielding configurations with a given extent in z-direction of the disc shielding, as the planning and construction of the *NSW* progressed and the final agreement on this distance was reached. An additional investigation was performed on the effects of gaps in the cladding. Those gaps are present in the cladding of the so called *Hub* and needed for supporting structures of the detector chambers. The results of these investigations were once more communicated in the community for optimizing the *NSW* design and summerized in an *ATLAS* internal note [26].

The studies of the two scenarios were performed with different versions of the simulation application, mainly differing in the representation of the *ATLAS* detector, which gets continuously updated. Therefore the absolute numbers obtained by the simulations can be compared directly only within one scenario.

5.1. Simulation studies within a general scenario

The cavern background application version used during the more general first phase of the shielding studies was 00-01-50, which corresponds to the *ATLAS* detector configuration in 2012. The representation of the disc shielding implemented in this version was used as nominal layout during the comparisons. This configuration will be referred to as default in the following. A rectangular geometry was chosen for all the geometries investigated, like shown in figure 5.2.

To adapt the shielding to the *NSW* and the needed rectangular configuration, the *Hub* shielding part, mounted on the tube, as well as the radial shielding directly on the disc, called *Cone*, have to be modified. As the study is focusing on the z-extend, different settings of the *Cone* will be considered, while the *Hub* stays the same throughout all studies. Despite the new geometry, the shielding part next to the disc will still be referred to with as *Cone*. In the currently installed shielding configuration the inclination of the *CSCs*, which follow directly the *Cone*,

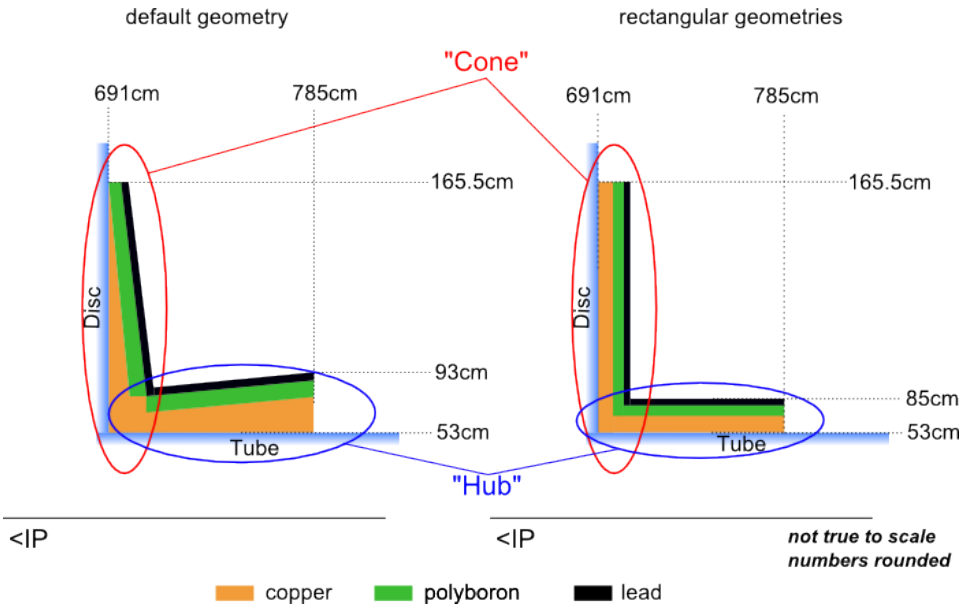

Figure 5.2.: Sketch of studied shielding configurations. On the left hand side the disc shielding as it is represented in version 00-01-50, called default, is displayed. On the right a rectangular configuration showing the general principles of the studied options for a new shielding is presented.

allows to have more material close to the beam line. In a rectangular configuration with a new *Cone* this will no longer be possible. To have the same amount of shielding material in the low-r region, the position of the chambers has to be changed. However this results in a less precise determination of the final muon trajectory, due to smaller possible distances between the detector layers. Therefore a higher background rate is accepted for all configurations instead, as the enhanced performance of the new detectors should be able to compensate the increased background.

The end of the *Hub* closer to the interaction point follows directly after the disc at $z = 691\,\text{cm}$ and extends up to $z = 785\,\text{cm}$. It has the same dimensions along the z-direction as in the default geometry. The radial thickness of the *Hub* is 32 cm and begins right after the tube at a radius of $r = 53\,\text{cm}$ reaching to $r = 85\,\text{cm}$. Essentially these values correspond to the dimension of the default *Hub* at its thin side close to the disc. They are mandatory, as a lager radial extent would prevent the detectors being as close to the beam line as in the actual *Small Wheel*. This would cut into the η acceptance and is therefore strongly disfavored.

The polyboron used in this scenario is assumed to have a density of $0.95\,\frac{\text{g}}{\text{cm}^3}$. The implied composition in terms of mass fraction is 73% carbon, 12.9% hydrogen, 9%

oxygen and 5.1% boron.

5.1.1. Studies on the optimal extent of the disc shielding in z-direction

The goal of this study was to acquire insights on the required extent of the *Cone* in z-direction in order to obtain optimal shielding results. Therefore 8 shielding configurations with different *Cone* geometries but identical *Hub* were implemented supplementary to the default layout. These geometries have different thicknesses for the three shielding layers, giving an impression on their relative importance. The overall thickness of the configurations ranges between 4.5 cm and 18 cm, which is always less than the low-r end of the current *Cone*, which measures 25.5 cm. The different configurations are:

- no *Cone* shielding at all
- 0 cm copper, 3 cm polyboron, 1.5 cm lead - overall 4.5 cm shielding
- 0 cm copper, 3 cm polyboron, 3 cm lead - overall 6 cm shielding
- 0 cm copper, 6 cm polyboron, 1.5 cm lead - overall 7.5 cm shielding
- 0 cm copper, 6 cm polyboron, 3 cm lead - overall 9 cm shielding
- 6 cm copper, 6 cm polyboron, 3 cm lead - overall 15 cm shielding
- 8 cm copper, 6 cm polyboron, 3 cm lead - overall 17 cm shielding
- 6 cm copper, 8 cm polyboron, 4 cm lead - overall 18 cm shielding

For each of these layouts 10000 generated events were examined. For each configuration the hits in the *Small Wheel* chambers and in the inner barrel chambers are recorded. Resulting hit rate distributions as a function of the radius r for the *Small Wheel* and as a function of $|z|$ in the inner barrel region are calculated. Uncertainties are assumed to be Poisson errors and are propagated, assuming all of them are fully uncorrelated. Also the type of the incident particle creating a hit is stored. The extracted fraction for the various particle types is shown for the default configuration in figure 5.3.

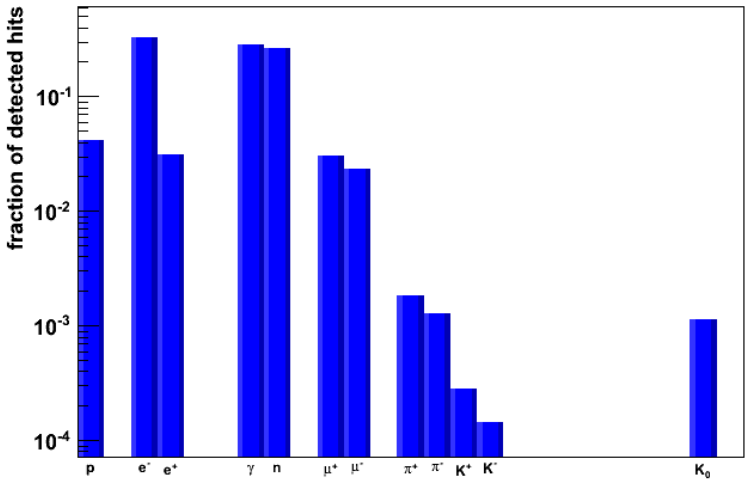

Figure 5.3.: Fraction of different particle types causing detector hits in the default geometry configuration.

The hit rate distributions are not studied for all particle types separately, but it is only distinguished between photons, neutrons and charged particles. The rates are stacked, while the uncertainties only indicate the uncertainty of the respective particle type. The hit rate distribution for the default layout are presented in figure 5.4.

The rates in the BI layer are much lower than in the EI layer. This observation is expected, as the BI is located at a radial distance of about 5 m to the beam line. Comparing the rates in the EI at about the same radial distance, they agree fairly well with the rates in the BI. For the EI layer increased rates are observed in the low r region, while in the BI region two items attract attention. A small peak is present around $|z| = 300\,\text{cm}$, while a second, larger one can be seen around $|z| = 700\,\text{cm}$. This pattern can be recognized for all geometries and is well understood, as it results from the design of *ATLAS*. At around $|z| = 3\,\text{m}$ there is the transition from the barrel to the endcaps of the calorimeters. Especially for the hadronic calorimeter there is a split in between, which leaves a gap for background radiation from the beam line to reachs the BI muon chambers. The *Small Wheel* approaches at $|z| \approx 7\,\text{m}$ the calorimeter but does not fully close the space. This can for example be seen in a birthposition diagramm. Figure 5.5 shows such plots for the default geometry and for a rectangular shielding configuration. The whole *Small Wheel* structure can be conjectured, as all material is a source of secondary radiation. In particular the different geometries of the shielding are well recognizable. Also visible are two gaps starting from the beam line towards higher r. Those gaps indicate

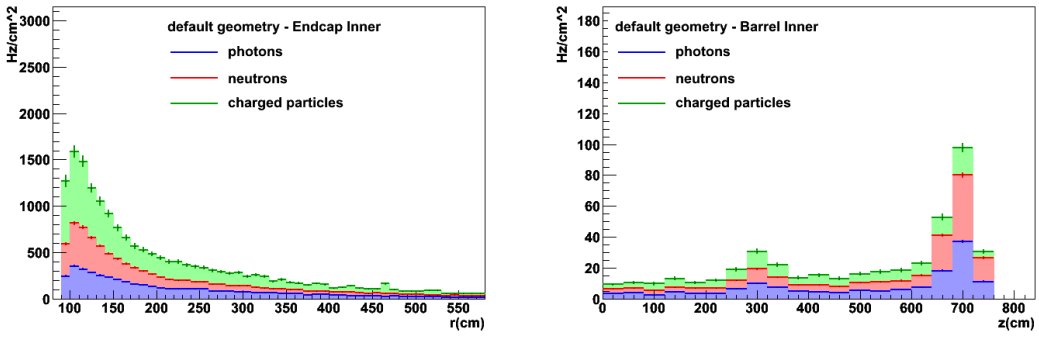

(a) (b)

Figure 5.4.: Simulated hit rates for the default geometry. In (a) the rates as a function of r in the EI are shown, while in (b) the rates as a function of z in the BI are illustrated.

regions without sources of secondary radiation, indicating areas where there is no material. Behind the *Small Wheel*, at about $|z| \approx 780\,\text{cm}$, there is a gap with the number of birthpositions being locally raised right below. This indicates the gap to be a weak aspect of the shielding concept. The second split is at about $|z| \approx 680\,\text{cm}$. It is less distinct than the other, because birthpositions of particles generating hits in the EI are shown and there is the disc shielding between this gap and the EI.

Also the hit rate distributions in the EI region are understood in detail. As a matter of principle there are higher rates closer to the beam pipe and therefore the maximum rate in the EI layer is at low radii, while it decreases with increasing r. Except for the first two bins this behavior can be noticed in figure 5.4 (a). The first bin ($80\,\text{cm} \leq r < 90\,\text{cm}$) is empty and the second bin ($90\,\text{cm} \leq r < 100\,\text{cm}$) has fewer entries than the third one. This can be explained by the fact that detectors are represented by so called scoring volumes (see also chapter 4.1). The scoring volume of the *CSCs*, which are the detectors closest to the beamline, starts at $r = 93.1\,\text{cm}$. In consequence the hit rate has to be 0 in the first bin as there are no detectors that could be hit. The global calculation of the rates results in lower values in the second bin compared to the third one. The rates are normalized per area and in a cylindrical geometry the area is increasing quadratically with the radius. Therefore the normalization is done with respect to the bin width, resulting in lower rates when the scoring volume is not covering the whole bin. As not the complete area represented by the second bin is sensitive, there are of course less hits in the second bin and it has subsequently less statistic than the following one. Thus the third bin is more suitable for comparisons, making a correction of the normalization of the second bin unnecessary.

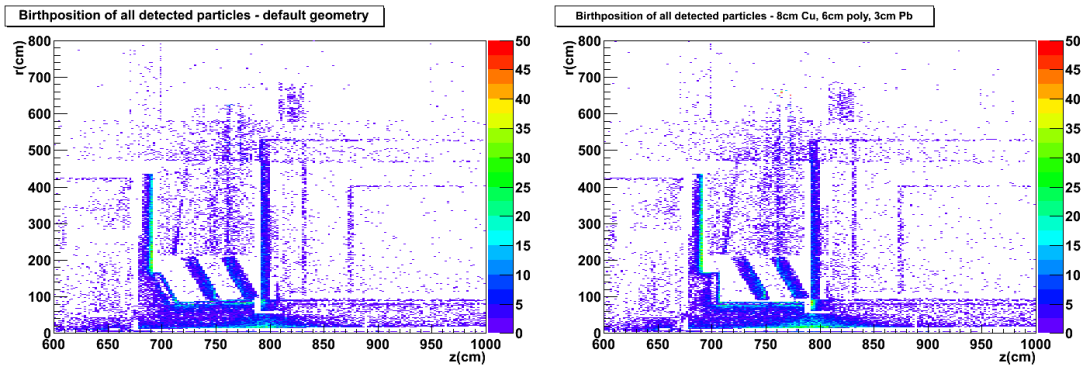

(a) (b)

Figure 5.5.: Birthposition of particles making a hit in the EI. (a) shows the default geometry, while (b) shows a 15 cm thick rectangular shielding. The whole *Small Wheel* design can be seen, as all material is also a source of secondary radiation. Especially the different geometry of the shielding can be easily seen.

The first adapted geometry studied is the extreme scenario with no *Cone* shielding at all, as this is the worst case in terms of background radiation and gives an impression on what to expect from the shielding. The rate distributions for this setup are shown in figure 5.6. The rates in the EI are close to double the rates with respect to the default geometry. In the BI at $|z| \approx 700\,\text{cm}$, where the *New Small Wheel* is positioned, the rates are about 50% higher than in the case of the default geometry. Those results confirm the assumption that a shielding is necessary.

The distributions of the resulting rates obtained for the other geometries (see list on page 27) can be found in the appendix A. The different layouts are compared by calculating the ratio of the rates. The default geometry, which is the layout of the current *Small Wheel*, is the baseline for this study. The ratios of the rates for the investigated geometries relative to the default geometry are calculated for all configurations. As the shape of the rates as functions of r respectively $|z|$ stays nearly identical throughout all the configurations, it seems possible to choose bins representing characteristic items for comparison. To verify this, the ratio of the hit rates of one adapted geometry over the hit rates of the default geometry was calculated as a function of r. The configuration with 3 cm polyboron and 1.5 cm lead was chosen as adapted geometry. The ratio of the hit rates of all particles as well a the ratios only looking at chosen particle types are shown in figure 5.7. Though all the ratios are of the same order a small tendency to smaller ratios for higher radius can be seen. That is not surprising, as the shielding and therefore also the changes to it are limited to radii up to 165.5 cm. It is reasonable to choose low r characteristics for comparison of the rates in the EI, as the decrease of the ratios

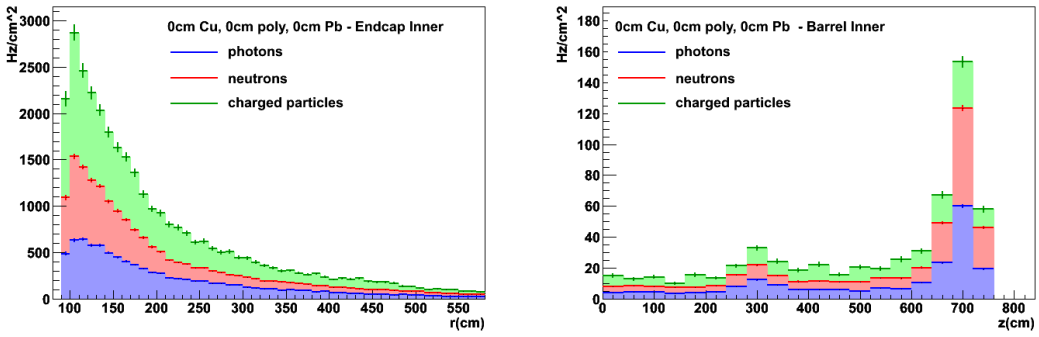

(a) (b)

Figure 5.6.: Hit rates with a geometry without any *Cone*. (a) displays the hit rates in the EI, while (b) shows the hit rates in the BI. The particle types are stacked.

with respect to the radius is small, the most interesting regions of highest rates are at low radii and the statistics get worse with increasing radius. Within this study, only the $|z|$-region at the *Small Wheel* position makes sense for comparisons in the BI, anyway.

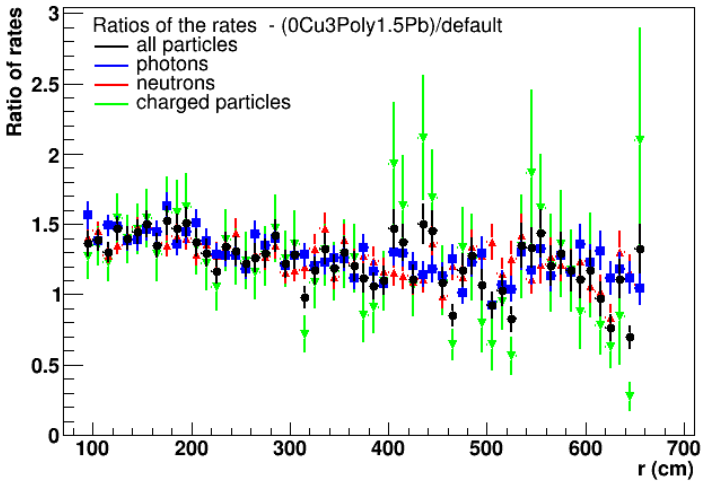

Figure 5.7.: Ratios of hit rates in the EI having a shielding configuration of 3 cm polyboron and 1.5 cm lead over hit rates having the default shielding.

The bin at 100 cm $< r <$ 110 cm in the EI region and the peak at around 7 m in the BI, having the most entries and therefore the highest statistic, are used for making the ratios for comparing the different configurations. Beside the ratios of the rates in these characteristic bins, also the ratio of the accumulated rates of more

extended regions is calculated, in order to avoid the risk of statistical artifacts. For the BI the region above the *Small Wheel* at 640 cm $< |z| <$ 760 cm is chosen. In case of the EI the choice is not driven by geometry or patterns in the distribution. Therefore all bins up to the arbitrarily chosen radial distance of $r = 180$ cm are summed up. The Poisson errors from the hit rates are propagated into the ratios and are shown to give an impression of the reliability.

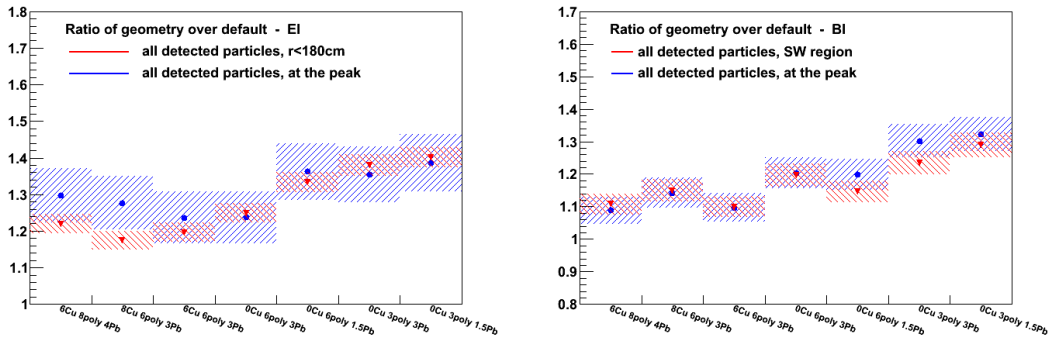

(a) (b)

Figure 5.8.: Ratio of the hit rates of adapted geometries with respect to the default geometry. (a) shows the ratio for the EI, while (b) presents the ratio for the BI. The indicated errors are propagated Poisson errors from the hit rates.

From the ratio plots, displayed in the figures 5.8 and 5.9, a few things can be concluded. Firstly the obvious hypothesis, that more shielding material leads to smaller rates is confirmed. Nevertheless all studied configurations result in higher rates than the default geometry. This is expected as in all tested geometries there is less material than in the default geometry, especially in the *Hub* region. Furthermore a shielding with an vertical extent of at least 15 cm can be designed in a way, that under similar conditions the resulting background rates do not exceed 1.2 times the rates expected for the currently used shielding.

While in general the data allows no definite conclusion which combination of materials and layer thicknesses are most ideal, a statement on the effects of a copper layer can be made. The copper layer seems not to be as important for an effective shielding as the polyboron layer. The reason could be, that the steel disc, that is a shielding layer itself, takes at least partially over the part of the copper layer in the modular shielding concept.

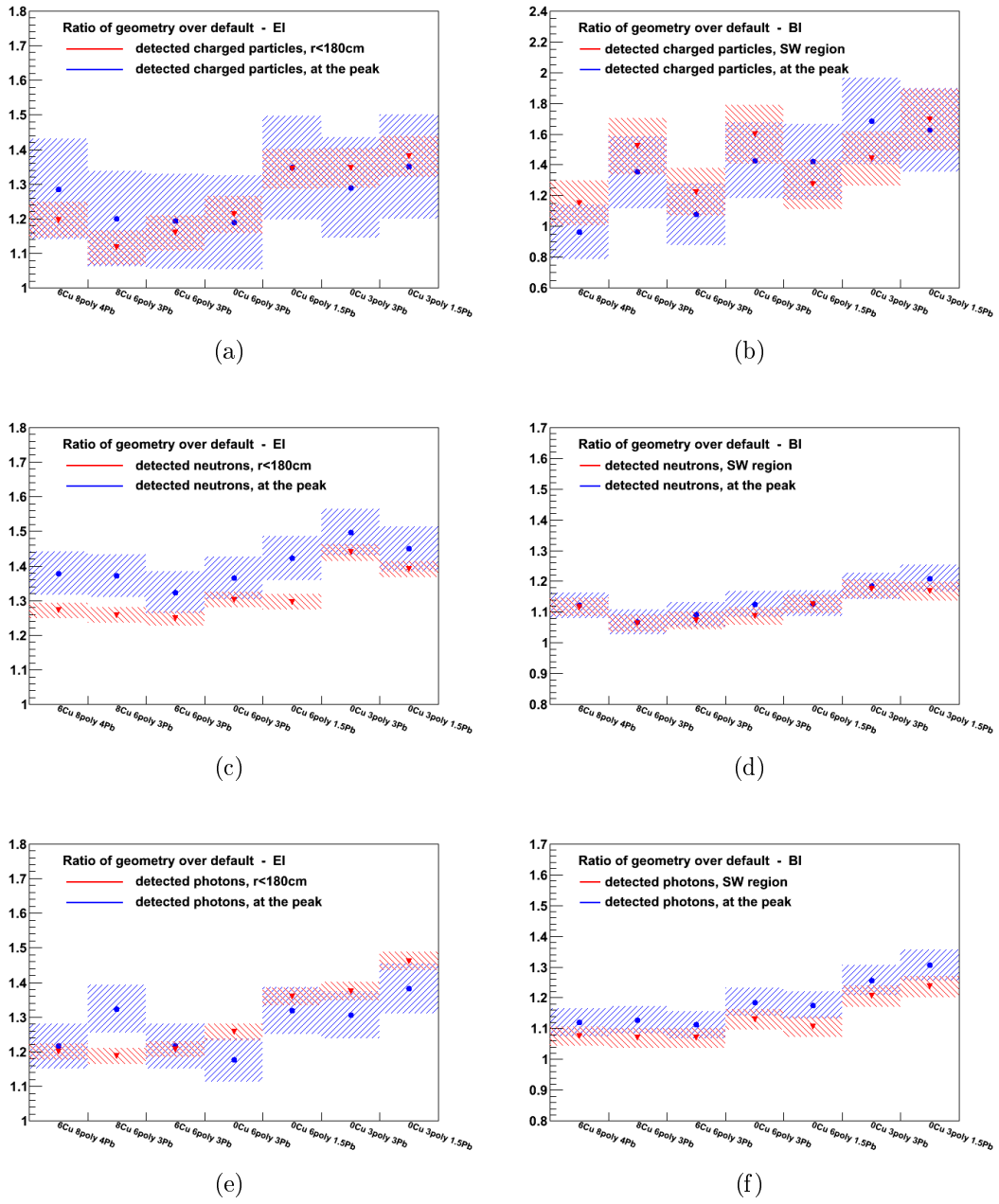

Figure 5.9.: Ratios of the hit rates of the modified geometries divided by the default geometry for different particle types. The left hand side displays the ratios for the EI, while on the right there are the ratios for the BI. (a) and (b) show the ratios for charged particles, (c) and (d) give information on the neutrons and (e) and (f) indicate the ratios of the photons. The uncertainties are propagated Poisson errors originating from the hit rates. The different scale of the y-axis in subfigure (b) compared to all other plots of the BI region should be noted.

5.1.2. Studies on a configuration of an in radial direction extended disc shielding

While the extension of the *Cone* shielding in z-direction is the main focus of studies within the general scenario, investigations were also made to figure out, if modifications of the radial extent or an additional lead cover at the high-radius end of the shielding reduce the rates significantly. Both may be a chance to shrink the shielding along the z-direction.

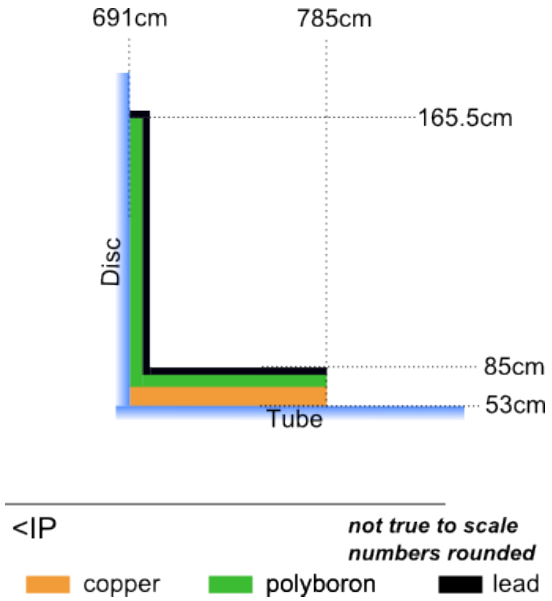

Figure 5.10.: Sketch of the shielding configurations with radial lead cover on top of the high-radius end of the polyboron cladding.

In a first attempt to understand such modifications a quite thin shielding composed of a 3 cm polyboron layer with a 1.5 cm thick lead cover, but without any copper layer was arbitrarily chosen. Based on this shielding configuration, two layouts were studied. On the one hand a setup with an outer radius of $r = 200\,\text{cm}$ of the *Cone* shielding was investigated and on the other hand a configuration was studied for which the outer radius is kept at $r = 165.5\,\text{cm}$ but has in addition a 1.5 cm lead cover in radial direction (see figure 5.10). The distributions of the hit rates can be found in the appendix A. Once more ratios of the hit rates with the modified geometries divided by the hit rates using the default geometry are calculated. In figure 5.11 and figure 5.12 the ratios of the two analyzed shielding configurations are shown. Moreover the ratio of the shielding configuration with a 3 cm polyboron layer and a 1.5 cm thick lead cover, already presented in chapter 5.1.1 is displayed.

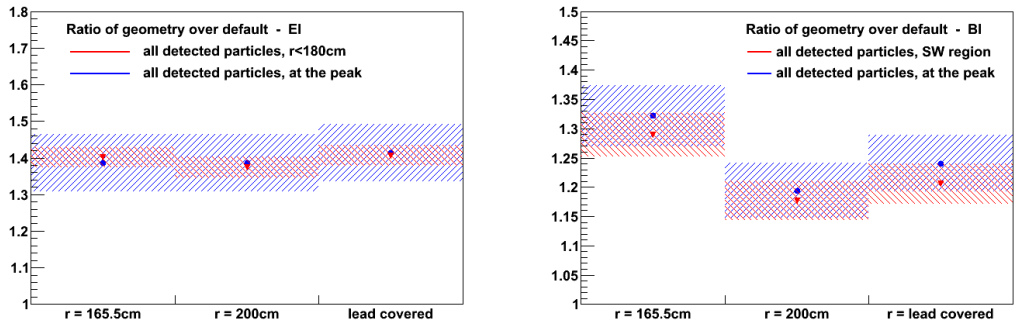

(a) (b)

Figure 5.11.: Ratios of hit rates for geometries with a radial extension divided by the default geometry. (a) shows the ratio for the EI, while (b) shows the ratio for the BI. The indicated uncertainties are propagated Poisson errors originating from the hit rates.

It can be inferred that an extent of the radius of the *Cone* shielding as well as a lead coverage in radial direction have minor effects on the hit rates in the BI region. In the EI region with higher overall rates and therefore enhanced need for effective background shielding, the studied geometries have only negligible effects on the hit rates compared to similar shielding configuration.

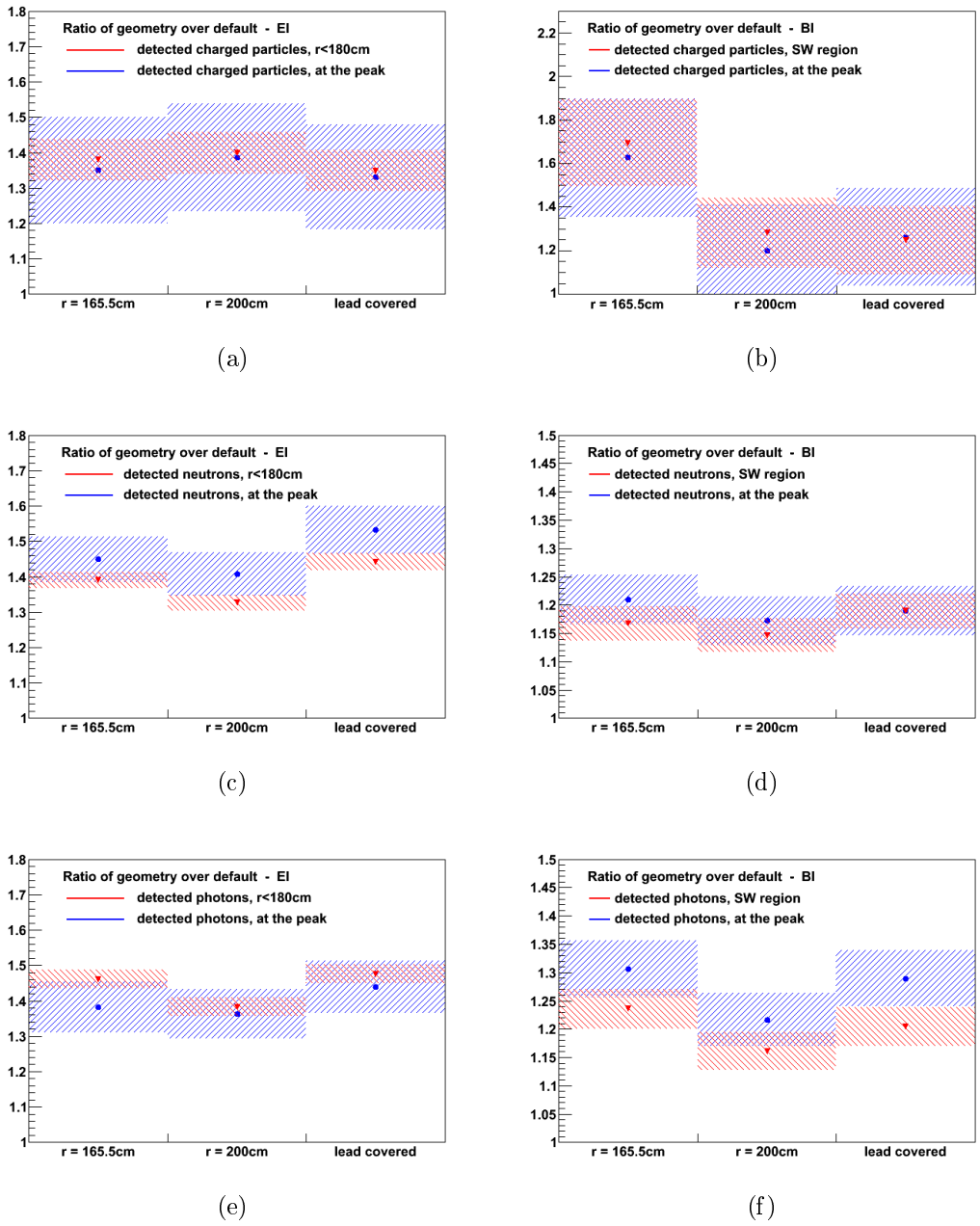

Figure 5.12.: Ratios of hit rates of geometries with a radial extension with respect to the default geometry of different particle types. The left hand side displays the ratios for the EI, while on the right there are the ratios for the BI. (a) and (b) show the ratios for charged particles, (c) and (d) give information on the neutrons and (e) and (f) indicate the ratios of the photons. The uncertainties are propagated Poisson errors originating from the hit rates. The different scale of the y-axis in subfigure (b) compared to all other plots of the BI region should be noted.

5.2. Simulation studies within a restricted scenario

Based also on the results of the studies of the previous more general scenario, the *NSW* design concepts had been reviewed and environmental parameters got defined. The mandatory space for detectors to achieve the aimed spatial resolution was specified, as well as the maximum weight of the complete *NSW* got stricter. Both limited the space in z-direction which can be used for shielding purposes even further.

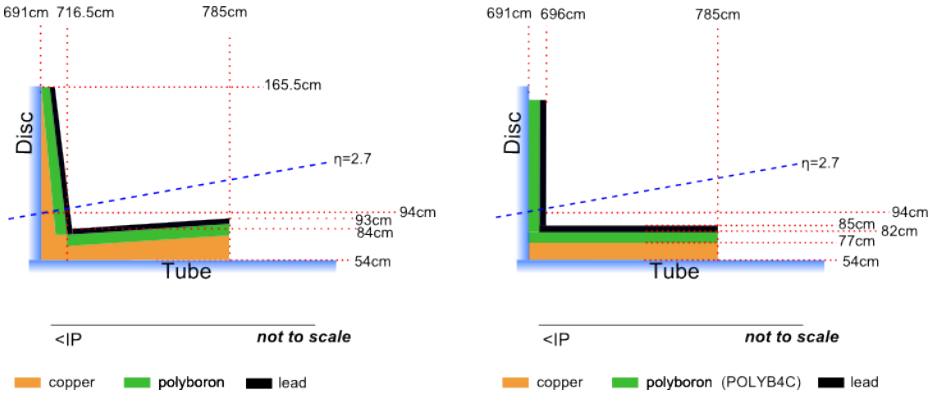

Figure 5.13.: Sketch of the studied shielding configurations. On the leftthe disc shielding is illustrated as it is implemented in software version 00-01-73, considered as default. On the right a rectangular configuration is displayed, which shows the general concept of the studied options for a new shielding.

The extent in z-direction, to be occupied by shielding was restricted to 5 cm, which is much less than the optimal dimension found in the previous simulation studies within the general scenario. Therefore the main goal of the second phase of simulation studies is to determine the optimal shielding composition for a restricted scenario respecting this now given space. A secondary objective during these studies is to investigate the impact of holes in the cladding of the *Hub* and the possibilities to reduce background hit rates by closing such holes.

Besides different goals, the two studies differ also in the used software version of the cavern background application. For the following simulation studies within the restricted scenario version 00-01-73 was used. It differs from version 00-01-50 especially in two aspects relevant for the EI region. Additional shielding parts are added between the endcap calorimeter and the *Small Wheel* disc. Moreover an aluminum beam pipe replacing the stainless steel pipe during LS1 is implemented in this version. Further minor changes in the representation of the detector entered as well. In figure 5.13 the slightly changed dimensions of the default tube with respect to the

general scenario simulations are indicated. Figure 5.2 shows the dimensions of version 00-01-50, which have a different outer radius of the tube.

The material definition of polyboron used for these simulations is also modified. In contrast to the studies within the general scenario it is assumed that the polyboron shielding parts are made out of a commercial polyethylene that is doped with boron carbide (B_4C) and has a density of $0.95\,\frac{g}{cm^3}$. Therefore the mass composition is 81.52% carbon, 13.48% hydrogen and 5% boron.

The presentation of results has slightly changed, too. Due to the fact that in parallel to the studies performed here two related additional investigations[1] got carried out, it was taken care to present the outcomes in a comparable way and to use similar analysis methods. An *ATLAS* internal note on the results of those studies was written, too [26].

5.2.1. Studies on the optimal shielding composition for a z-extent of 5 cm

Within the studies on an optimal *Cone* shielding several parameters had been fixed for all configurations investigated (see figure 5.13). The maximum thickness of the *Cone* along z is 5 cm and it extends up to 165.5 cm in radial distance from the beam line. The *Hub* has the same configuration for all studied geometries. It reaches from the disc up to $|z| = 785.0$ cm with respect to the interaction point and is composed of a 23 cm wide layer of copper, covered with 5 cm polyboron and 3 cm lead. The coverage subsequent to the copper is not complete because of support structures of the detectors (see also chapter 5.2.2).

The studies within the first scenario showed, that copper is less important for an effective shielding composition than polyboron. Therefore configurations out of polyboron with or without lead cover were mainly investigated. To verify and refine the results obtained from the general scenario studies one configuration with a sole copper shielding and another configuration with a copper shielding covered with a lead layer were investigated, too.

The following *Cone* configurations were analyzed by simulating 10000 events each:

[1] Masahiro Morinaga (University of Tokyo) performed studies on a reduction of a thinner disc, with the goal to reduce the overall weight of the *NSW*. Daniel Marley (University of Michigan) investigated the interdependence of the studies on the disc and on the shielding by simulations. It turned out that the effects of modifications in those studies can be combined linearly.

– 4 cm copper, 0 cm polyboron, 0 cm lead

– 4 cm copper, 0 cm polyboron, 1 cm lead

– 0 cm copper, 4 cm polyboron, 0 cm lead

– 0 cm copper, 5 cm polyboron, 0 cm lead

– 0 cm copper, 4.5 cm polyboron, 0.5 cm lead

– 0 cm copper, 4 cm polyboron, 1 cm lead

– 0 cm copper, 3.5 cm polyboron, 1.5 cm lead

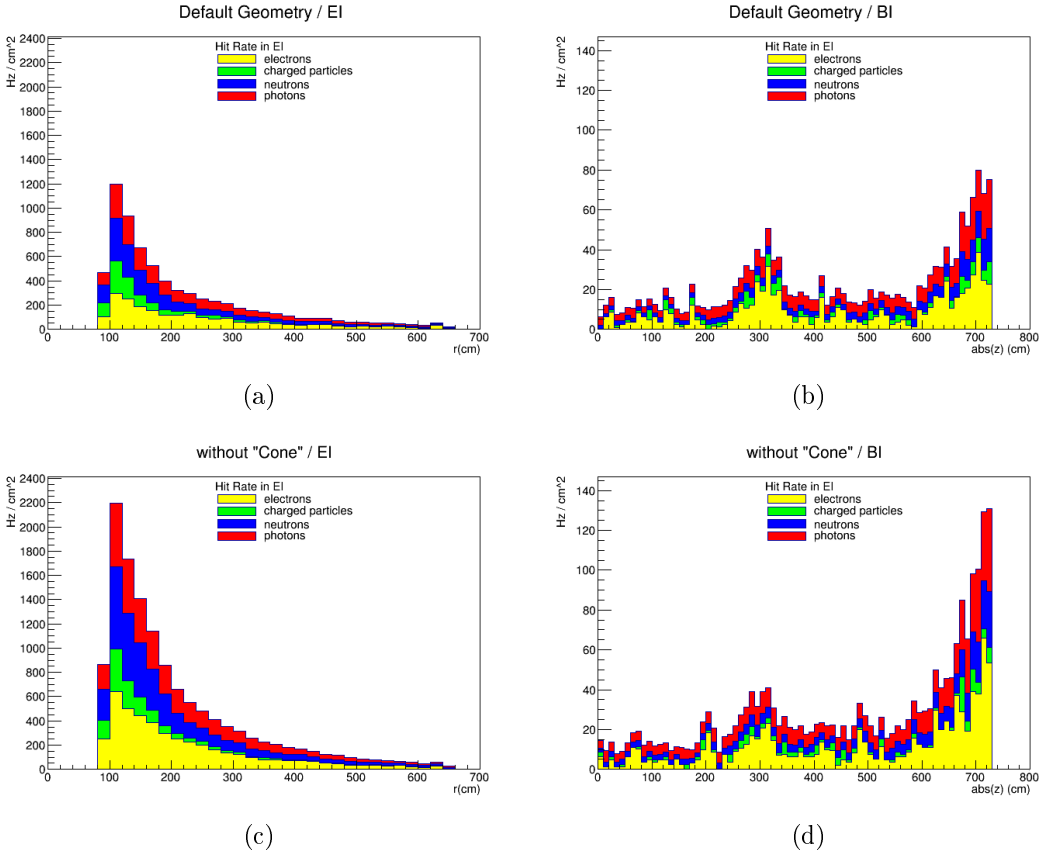

Figure 5.14.: Hit rate distributions of the reference geometries. (a) shows the hit rates in the EI region with the default shielding geometry, while (b) shows the hit rates in the BI region. In (c) and (d) the hit rates in the EI region and the BI region are displayed for no *Cone* shielding at all. Different particle types are distinguished and stacked.

In addition, two reference geometries were simulated. The first reference point is given by the default geometry, representing the current shielding configuration in the *Small Wheel*. It is expected to result in lower rates than all the configurations investigated. The second reference is a configuration without any *Cone* shielding at all, resulting in the worst case scenario. Both are simulated with 40000 events each to have good statistics, as they are the baseline for the comparisons. The hit rates in the EI and BI are displayed in figure 5.14. In contrast to the simulations within the general scenario the electrons are not included in the charged particles but separated as a own type. Also uncertainties on the rates are not indicated. They are comparable to the uncertainties in the previous study, as the same amount of events were generated. The uncertainties for the reference geometries are about half of the uncertainties of the investigated layouts, due to the higher statistics.

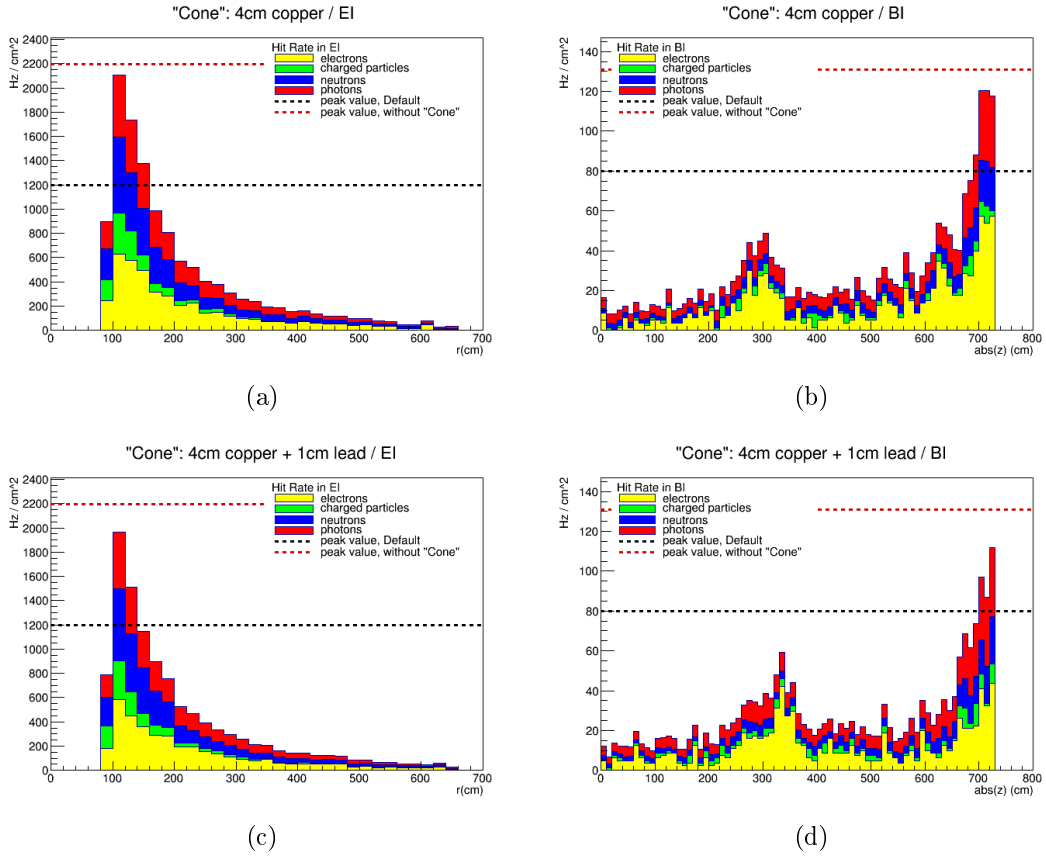

Figure 5.15.: Hit rate distributions for shielding configurations with copper. (a) and (b) display the hit rates for a shielding of 4 cm copper in the EI region and the BI region, respectively. In (c) and (d) the hit rates are presented, which result from a shielding with an additional 1 cm thick lead cover.

Figure 5.15, 5.16, 5.17 and 5.18 present the hit rates in the EI region as well as in the BI region for the simulated geometries. The peak values of the default geometry and the configuration without a *Cone* shielding are indicated in the hit rate plots of the investigated configurations by dotted lines.

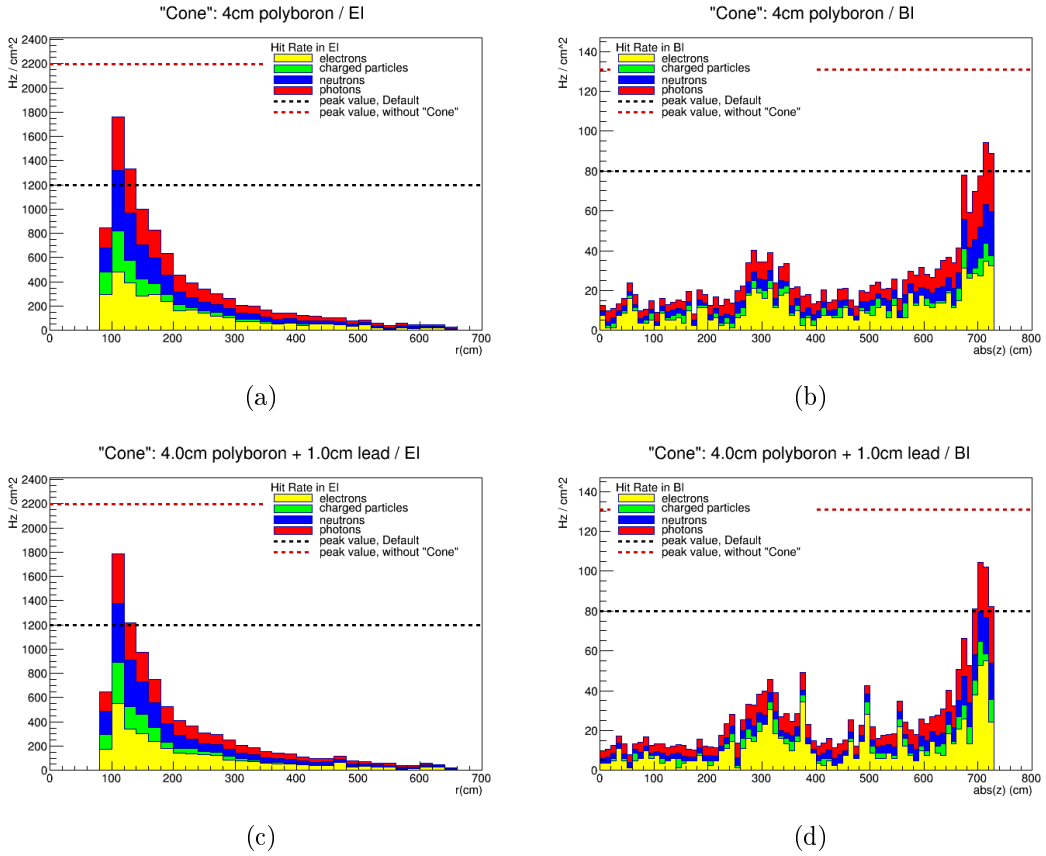

Figure 5.16.: Hit rate distributions for polyboron shieldings with and without lead cover. (a) and (b) show the hit rates for a shielding of 4 cm polyboron in the EI region and the BI region, respectively. In (c) and (d) the hit rates for a shielding with an additional 1 cm thick lead cover are presented.

In figure 5.16 the hit rates for a shielding composed of copper only, as well as for a shielding out of copper with a lead cover can be seen. In both cases the rates are just slightly lower than for a configuration without any *Cone* shielding. This result confirms the expectation, obtained from the simulations within the general scenario (see chapter 5.1.1). Therefore further studies on a copper shielding do not give additional insights and can be skipped.

The difference between a polyboron shielding and a polyboron shielding with lead coverage is presented in figure 5.16. At first, the peak values, convey the impression

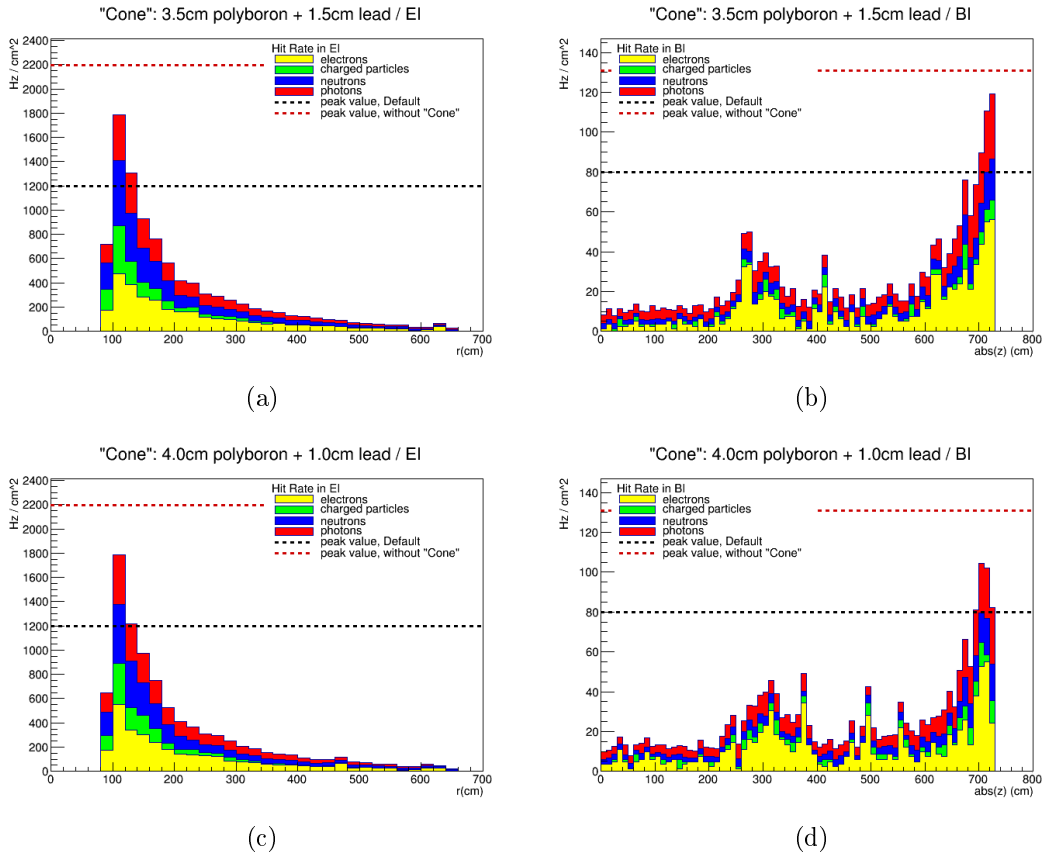

Figure 5.17.: Hit rate distributions for different shielding configurations. (a) and (b) show the hit rates for a shielding configuration with 3.5 cm polyboron and 1.5 cm lead on top, while (c) and (d) show the hit rates for a configuration with 4 cm polyboron and 1 cm lead.

of a negligible difference. However, taking also the neighboring bins into account a small rate reduction due to the lead can be anticipated. Nevertheless the difference is minor, giving a first hint on the lower relative importance of a lead cover compared to the polyboron shielding.

The figures 5.17 and 5.18 illustrate the results for different ratios of the thickness of the polyboron layer to the lead cover layer. No major effects are noticeable, nevertheless a small tendency can be recognized. Lowest rates can be achieved by a thin lead cover. Both, no lead at all, as well as thick lead layers result in higher rates. An absolute value for the optimal thickness is hard to be identified, considering the minor differences and statistical fluctuations.

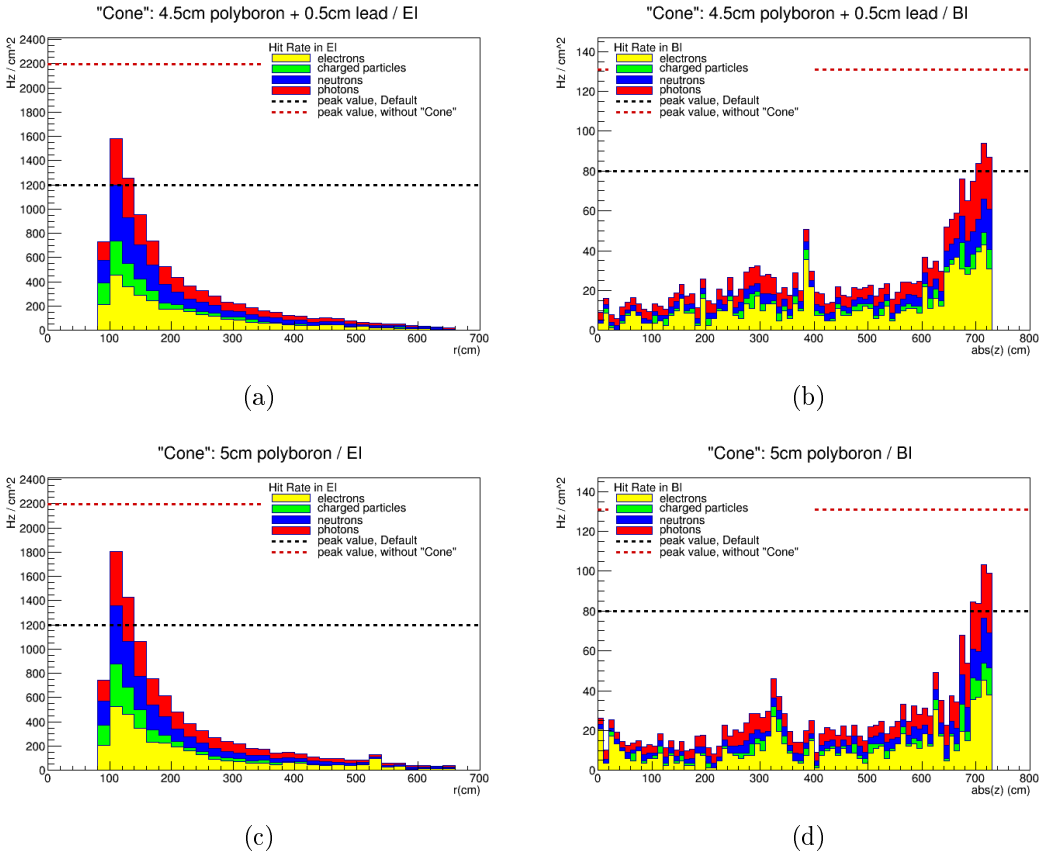

Figure 5.18.: Hit rate distributions for different shielding configurations. (a) and (b) display the hit rates for a shielding configuration with 4.5 cm polyboron and 0.5 cm lead, while (c) and (d) show the hit rates for a configuration with 5 cm polyboron and without a lead cover.

The performance of the shielding is not only defined by the overall rates but also by the particle type escaping the shielding and their energy. Further energy distributions got generated, to obtain this information in addition to more detailed insight regarding the active principles of the shielding. These energy distributions are based on the same event samples as the hit rate distributions. Figure 5.19 shows such an energy distribution plot for the default geometry and with stacked particle types. In these plots are particles displayed, which generated hits in a detector of the EI region and had a birthposition in the *Cone* region, defined as the region with $688.5\,\text{cm} \leq |z| \leq 698.5\,\text{cm}$ and $82.5\,\text{cm} \leq r \leq 168.0\,\text{cm}$. The x-axis is the logarithm of the energy of the particles in GeV, while the particles per proton-proton interaction are on the y-axis.

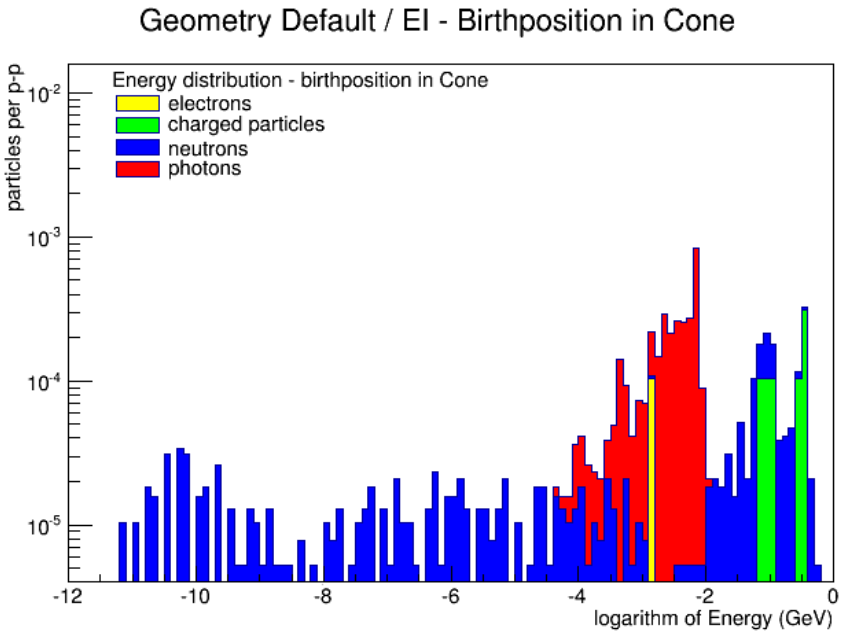

Figure 5.19.: Energy distribution of the default configuration. Presented is the logarithm of the energy in GeV of particles generating hits in the detectors of the EI region and having a birthposition in the *Cone* region.

It is hard to draw definite conclusions on the optimal ratio between the thickness of the polyboron and the lead layer for a modified shielding based only on the hit rates. Figures 5.20, 5.21, 5.22 and 5.23 present the energy distributions for different layer thicknesses of polyboron and lead. The different particle types are presented in different plots because the logarithmic scale makes a stacked histogram is not intuitive to read. The scale of the y-axis differs for the various particle types. The distributions of copper shieldings can be found in appendix A.

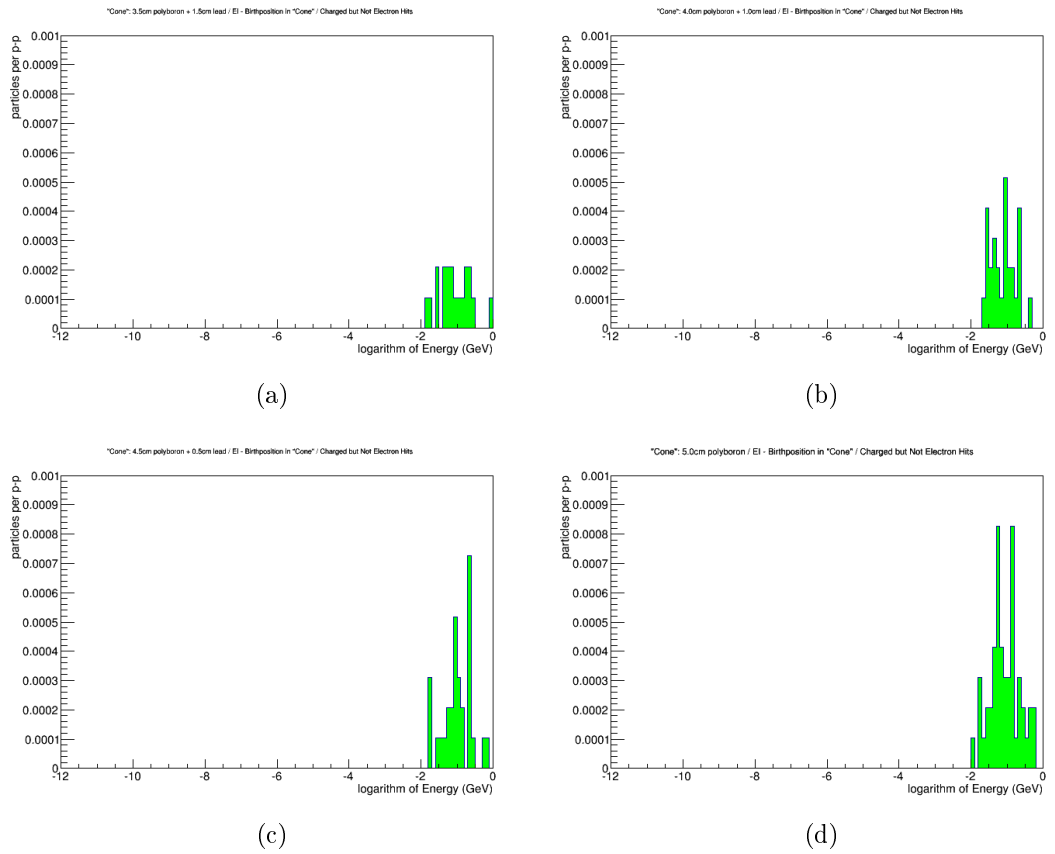

Figure 5.20.: Energy distributions of charged particles without electrons. (a) displays the distribution for a *Cone* shielding built of 3.5 cm polyboron and 1.5 cm lead. In (b) the distribution for a shielding made out of 4.0 cm polyboron and 1.0 cm lead is presented. (c) gives the distribution for a shielding composed of 4.5 cm polyboron and 0.5 cm lead, while (d) is the distribution of a shielding completely made out of polyboron.

These distributions indicate two effects of major interest. The thicker the lead cover is, the less charged particles are left. However, at the same time the amount of neutrons is increasing, especially for low energies. This suggests the charged particles to be stopped in the lead and various particles to be produced by this process, of which only neutrons can escape. The distribution for photons shows interesting features as well. For the shielding configuration without any lead cover, there are two peaks in the distribution, one roughly at 10 MeV and another one in the MeV region further below. Already half a centimeter of lead blocks the majority of these photons, especially if their energy is low. By increasing the thickness of the lead layer this effect does not grow linearly, but significantly slower.

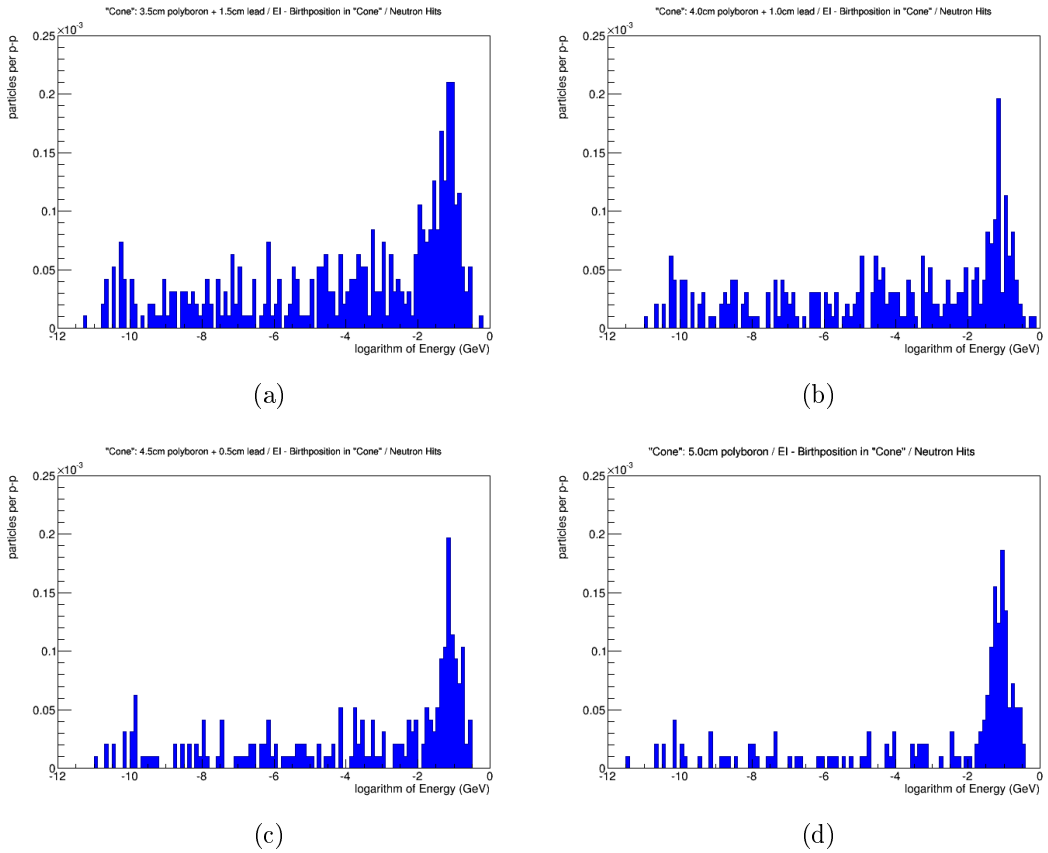

Figure 5.21.: Energy distributions of neutrons. (a) shows the distribution for a *Cone* shielding built of 3.5 cm polyboron and 1.5 cm lead. In (b) the distribution for a shielding made out of 4.0 cm polyboron and 1.0 cm lead is presented. (c) gives the distribution for a shielding composed of 4.5 cm polyboron and 0.5 cm lead, while (d) is the distribution of a shielding completely made out of polyboron.

The energy distributions of the different particle types therefore underline the conclusion drawn from the hit rates, as the processes resulting in smallest rates for a thin lead cover are reflected in more detail. This leads to the conclusion, that the optimal shielding in the *Cone* region of the *NSW* will be composed of polyboron with a thin lead cover. A thicker lead layer does not increase the shielding performance substantially but just adds to the weight of the shielding, which is strictly limited.

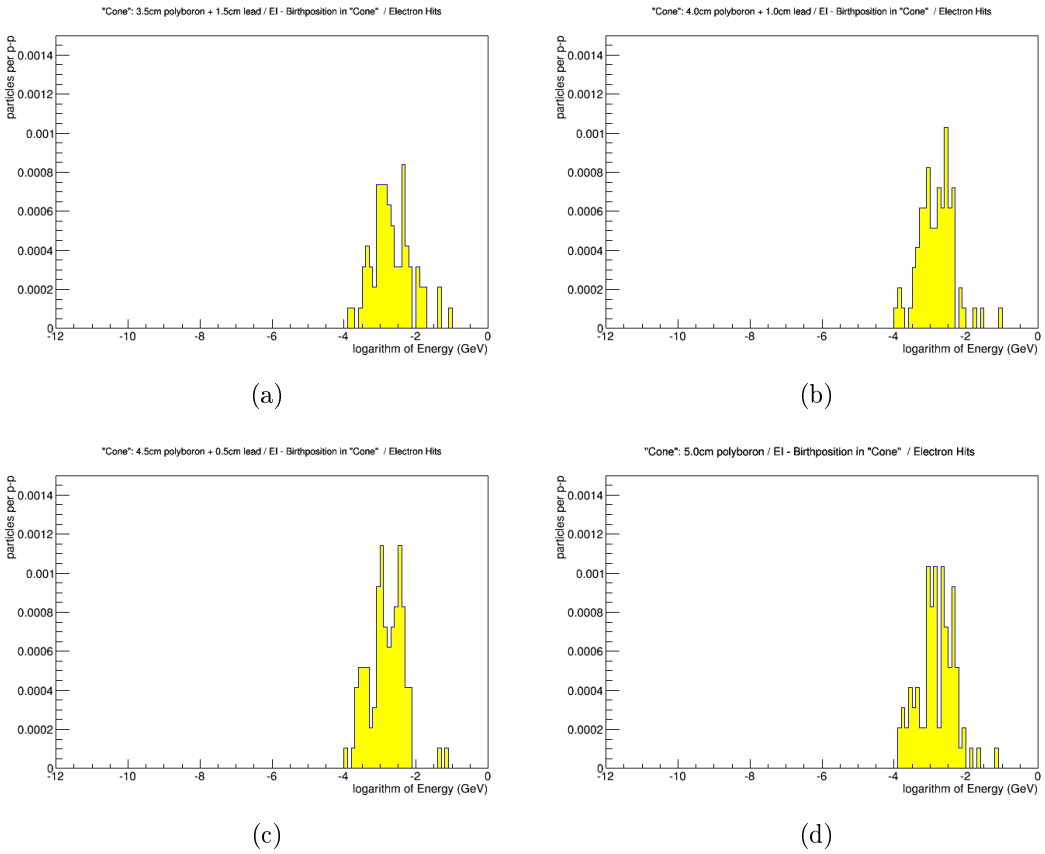

Figure 5.22.: Energy distributions of electrons. (a) presents the distribution for a *Cone* shielding built of 3.5 cm polyboron and 1.5 cm lead. In (b) the distribution for a shielding made out of 4.0 cm polyboron and 1.0 cm lead is displayed. (c) gives the distribution for a shielding composed of 4.5 cm polyboron and 0.5 cm lead, while (d) is the distribution of a shielding completely made out of polyboron.

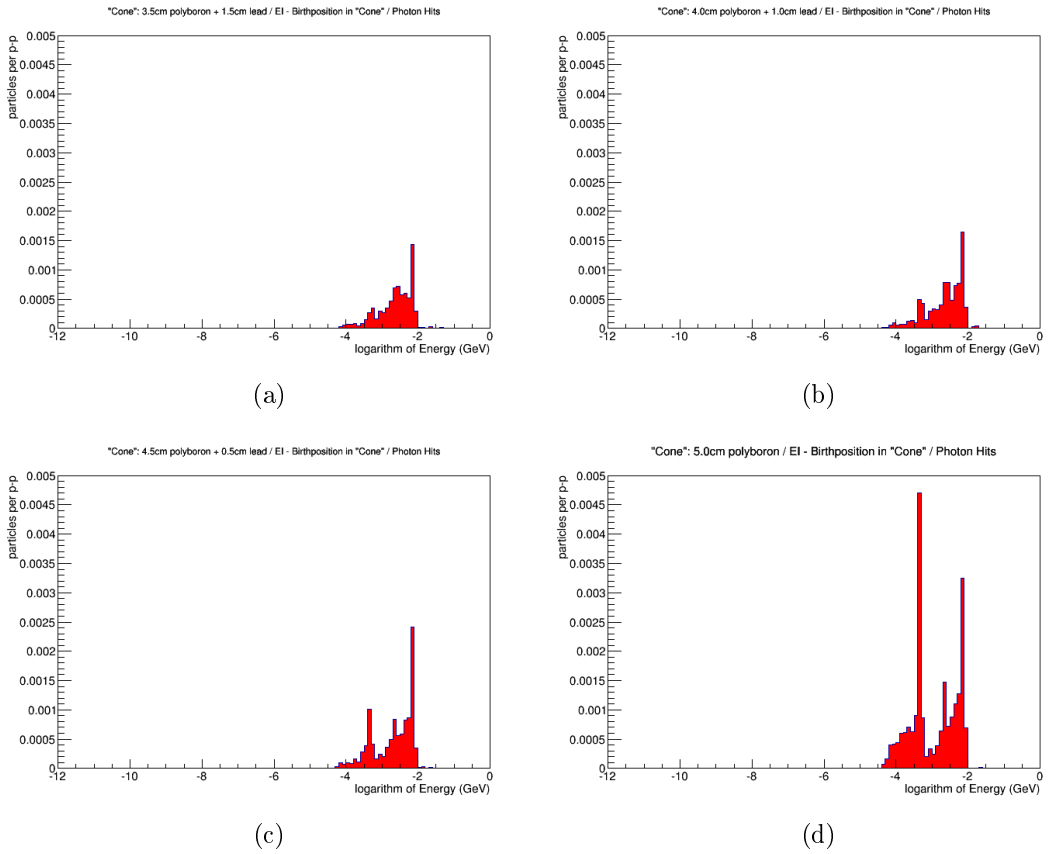

Figure 5.23.: Energy distributions of photons. (a) displays the distribution for a *Cone* shielding built of 3.5 cm polyboron and 1.5 cm lead. In (b) the distribution for a shielding made out of 4.0 cm polyboron and 1.0 cm lead is presented. (c) gives the distribution for a shielding composed of 4.5 cm polyboron and 0.5 cm lead, while (d) is the distribution of a shielding completely made out of polyboron.

5.2.2. Studies on cladding gaps in the Hub

An additional objective of the studies within the restricted scenario concerns investigations on a potential improvement of the *Hub* shielding without an increased overall thickness. Most of the chambers of the *Small Wheel* are supported by the tube or the *Hub* respectively (see chapter 3.1). The required support structures are mounted directly on the copper layer of the *Hub*. Therefore some regions in the *Hub* shielding are not covered by polyboron and lead layers (see figure 5.24). This situation will be similar for the *NSW*.

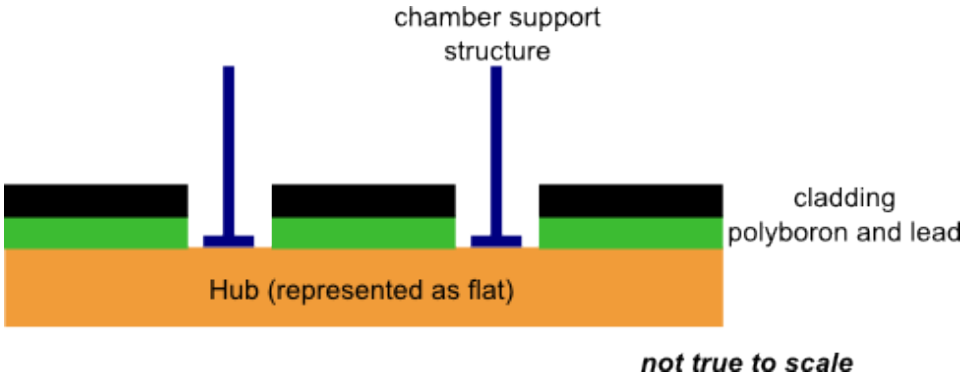

Figure 5.24.: Sketch of the gaps in the *Hub* cladding due to support structures of the chambers.

Simulations were performed to study the effect of cladding gaps with respect to a continuous cladding. This study aims to verify the importance of an improved cladding in this region. Therefore no realistic cover is assumed, but a continuous cladding, that neglects the necessity of the support structures. The *Cone*-shielding configuration with 4 cm polyboron and 1 cm lead was chosen for this study. Figure 5.25 presents the direct comparison for the *Cone* configuration with gaps in the cladding as they are needed for the actual *Small Wheel* chambers and for a continuous cladding.

Like expected the hit rates in the EI are significantly lower in case of a continuous cladding, indicating that further studies on this part of the shielding are required to optimze it further. The corresponding energy distributions for particles with birthpositions in the *Hub* region can be found in appendix A.

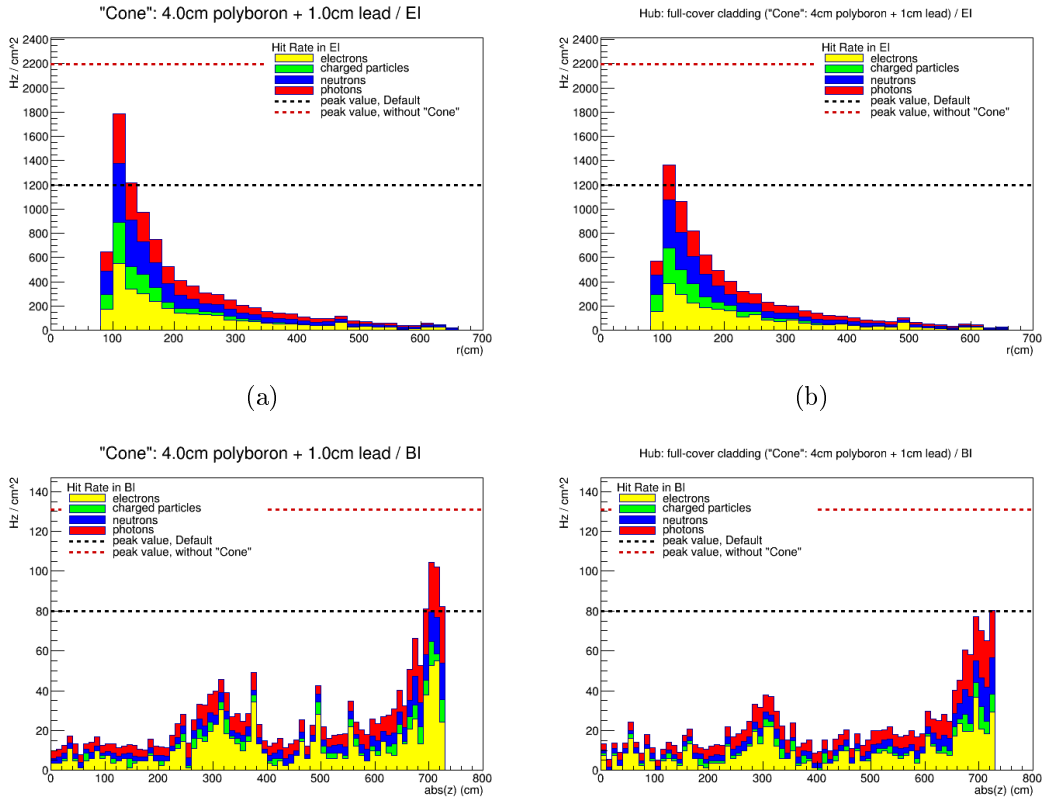

Figure 5.25.: Comparison of hit rates for a *Hub* with and without cladding gaps. The *Cone* shielding is composed of 4 cm polyboron and 1 cm lead. (a) displays the hit rates in the EI region with cladding gaps in the *Hub* and (c) the hit rates in the BI region for the same configuration. (b) and (d) show the corresponding rates when the *Hub* cladding is continuous.

6. Conclusion on the simulation studies

The presented studies were done in the context of the preparations for the *New Small Wheel* upgrade. The shielding configurations simulated were not just adapted to the new geometry, but followed also closely the discussions in the *NSW* group. By providing results to the discussion, substantiated decisions could been taken. The results of the two scenarios of the study are made available to the community in *ATLAS* internal notes.

While the results of a general scenario during the first phase were intent to be preliminary to support the discussion on the *New Small Wheel* design, the second phase aimed for an actual design recommendation, especially for the *Cone* structure of the shielding and was therefore carried out within a restricted scenario. The result of these studies showed, that within the given constraints for the shielding a combination of a polyboron shielding with a thin lead layer leads to the lowest rates, while a copper component does not increase the shielding performance significant. Besides other considerations like engineering limitations, the final design of the shielding reflects this result, as a 4 cm thick polyboron layer with a 1 cm lead cover is planned [27].

In the cladding of the *Hub* of the shielding there are holes for the support structures of the detectors. The effects of these holes were investigated during the studies within a restricted scenario. It is shown that the rates of the background radiation is reduced by nearly a third, when the gaps in the cladding are closed. Therefore further studies and engineering efforts are required to achieve a more optimal design in this region.

Design and Construction of a Test Facility for Gaseous Detectors

7. Conceptional idea and demand for a test facility

The research on detector systems is a long term task, including a lot of gradual developments. A facility to test and characterize new developments is absolutely necessary to enable systematical research. The design and construction of such a facility is an important step to strengthen the commitments of the University of Würzburg in the detector research, by enabling independent local development as well as the execution of measuring and testing tasks in collaboration projects.

The Würzburg *ATLAS* group is mainly involved in the maintenance and development of the Muon Spectrometer and in physics searches including muons. Therefore the described test facility will be used mainly for research on muon detectors, making cosmic muons a natural choice for usage at the test facility, as they are a main part of secondary cosmic rays. Those muons are produced in the atmosphere by decays of charged mesons. On ground level they have a flux of about $1\,\mathrm{cm}^{-2}\mathrm{min}^{-1}$. The distribution of the incident angle is proportional to $\cos^2\theta$, while the energy spectrum is more complex with a mean energy of 4 GeV. [28]

As cosmic muons are in time as well as in space statistically distributed, a trigger system is needed to acquire meaningful data. But also the possibility of a trace reconstruction would also be helpful in many cases. This leads to at least two layers of segmented detectors, to enclose the tested detector from below and above, driving the design of the facility.

The University of Würzburg is part of the *New Small Wheel* upgrade project of the *ATLAS* experiment, taking over several tasks in the design and construction of the *Micromegas* chambers. By this, the test facility has to be capable of validating the segments of these chambers, the University of Würzburg is participating in production. Nevertheless the test facility was not planned for this purpose alone but it has to be flexible enough to be used in any kind of future project that may be of interest.

Finally such equipment gives the opportunity for increased teaching as part of the physics student's education in this field. Not only Master and Bachelor theses can be part of this increased teaching effort, but also an advanced laboratory course could be a possibility.[1] As a result of possible teaching usage of the test facility, it has to be designed in such a way, that also inexperienced students can work safely and intuitively with all of its components.

The design and construction of the test facility has been performed with keeping these basic aspects in mind. The design and construction of the system as well as first measurements proofing its functional capability and identifying some of its characteristics are described in the following chapters.

[1] Already during the construction phase of the test facility teaching was done by means of this project. Several Bachelor theses and one Master thesis were made on topics related directly to the project. In the following only those theses will be mentioned that were supervised by the author of this thesis and had relevant implications on the project.

8. Structural enhancement of the lab

Right before the begin of the project, the Würzburg *ATLAS* group moved into another building on a new part of the campus. In this building no room was prepared as a lab. Therefore the room chosen for the project had to be enhanced.

The fire protection was already adapted before moving. The room is also declared as a controlled area with respect to the applicable regulations of radiation protection, allowing to operate with radioactive sources, that could be used for aging tests of detectors for instance.

In addition to the standard electric power supply of the room, circuits particularly for experimental purpose were installed. Those 12 circuits have a separate fuse each, accessible from inside the room. Two independent phases, each corresponding to six of the circuits, ensure the ability of preventing interference of different components via the power circuits. All electrical sockets connected to those circuits are secured with a common emergency switch. Finally there is also an independent ground accessible.

A gas cabinet was installed in the room, allowing the usage of gas cylinders inside the building. As there is no exhaust air system, only non-toxic and non-flammable gas mixtures can be used at the moment.

The floor was strengthened where the frame of the facility (see chapter 9) is placed, as well as below the gas cabinet. A gray painted wooden board, having no complete interruption of the wooden fibers at any position, is embedded in the floor beneath the frame. This board distributes forces evenly to a wall below, especially built for this reason. An overall weight of three tons can be placed on this board.

9. The Frame of the facility

The main support structure of the facility is an aluminum frame. It has to support the detector that will be tested as well as the trigger detectors, while being as adaptable as possible. The dimensions were chosen with respect to the Micromegas detector parts Würzburg participates in building. An integrated absorption layer allows to prevent triggering on low energetic muons, as the probability of multiple scattering processes is much higher for those. Multiple scattering can complicate track reconstructions for instance. In figure 9.1 a schematic sketch of the facility as well as a photograph of the finished frame can be seen side by side.

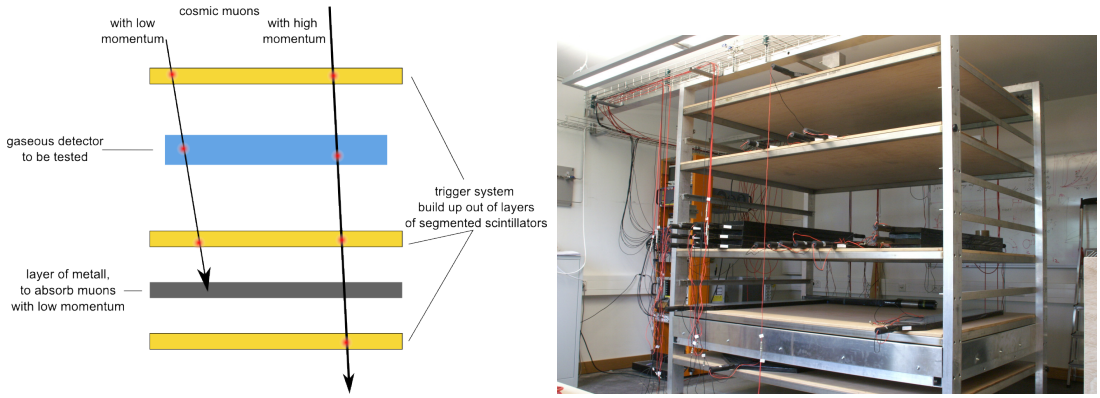

(a) (b)

Figure 9.1.: A schematic sketch of the facility (a) and a photograph of the frame (b).

9.1. Mechanical details of the frame

The frame is built of rectangular aluminum tubes and has an outer dimension of 210 cm times 150 cm in the ground area and a height of 225 cm. This leads to a usable area of 200 cm times 150 cm, which is big enough for *NSW* chambers (SM2 modules have a size of 1821.5 mm times 1350 mm [29]). An absorption layer is positioned at about 52 cm to 60 cm over floor level (see chapter 9.2). Below this

absorber there is the support for one shelf, while above the absorption layer there are 8 supports for shelves. Those supports are made from steel angles, each arm measuring 40 mm with a material thickness of 4 mm. They are mounted between the cornerstones at the short sides of the footprint of the frame. Above the absorption layer the angles are positioned with a distance of 20 cm to each other, giving the opportunity to vary the height of the shelves as it is needed for a given project.

Four shelves are available to configure the frame as required, as they can be freely moved to different supports. The shelves are composed of a 16 mm thick beech multiplex board and a 40 mm times 40 mm steel tube with a wall thickness of 4 mm on each long side. The wooden boards of the shelves are lying directly on the supports on the small side, while the tubes on the long side reduce the sag of the shelf. If necessary the tubes can be fixed to the frame with screws at all four corners (see figure 9.2). A grid of lines with ten centimeters distance, that is helpful for positioning, is printed on top of the shelves (see also chapter 9.3).

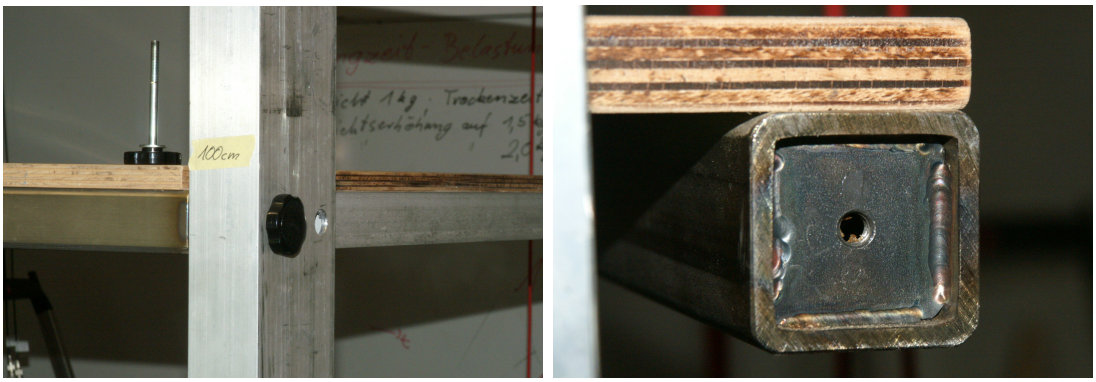

(a) (b)

Figure 9.2.: Pictures of the shelf mounting. On the left hand side a shelf mounted on one of the supports can be seen. The horizontal metal structure on the left side is the steel tube that prevents the board from sagging, while the structure on the right side of the picture is the steel angle on which the board is lying on. Two screws can be seen on the photograph, too. With one of the screws the shelf is fixed to the frame, while the other one is lying one the board, just for illustration. On the right hand side a picture shows one end of a steel tube. On both sides of the tube near the end a plate is welded inside, where the thread for the screws is cut in. The hole in the post of the frame has a big clearance to ensure that the shelf is lying on the angles and not on the screws.

A drift tube is placed at the top of the frame giving an additional opportunity for gas monitoring (see also chapter 11). Due to the large number of trigger detectors a lot of cables are needed. To allow more structured wiring, cable trays are mounted at the top of both long sides of the frame, too.

9.2. The absorption layer

For many studies a track reconstruction of muons can be valuable. Multiple scattering of low momentum muons is reducing the precision of such a reconstruction. The absorption layer in the frame provides a tool to avoid triggering on such low momentum muons. By having scintillation detectors also below the absorber and requesting a signal from them, too, only those muons are triggered, which had enough energy to pass through the material.

Figure 9.3.: Picture of the absorber showing the internal structure. The 42 steel sheets of the absorber can be seen as well as one of the cover panels, attached for safety reasons.

Typically metal is used for such absorbers as these have a high density and a low space consumption. The absorber in this frame is built of carbon steel sheets, as it is the most cost-efficient material (see figure 9.3). The amount of material was driven by the load capacity of the floor. The strengthened part of the floor, where the setup is placed, can carry three tons in maximum (see chapter 8). With the possibility to have a payload of a few hundred kilograms, the absorber should not weigh more than 2 tons in addition to the weight of the frame itself and the trigger detectors. The density of steel is about $7.85\,\frac{\mathrm{g}}{\mathrm{cm}^3}$. For an area of $3\,\mathrm{m}^2$ 2 tons result in an 8.5 cm thick steel absorber. 42 2 mm thick sheets were stacked, staying below the maximum. The sharp edges of the sheets were not worked over, therefore a cover panel was attached on all sides, to reduce the risk of accidents.

To get an impression on the energy loss of the muons in material the Bethe formula is often used. It gives the mean rate of energy loss by moderately relativistic charged heavy particles per distance [28]. The stopping power can be given in the form [30]

$$-\left\langle \frac{\mathrm{d}E}{\mathrm{d}x} \right\rangle = K\frac{Z}{A}\frac{1}{\beta^2}\left[\frac{1}{2}\ln\left(\frac{2m_e c^2\beta^2\gamma^2 Q_{\max}}{I^2}\right) - \beta^2 - \frac{\delta}{2} + \frac{1}{8}\frac{Q_{\max}^2}{(\gamma M c^2)^2}\right] + \Delta\left|\frac{\mathrm{d}E}{\mathrm{d}x}\right| \ ,$$

where $-\left\langle \frac{\mathrm{d}E}{\mathrm{d}x} \right\rangle$ is the mean energy loss per distance and density. c is the speed of light in vacuum and β and γ are the common kinematic variables. m_e is the mass of the electron, while M is the mass of the incident particle. Z is the atomic number, A the atomic mass of the absorber and I the mean excitation energy of the material. δ is the density effect correction. $Q_{\max}$ is the maximum kinetic energy that can be transferred to an electron in a collision. The factor K is given by

$$K = 4\pi N_A r_e^2 m_e c^2 \ ,$$

with the Avogardo's number N_A and the classical electron radius

$$r_e = \frac{e^2}{4\pi\epsilon_0 m_e c^2} \ .$$

The elementary electric charge is symbolized by e and ϵ_0 is the vacuum permittivity. $\Delta\left|\frac{\mathrm{d}E}{\mathrm{d}x}\right|$ is the relevant contribution of Bremsstrahlung to the stopping power. It is given by [30]

$$\Delta\left|\frac{\mathrm{d}E}{\mathrm{d}x}\right| = \frac{K}{4\pi}\frac{Z}{A}\alpha\left[\ln\left(\frac{2E}{M_\mu c^2}\right) - \frac{1}{3}\ln\left(\frac{2Q_{\max}}{m_e c^2}\right)\right]\ln^2\left(\frac{2Q_{max}}{m_e c^2}\right) \ .$$

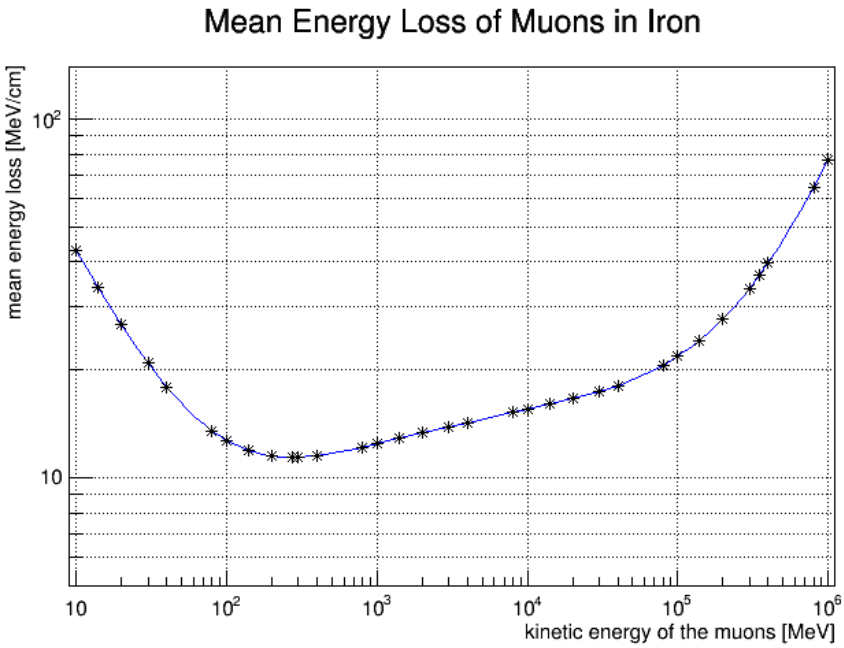

Figure 9.4.: Mean energy loss of muons per distance in iron. The points are calculated with data from the Particle Data Group [31]. The line is only an interpolation between these points.

M_μ is the mass of the muon, E is the energy of the incident particle and α is the fine-structure constant.

Carbon steel, that is used for the absorption layer, can be treated as iron in very good approximation for calculating the stopping power. Carbon steel is an alloy out of iron and less than 1% carbon having nearly an identical density to pure iron. Calculating the mean excitation energy of a material and the density effect corrections is non trivial, but those values as well as tables with already calculated values for the stopping power of a given material can be found on the web pages of the Particle Data Group [31]. This was used to plot the mean energy loss per distance in iron as a function of the kinetic energy of the muon in figure 9.4. Of course there is no way to conclude from the mean energy loss on the energy loss of a given muon, but nevertheless it can be estimated that most of the muons with less than 100 MeV kinetic energy will be stopped in the absorption layer.

9.3. A coordinate system of the facility

The reconstruction of a muon track and even a more locally specialized offline triggering is only possible if the information of the position of all detectors relative to each other are known. Generally this information can be given in any user-defined way.

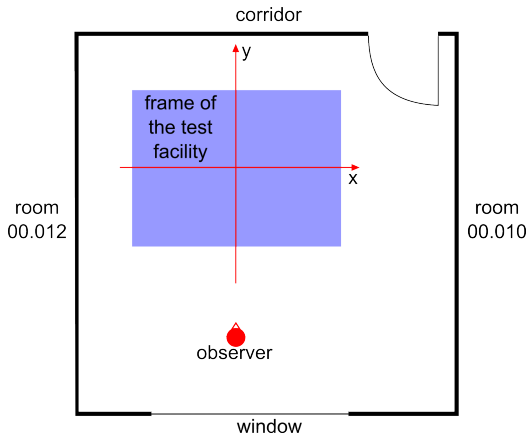

Figure 9.5.: Sketch of a coordinate system for the test facility. The drawing is not to scale. The orientation of detectors is given in respect to the observer in this system.

Nevertheless during the first measurements the following coordinate system proofed to be working well (see figure 9.5). A positioning system is already drawn on all shelves. In both directions the exact center of the frame is given by red lines. With respect to these lines there are parallel lines every 10 cm. The x-axis is parallel to the main corridor of the building. The positive x-axis is pointing towards room 00.010 while negative x-axis is pointing towards room 00.012. The y-axis is oriented from the window-side to the door-side with the positive half-line is pointing towards the door. The x- and the y-axis are zeroed at the middle of the frame indicated by the red lines on the shelves. Z-direction is upwards with the 0-position on the surface of the first shelf above the absorber. By this negative z-numbers indicate a position below the absorber. The surface of the shelf below the absorption layer is therefore at -33 cm.

The position of a trigger detector is given by its left lower corner close to an observer, while standing between the frame and the window and looking in y-direction towards the frame (see figure 9.5). In addition the orientation of a scintillator parallel to the x- or the y-axis and the position of the detector's photo-

multiplier (see chapter 10) towards plus- or minus-direction defines the detector completely.

A definition using always the same point of a detector, for example the left lower corner close to the photomultiplier, would not need to define the position and orientation of an observer. Instead two detectors stacked on top of each other with opposite orientations would have different coordinates, making the identification of detector stacks more difficult than in the system described above.

10. Construction of the trigger detectors

One of the main components of the test facility are the detectors used for trigger and rough trace-reconstruction purposes. Already in the very first concept phase it was decided to use segmented layers of scintillation detectors. The advantage of scintillation detectors is the long experience of science and industry in those detector systems, their relative low cost and stability as well as their low maintenance efforts. It was decided to have 30 pieces in three different widths to increase the flexibility in usage of the detectors. The conversion of light signals into electrical signals is done by photomultiplier tubes, as they are again well known systems. The assembly of the different components was performed within this project to be able to customize the details as well as keeping track of every step.

10.1. Preparatory work and studies

One of the two main components of the trigger detectors is the scintillation material itself. Solid plastic scintillators are the best choice for such a project as the have a good time response and are relatively robust and easy to handle. They are also inexpensive due to the good processability. BC-408 manufactured by Staint-Gobain has been chosen [32]. 30 scintillators in three different widths were purchased. All of them are 1200 mm long and 25 mm thick. 14 pieces have a width of 100 mm and another 14 pieces have a width of 200 mm. In addition 2 large pieces with 700 mm width were bought to be used as trigger below the absorption layer. The second main component are the photomultiplier tubes. The chosen photomultiplier tubes from Hamamatsu have a round light entry window and a sensitive area with a maximum diameter of 25 mm [33] [34]. To transmit the light created in the scintillator into the photomultiplier a light guide is necessary. The functional capability of the photomultiplier have to be tested too, before detector assembly.

10.1.1. Design of the light guides

To effectively utilize the light generated in the scintillators, light guides optimized for the given components, have to be designed. A smooth geometry transferring the big rectangular surface of one end of a scintillator to the small round surface of the photomultiplier will ensure the highest light yield. In the early design phase it already became obvious that such a geometry is very difficult to produce with conventional methods as one piece, therefore two parts were designed.

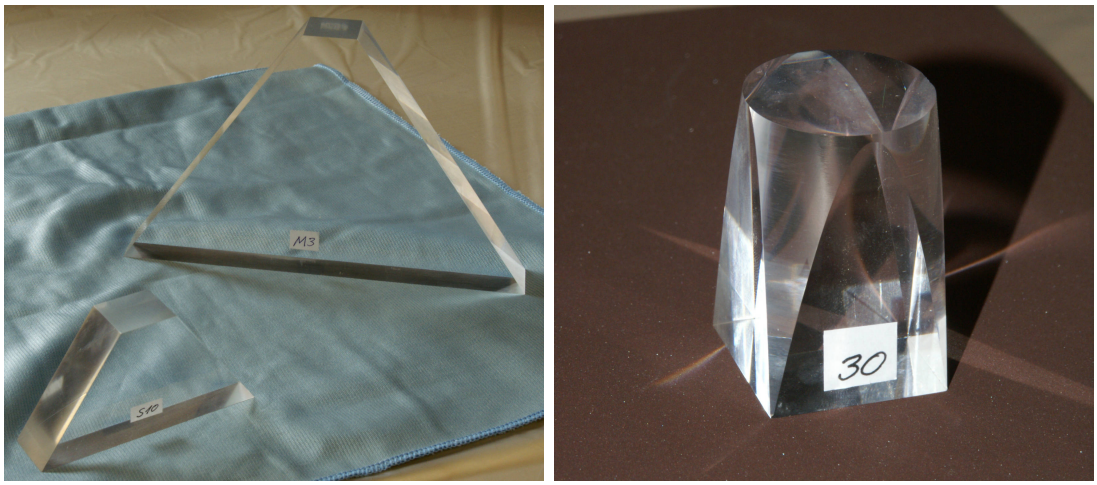

(a) (b)

Figure 10.1.: Photos of the light guide parts. In (a) trapezoidal parts for the 100 mm and the 200 mm wide scintillators can be seen. In (b) the piece transferring the rectangular shaped surface into a round shaped surface is shown.

One part has a trapezoidal base and transfers the rectangular shape of the end of the scintillator into a square surface with an edge length of 25 mm. As there are three different types of scintillators with different widths, of course also three different versions of these trapezoidal parts are necessary (see figure 10.1). The second part of the light guide is a part that transfers the squared surface with an egde length of 25 mm into a round surface with a diameter of 25 mm (see figure 10.1). This part is the same for all the scintillators. Finally the two parts of the light guide can be glued onto each other and between the scintillator and the photomultiplier to get a smooth light transition between those two parts (see also chapter 10.2).

A natural choice for the material of these parts is acrylic glass, as it has on the one hand a similar refractive index as the scintillator material and nearly the same

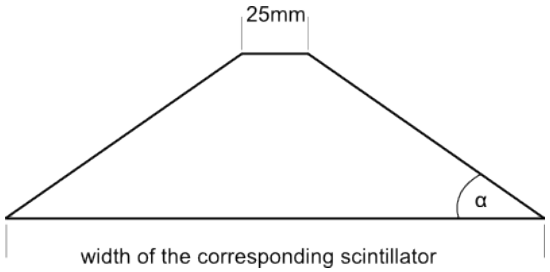

Figure 10.2.: Sketch of the trapezoidal part of the light guide. The angle α is 55° for 100 mm and 200 mm wide parts and 30° for 700 mm wide parts.

one as the silicate glass window of the photomultiplier, on the other hand it is easy machinable. The trapezoidal part can be milled, while the other part can be lathed. All these parts were produced in the mechanical workshop of the institute. Simulations of the light propagation inside the detectors were the topic of a bachelor thesis [35]. In particular the optimal angle of the trapezoidal parts was studied. The efficiency depends only slightly on the angle, therefore the angles were defined from a practical point of view. The inner angles of the parts for the 100 mm and 200 mm wide scintillators are 55° while the angle of the part for the 700 mm wide scintillator is 30°, as the parts otherwise became to long (see figure 10.2).

10.1.2. Studies on the photomultipliers

The photomultipliers are an essential part of the trigger detectors. Therefore it is advisable to test them before assembling the detectors. From the data sheet it is expected that for a maximum supply voltage of -2000 V the dark current is not higher than 200 nA [33] [34]. Studies on the possibility to measure the dark current of the individual photomultiplier was part of a bachelor thesis [36]. Within the thesis it is pointed out, that it is not possible to do so, neither with an oscilloscope nor with integrators built by the workshop, as the relevant signals were to short in time and similar to the noise of the electronics.

Independent from the bachelor thesis, the necessity to acquire information about the photomultiplier's behavior remained. Therefore the dark current peaks of the photomultipliers were counted, instead. After exposing a photomultiplier to bright light like daylight its sensitivity can differ for some time from the nominal value. To ensure controlled and stable conditions the photomultiplier were darkened during the measurement, as well as already 45 minutes beforehand. Therefore a special PVC cover was designed and built. The number of counts within 100 s was measured for three different supply voltages, -1200 V, -1400 V and -1600 V, as well as the

supply current and the temperature during the measurements. The counting of the peaks was done with an oscilloscope, triggering on the falling edges at -200 mV. For two arbitrarily chosen photomultipliers the dark current peak rate was measured for negative supply voltages from 1200 V to 1700 V in steps of 20 V, to get an impression of the general behavior. Those measurements were done after several days of darkening the photomultiplier.

The first result was that the necessary supply currents were equal for the different photomultipliers. The current drawn is about 200 $\frac{\text{nA}}{\text{V}}$, which is the power consumption due to the voltage dividers within the photomultipliers. As this value stays the same for all photomultipliers and for all supply voltages, fundamental damages or relevant disruptive discharges between the dynodes can be excluded. More detailed information on the functional capability of the photomultipliers is of course given by the count rates (see figure 10.3). In figure 10.3(a) the dark current rates of two different photomultipliers can be seen. The behavior of those arbitrarily chosen photomultiliers is obviously different, but both have a continuously rising rate with respect to the supply voltage, as well as no triggered dark current peaks at all for voltages below around -1350 V. In 10.3(b) and 10.3(c) the rates for all the photomultipliers can be seen. At higher supply voltages the rates of the photomultipliers are very different, but for -1200 V all of them have no triggered peaks at all. As a summary it can be noticed, that all of the photomultipliers work well and supply voltages below -1400 V should be preferred. In 10.3(d) the rates are plotted with respect to the temperature during the corresponding measurement. No trend can be seen in this data, meaning that no impact on the dark current by the temperature within usual limits can be expected.

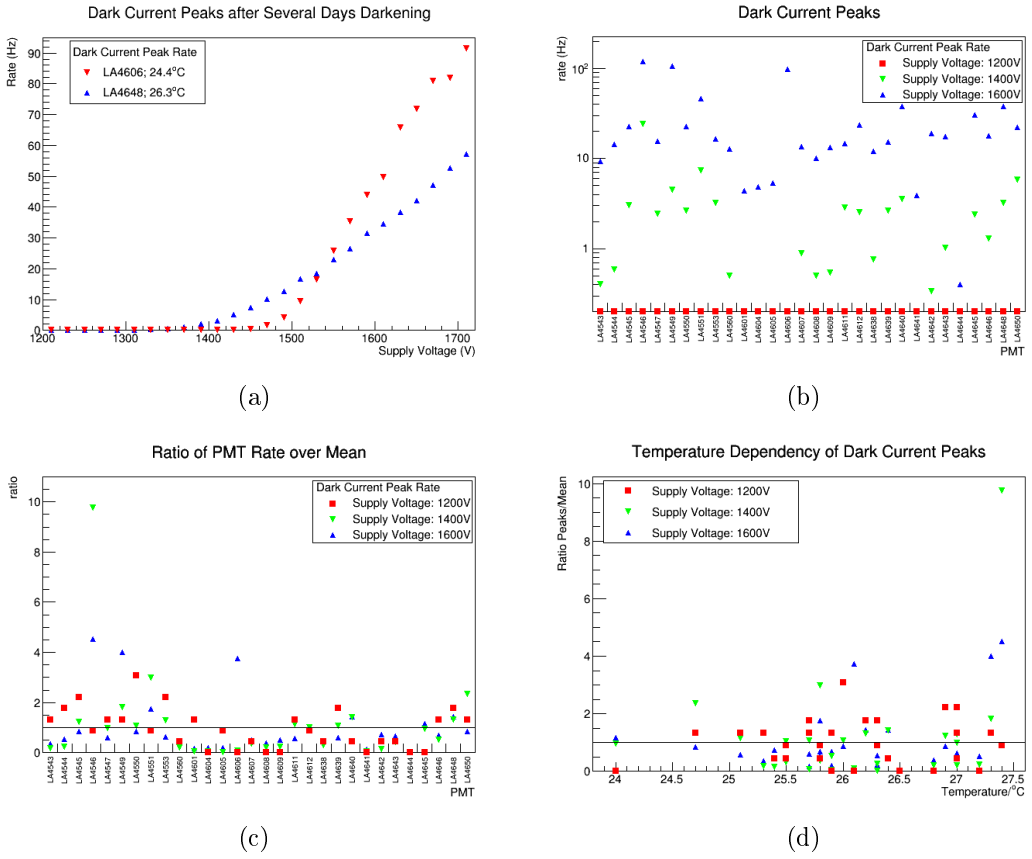

Figure 10.3.: (a) shows the dark current peak rate of two arbitrarily chosen photomultipliers for supply voltages between -1200 V and -1700 V. In (b) and (c) the dark current rates for all the photomultipliers can be seen. In (b) the rate is given in absolute numbers, while in (c) the ratio of the rate over the mean of the rates of all photomultipliers is shown. (d) gives the ratio of the rate over the mean with respect to the temperature at which the corresponding photomultiplier was measured.

10.2. Assembly of the detectors

The assembly of the trigger detectors includes several working steps, not being feasible for a single person. Therefore student assistants were contributing to the assembly, especially in the manufacturing stage.

The basic steps of assembly are the same for the three different scintillator dimensions. In a first step the two parts of the light guides were glued to each other, afterwards the light guides are glued on one end of the scintillator and as the last gluing step the photomultiplier has to be fixed to the light guides. Finally the whole detector is wrapped.

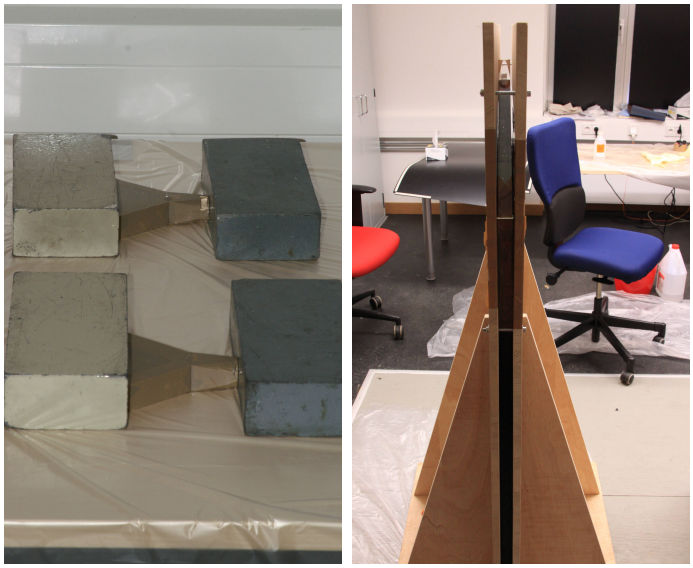

(a) (b)

Figure 10.4.: Photos of gluing light guide parts and a light guide to a scintillator. (a) shows the curing process of light guide components. The position of the parts is fixed by pressing them between lead bricks. (b) (by Dominik Köth) shows, how a light guide is glued onto a 700 mm wide scintillator. For fixing the parts during curing special frames were built.

The gluing of the scintillators and the light guide components differs from the gluing of the photomultiplier to the light guide, as the mineral glass of the photomultiplier window needs to be handled differently. After testing different adhesives, BC-600 optical cement from Saint-Gobain [37] was used for gluing the scintillators and light guides, as it gave the best results. Before gluing the surfaces were roughened with sandpaper with a grit size of about 300 meshes per inch, and carefully cleaned with methanol. After applying the adhesive on both pieces to be glued, the curing

takes about 24 hours. During this time the two parts are fixed to each other under mechanical pressure (see figure 10.4). For gluing the photomultiplier on the light guides different adhesives were tested, too. The best performance was achieved by MS Clear HS from Kent [38]. For using this adhesive the surfaces of the light guides do not have to be roughened but to be polished with a very fine grit size and carefully cleaned, while the glass of the photomultiplier is only cleaned. The curing time is at least 24 hours. During the curing the pieces to be connected must not be fixed, because the glue is shrinking and the connection is very weak if the parts can not move correspondingly.

The basic intention of wrapping scintillation detectors is to keep the scintillation light inside the detector, while avoiding ambient light to get in. There are different materials used for wrapping scintillators and even painting them with special reflective paint is an option. The detectors used in this test facility were wrapped with an inner layer of aluminum foil and an outer layer of opaque PVC. On the bigger surfaces PVC sheets were used while the rest was wrapped with PVC tape.

The very common approach of wrapping with aluminum and PVC provides a good time resolution of the detectors, as the light is mostly reflected by total internal reflection, as there is a very thin air gap between the scintillation material and the aluminum foil. In contrast to diffuse reflection the determinate angles of total reflection lead to a shorter light pulse arriving at the photomultiplier. In addition the PVC is optically enclosing the detector and it also provides mechanical protection, up to a certain degree.

10.3. Experiences with the trigger detectors

One of the adhesive connections between the scintillator and the light guide, as well as a different connection of the photomultiplier to the light guide, had not the expected quality. Therefore those connections were disassembled, for gluing them a second time. By doing so the feasibility of repairing broken bonds is also proven. To remove the remains of the cured adhesives the scintillation material and the acrylic glass are best polished with sandpaper. To remove the remains from the photomultiplier's mineral glass two steps are necessary, larger remains can be removed carefully with a razor blade (see figure 10.5). Afterwards the remaining thin layer of adhesive can be removed with a microfiber cloth and methanol.

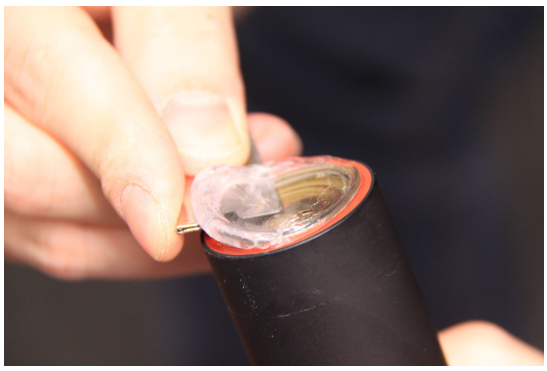

Figure 10.5.: Picture (by Dominik Köth) of removing adhesive remains from a photomultiplier using a razor blade.

The efficiency of three detectors were measured already during the manufacturing phase using an improvised setup, to recognize potential serious mistakes early in the process. The efficiencies were all higher than 97%. After finishing the detectors and the framework for data acquisition the optimal supply voltage for every detector, as well as the efficiency with this supply voltage were measured within a bachelor thesis [39]. To identify the optimal supply voltages the signal rates as function of the voltage were measured and associated with the corresponding efficiencies. When the detectors are driven with the optimal supply voltage, all measured efficiencies are between 93.7% and 99.3%, with only 7 detectors having a efficiency below 97%. A table on all detectors including the optimal supply voltages and the efficiencies can be found in appendix B.

During operation it become obvious that the mechanical weak point of the detectors is between the two parts of the light guides. So far three times one of these connections broke by handling the detectors carelessly. To avoid this in future, a prototype of a frame was designed to transfer forces from the photomultiplier directly to the trapezoidal part of the light guide (see figure 10.6). The frame is designed in a way that the detectors are still stackable by changing there orientation in every layer. The design was adopted for the different widths of the detectors. Frames for one half of the detectors were produced for a long term test.

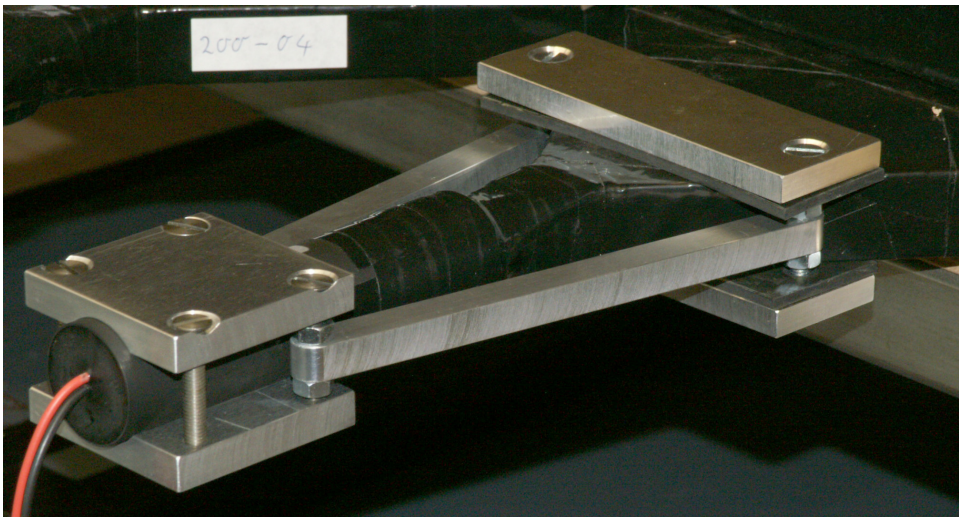

Figure 10.6.: Picture of the frame prototype to transfer the forces from the photomultiplier directly to the trapezoidal part of the light guide. To adjust the frame to the individual detector, rubber spacers are used on the light guide side and in addition the position of each end of the connectors between the two parts can be tuned separately.

11. The gas supply system

The test facility is designed for investigation of gaseous detectors. The gas system needed for that was in its main parts built by Stefan Czerwenka within his master thesis. The system includes an installation for gas mixing and controlling the mass flow and pressure of the gasmixture. The pressure can be independently set for two consecutive sections in the gas system. The pressure ranges of one section is optimized for the use of drift tubes as used in the *ATLAS* muon spectrometer (about 3 bar(a)). Such a drift tube is installed on top of the facility frame allowing gas quality reviews using drifttime spectra. The pressure range of the second section, following the first one, is optimized for micromegas chambers (about 10 mbar(g)). Besides the controlling of the gas properties the system also includes several temperature sensors and a barometer to monitor the conditions in the room. The whole system is coded in LabView with a clear optical user interface. All parameters set, as well as all data taken with the system are written into ASCII files. Results of measurements can thus be related offline to the conditions during the data taking. More detailed information on the topic can be found in the master thesis, that is available at the department of physics and astronomy of the University of Würzburg [40].

Some issues were recognized after the master thesis' project during long term tests of the system and were therefore not considered in the thesis. Two main subjects were identified. On the one hand the allocation of physical USB-ports to the data stream in the code can change by restarting the computer, causing errors in the program. On the other hand it showed up that the gas-flow controllers and pressure controllers did not run stable in extended runs.

The physical USB-ports are usually dynamically allocated to the device handles. When restarting the computer or replugging the cables this can change the handles. In the original program those handles were hard-coded. To avoid making regular changes in the code, selection boxes were integrated into the user interface. To find the right handles several tools can be used, like NI-Visa from National Instruments.

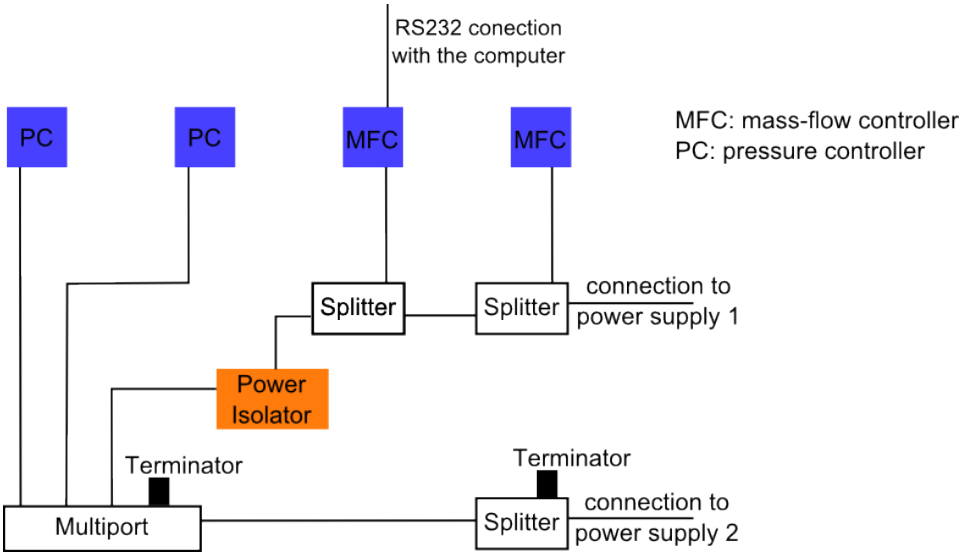

Figure 11.1.: Sketch of the bus system and power supply of the gas controllers.

In long term operation the mass-flow controllers and pressure controllers run unstable. It was found that the reason was the power supply, not providing sufficient current. Therefore a second power supply was added to the system. The bus system and power connection of the controllers, sharing the same Ethernet cables, was therefore redesigned including a power isolator to have two low voltage power supply circuits within only one data network. A sketch of the revised configuration is shown in figure 11.1. To reduce the probability of malfunctions the length of the cables between the two terminators in the system should be longer than the length of the connections between the controllers.

12. Triggering and data acquisition of the facility

A essential part of every experiment is the trigger and data acquisition system, to transfer the signals of the used detectors into analyzable data. At the facility presented here, the signals of the detectors are transformed with discriminators into logical pulses in a first step. Afterwards a trigger signal can be generated using logic units. (A table with all used electronics can be found in appendix B.) This provides a stable and quickly adoptable hardware trigger. The data acquisition itself can be done in two different ways. On the one hand a time-to-digital converter (TDC) can be used on the other hand an oscilloscope with a high time resolution is available.

12.1. Data acquisition using a time-to-digital converter

One option for the data acquisition is a multi channel TDC [41]. This TDC is a VME unit that can handle only logical signals, namely fast NIM or TTL logic signals. It was decided to use NIM pulses in the whole system. Therefore all analog signals need to be discriminated and transformed into a NIM pulse in a first step. The TDC can be addressed with a computer via a VME-controller, allowing to control and run the acquisition from the computer. The TDC can run in different modes. The basic idea of the data acquisition currently used for the test facility is shown in figure 12.1, and can be adopted if necessary.

While the TDC is ready for readout a trigger signal will open a window of interest, that can reach into the past as well as into the future. All signals at the 32 input channels of the TDC are stored during this window of interest. If the TDC is running in single event mode, a register will be set at the end of the window of interest. The data acquisition code, running on a computer, commands per-

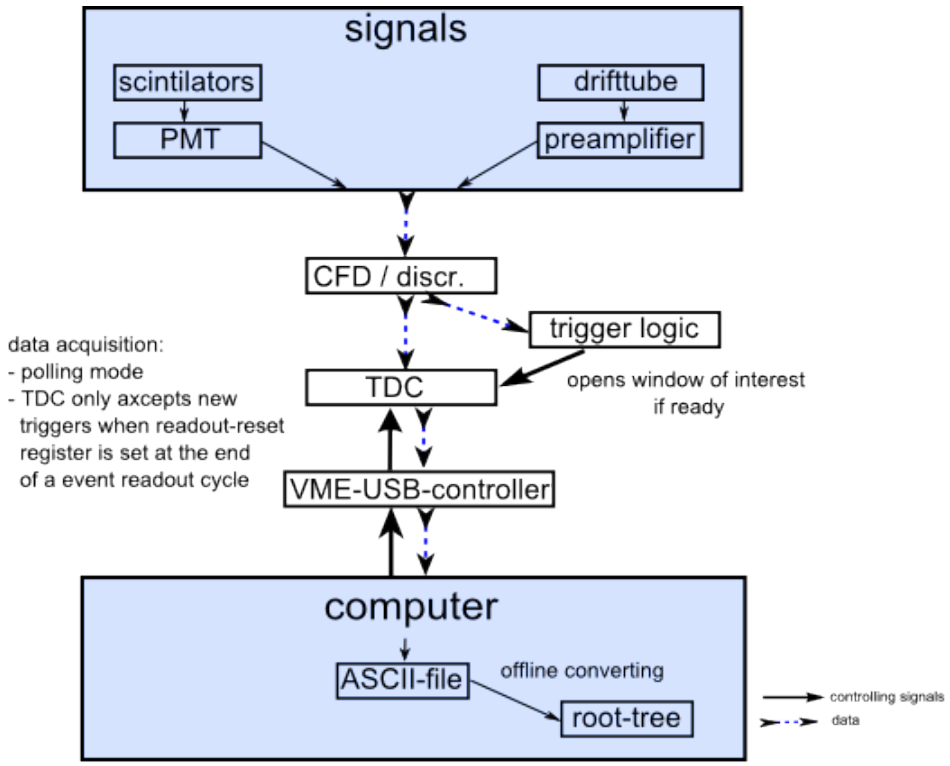

Figure 12.1.: Flow chart of the data acquisition.

manently the VME-controller to look for this register. If it is set, the data from the TDC will be read out and transferred to the computer where it will be saved. Afterwards the necessary reset registers will be set to allow new trigger signals. In the following the actual implementation of the data acquisition will be looked at more closely.

12.1.1. Implementations of the data acquisition

The TDC can be run in a lot of different configurations. For general purpose a distinct configuration was chosen and an program written to run the data acquisition and an additional ROOT script to transfer the data into a ROOT tree [42] [43]. In order to get more information on the timing characteristics of the TDC and the overall the trigger system, a second program with small differences in the configurations of the TDC was written later on (see chapter 12.1.3). The general purpose data acquisition program will be described in the following.

The communication with every unit in a VME-bus is done via a VME-controller writing into and reading from a set of registers. A data acquisition program was coded to operate the VME-controller and record the acquired data. The communication between the computer and the VME-controller is based on functions of a C-library, which were integrated in the more comprehensive data acquisition program, coded in C++ and compiled into an executable. To allow a user to customize the program to a certain extent some parameters are read in from an ASCII configuration file. An ASCII file has the advantage over arguments given to the program while calling it, that in a ASCII file the parameters can not only be change easily, but also information on the parameters and the way they have to be given can be written directly into the file. This way it is also possible to have a higher number of parameters and the operation still stays manageable. The use of the program does therefore not require further knowledge of the way it is coded.

When executing the program, the communication between the computer and the VME-controller will be established in a first step. Afterwards the TDC will be configured, before the data acquisition will start. After the data taking the communication between computer and VME-controller will be securely closed. As already mentioned before there are a lot of possible TDC configurations. In this data acquisition application the following parameter set is hardcoded:

- The two banks of the TDC, each with 16 channels, are treated as one bank with 32 channels.
- The trigger source for the TDC is input socket T0, expecting a NIM pulse.
- The TDC is running in single event mode. In this mode only one event is buffered at one time.
- All the signals inside the event window are saved.
- The events are marked with a counter, restarting each TDC powercycle.

In addition there are configurations read in from the configuration file and therefore adoptable for every data taking:

- The time in minutes the acquisition will run
- The time resolution of the TDC

- The width of the window of interest. This is the recorded time per event and the maximum is 16 µs.

- The relative time of the trigger signal within this window. This defines how far it is looked into the past and the future when a event is triggered.

After configuring the TDC, data acquisition will start running in polling mode, meaning that the computer is permanently asking if there was an event. If so the event data will be read out and written into an ASCII file. The event data consists of an even number of 32 bit words, of which the first one is the event header and the last one the end of event word, while in between every signal including the trigger of the event has its own word. If the number of words is odd a fill word will be added. Inside a word the information is given within a bit mask, but the word itself is transmitted by the VME-controller as a number of the type unsigned long. Therefore every word is converted back into a bit mask before writing it into the ASCII file, adding the unix time of the event and the event number within this data taking, which can therefore differ from the event counter within the bit mask. The file created has a name consisting of a freely selected part given within the configuration file by the user and the unix time of the start of measurement. During the measurement information will also be written to a log file. Besides the chosen parameters for the measurements, information on the communication with the VME bus and error messages concerning the writing into the files will be recorded. The naming of the log file will also include the user chosen name. A new log-file will not be created for every measurement, but when a log file with this name already exists the new information will be appended. This allows the user to create the log file before the measurement, documenting the setup. It is especially possible, to run several measurements with the same settings and only one common log file, as the naming of the data files will differ by the unix time.

Though it can be more efficient for some cases to process the ASCII file directly, a ROOT script was coded to convert the bit mask into human readable information and transferring them into a ROOT tree. The branches of this tree are:

- The number of the event within the measurement

- The unix time when the event was written

- The time resolution of the TDC during the measurement

- The ID of the TDC module, the data were taken with. The ID of the presently used TDC is 17.

- The number of signals within the event

- An object of the vector class for every channel and the trigger, containing the time in picoseconds of every signal of this channel within the event. The timing starts not with the trigger but with beginning of the event. Therefore all timing information will be positive and the trigger signal can have a positive offset.

- The number of signals within the event of every channel and the trigger channel

A proper error handling was included in the script, checking if there are all expected words and if they have the correct structure. On error occurrence, the whole event will be ignored for the conversion into a tree. In addition information on that will be written into a separate log file, in which also the number of overall events in the sample is documented. More details on such errors can be found in the next chapter.

12.1.2. Functional demonstration of the data acquisition

The measurement of the muon lifetime using the scintillation detectors and the data acquisition system of the test facility was part of a bachelor thesis [39]. While the precision of the measurement is not comparable with latest data, the measurement itself is a functional demonstration of the test facility and the data acquisition in particular.

The measurement was performed using several different detector setups and trigger logic configurations. Also first studies on setups for measuring the background rates were realized. Throughout all measurements the data acquisition was stable, except for one data taking, for which the data were corrupted. The reason for that was due to an application related misconception and is discussed in chapter 12.1.3. The resulting value for the muon lifetime is in good agreement with literature, taking into account, that background signals and systematic uncertainties were not studied in detail. Furthermore it was shown that the statistic necessary for a sufficient precision of the measured muon lifetime value can be acquired in a couple of hours. The possibility to perform the measurement within one day allows to use the facility also for future student lab courses.

12.1.3. Measurements of the TDC characteristics

The manual of the TDC does not give complete answers on all details, while other specifications even seem to be inconsistent [41]. Therefore a few short measurements were performed in order to get information on these issues as well as on the reliability of the module.

Filename	Intention	Events	Errors
GeneralSample	General understanding of the system	48 757 804	2
StampTest2	Search for overlaps	16 095 431	—
ParallelDrift	Comparison TDC and oscilloscope	111 130	—
Orthogonal-Configuration	Timing studies	16 245 915	—
MuLTMessung-MitZusDetektoren3	Muon lifetime	14 404 777	—
Overall		**95 615 057**	**2**

Table 12.1.: Errors in the structure of recorded data. During conversion of the raw data into trees errors are logged, when expected words are missing or when words have a structure differing from what is expected. The muon lifetime measurement was done as part of [39].

The reliability of the TDC is crucial for the whole data acquisition. The error handling during the conversion of the raw data into a tree allows to get an impression on the existence of errors. In table 12.1 some measurements are listed together with their number of events and the number of errors within the samples. During all measurements done until now, no other errors than missing end of event words appeared and that error appeared only two times in more than $95 \cdot 10^6$ events. But because of the small amount of errors, there is also no hint on the reason for them.

During the measurements of the muon lifetime as part of a bachelor thesis [39], some data was corrupted. The TDC was not able to open a window for the complete 16 µs as specified in the manual as maximum. Further investigations on this showed, that the window can only be 16 µs wide, when the time resolution is set to 250 ps or less. One should be aware that when a better resolution is chosen the window has to be accordingly smaller.

The TDC can also handle signals that appeared before the trigger. The information on these signals must be stored in some kind of internal memory. This raised the

question if a trigger signal will open a new event when a part of the window of interest will overlap with a part of the window of interest of the event before. A new event can only be triggered when the one before is already acquired, but its window of interest can reach into the past and by this maybe into the window of interest of the event before. A overlap like this would lead to double counting of signals. The manual of the TDC stated nothing on this topic.

To investigate in this question further, the data acquisition program was adopted to obtain a full time stamp for each event. The measurement ran for 60 hours. The windows opened for every event were starting 2.5 µs before the trigger and reaching until 2.5 µs after the trigger. Approximately 16 million events were recorded, not one overlapping with another (see table 12.1). The maximum overlap possible between two events is 2.5 µs, in case the trigger starts a new event exactly when the window of the last event ends. By this the occupied time a overlap could happen is 2.5 µs times the number of events in the sample. Knowing this time and the overall duration of the data acquisition the probability for one event overlapping with one of the others can be estimated to $1.86 \cdot 10^{-4}$. Multiplying this probability with the number of recorded events gives the number of events, expected to overlap. Those are 2998.5 events for this measurement. It is obvious that the TDC is only recording events, if they are not overlapping with the event before.[1]

12.2. Data acquisition using an oscilloscope

The data acquisition can be performed not only with the TDC but also with a digital storage oscilloscope[2]. A bandwidth of 2.5 GHz allows to resolve signals in the same range as the TDC. Using the so called "TriggerAction" option of the oscilloscope, the waveform of a channel can be written to an ASCII file. Nevertheless it should be triggered on a signal generated with the electronics also used for the TDC, as more complex logical conjunctions can not be carried out with the internal trigger options of the oscilloscope. Using the oscilloscope for the data acquisition, every triggered event will be written into a separate file, recording the full waveform and not only the time information, as it is done by using the TDC. This allows to analyze also the pattern of a signal for studies, but it also means that the amount of data is a lot higher than by using the TDC. Measuring signals in parallel with the oscilloscope and the TDC resulted in data samples, that had a file size of 75 GB in case of the oscilloscope and 35 MB in case of the TDC, representing identical

[1] The Poisson probability that such a measurement would result in 0 overlaps by chance is $exp(-2998.5)$ and therefore basically 0.

[2] DSO9254A from Agilent Technologies

signals. Though the oscilloscope gives the option to save more than 10^5 events the automatic file name suffixes have only 5 digits. By this all events after the event 10^5 will overwrite already acquired events. This limits the options for using the oscilloscope mainly to analyzing the shape of signals and short measurements with only small statistics expected.

The feasibility of acquiring data with the oscilloscope, as well as the functional capability of the installed drift tube were studied within the scope of a bachelor thesis [44]. For measuring the drift time the signal of the drift tube and a reference signal of a scintillation detector was acquired with the oscilloscope. The coincidence of both signals within a given time slot was used to generate a trigger signal for the oscilloscope. The drift-time was obtained offline from the full waveform information. The resulting drift-time spectra are fully consistent with the expectations, by this proving the functional capability of the system.

12.3. Comparison of the two data acquisition options

The signals of the detectors are discriminated with the same electronics, whether they are acquired by the TDC or the oscilloscope. The trigger signal is also generated with the same logic units. This gives the opportunity to directly compare the acquisition of both systems by using identical signals during simultaneously running acquisitions.

A drift-time spectrum was measured as it was done in a bachelor thesis [44]. Differing from the setup in the thesis the oscilloscope and the TDC were acquiring data simultaneously with identical configurations. As both acquisition options are running on different computers having independent system clocks, the exact time difference was measured by acquiring a few signals particularly generated for this reason. This identified time difference between the systems was used to synchronize the data. Figure 12.2 shows the two acquired drift-time spectra as well as their difference.

It can be noticed that the spectrum acquired with the TDC has more entries than the one acquired with the oscilloscope, while the form of the spectra seems to be nearly identical. This can be explained as the amount of data per event written out by the oscilloscope is a lot bigger than the extent of data written out by the TDC readout. In addition the data from the TDC is written to an internal hard-

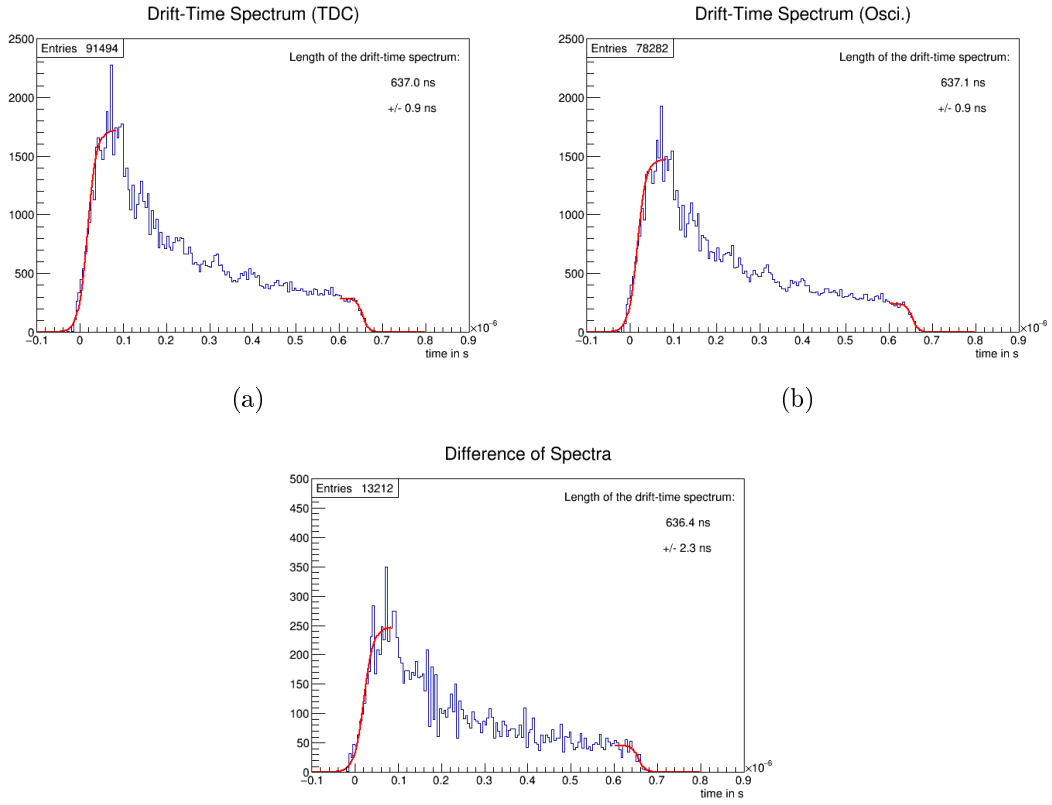

Figure 12.2.: Drift-time spectra. In the upper line the drift-time spectra acquired with the TDC and the oscilloscope are shown respectively. The histogram below presents the difference of the two. Also indicated are fits on the rising and falling edges of the distributions and the lengths of the spectra calculated from the fit parameters.

disc while the data from the oscilloscope are written to an external one using an USB-2 connection. By this, more dead time is to be expected for the oscilloscope readout. The representation of a single event measured by the oscilloscope is a ASCII file of about 1 Mb. With a theoretical transfer rate of 480 Mbit/s using a USB2 connection this results in a death time of around 2 ms just by writing out a event. To support this explanation a closer look at the distributions has to be taken.

Some of the most important parameters of the spectrum can be obtained by fitting the rising and the falling edge of the distribution. For this Fermi functions were used:

$$y(x) = \frac{a_r}{\exp(\frac{b_r - x}{c_r + 1}) + d_r} \quad ,$$

$$y(x) = \frac{a_f}{\exp(-\frac{b_f - x}{c_f + 1}) + d_f}$$

for the falling edge respectively, where a is a scale factor, b gives the inflection point, c is an indicator on the steepness of the function and d an offset. While the length of the spectrum is calculated out of the inflection points and indicated in the plots, the rest of the parameters are given in table 12.2.

	TDC	**Oscilloscope**	**Difference**
a_r	1719	1472	247
$\delta(a_r)$	± 16	± 15	± 6
a_f	287	242	45
$\delta(a_f)$	± 7	± 6	± 3
$\frac{a_r}{a_f}$	5.99	6.08	5.49
$\delta(\frac{a_r}{a_f})$	$\pm 4.1 \cdot 10^{-3}$	$\pm 4.1 \cdot 10^{-3}$	± 0.39
b_r	$16.8 \cdot 10^{-9}$	$16.2 \cdot 10^{-9}$	$19.9 \cdot 10^{-9}$
$\delta(b_r)$	$\pm 0.4 \cdot 10^{-9}$	$\pm 0.5 \cdot 10^{-9}$	$\pm 1.1 \cdot 10^{-9}$
b_f	$653.8 \cdot 10^{-9}$	$653.3 \cdot 10^{-9}$	$656.2 \cdot 10^{-9}$
$\delta(b_f)$	$\pm 0.8 \cdot 10^{-9}$	$\pm 0.8 \cdot 10^{-9}$	$\pm 2.0 \cdot 10^{-9}$
c_r	$10.6 \cdot 10^{-9}$	$10.4 \cdot 10^{-9}$	$11.3 \cdot 10^{-9}$
$\delta(c_r)$	$\pm 0.2 \cdot 10^{-9}$	$\pm 0.2 \cdot 10^{-9}$	$0.5 \pm \cdot 10^{-9}$
c_f	$7.2 \cdot 10^{-9}$	$7.0 \cdot 10^{-9}$	$7.8 \cdot 10^{-9}$
$\delta(c_f)$	$\pm 0.4 \cdot 10^{-9}$	$\pm 0.4 \cdot 10^{-9}$	$\pm 0.9 \cdot 10^{-9}$
d_r	0	0	0
$\delta(d_r)$	$\pm 5 \cdot 10^{-4}$	$\pm 4 \cdot 10^{-4}$	$\pm 2 \cdot 10^{-4}$
d_f	0.19	0.13	0.06
$\delta(d_f)$	± 0.10	± 0.08	± 0.06

Table 12.2.: Fit parameters and their uncertainties of the drift-time spectra.

The parameter b, as well as c, that both should be independent of the number of events are the same within the errors for the spectra measured with the TDC and the oscilloscope. Also the difference of both spectra has only slightly differing parameters, which could be due to the lower statistic. The ratios of the scale factors of the rising and falling edges $\frac{a_r}{a_f}$ on the other hand are not compatible within their errors, motivating further studies.

A second way to investigate dead time as source of the difference, is to look at the rates. If the missing events in the oscilloscope measurement are due to the dead time they should be distributed randomly. In figure 12.3 the events per hour are shown for the acquisition with the TDC, as well as with the oscilloscope. In addition also the difference and the difference normalized to the TDC rates are indicated.

Those distributions also support the hypothesis of the dead time induced difference, as the two acquired distributions and the difference of them show similar features and the distribution of the normalized difference is flat within the uncertainties. Another test the dead time hypothesis is also shown in figure 12.3. If the difference between oscilloscope and TDC is due to dead time, there should be an increasing difference with rising event numbers. The relative difference is therefore displayed as function of the absolute number of events recorded by the TDC. A linear fit to the data confirms the hypothesis clearly. The fit has a reduced χ^2 of 1.1, an evidently positive slope and an axial intercept that is compatible with 0.

While it can be stated that the data acquisition with the TDC and the oscilloscope is resulting in at least statistically equal data, there is still a conspicuous feature in data, regardless the system they are acquired with: The difference of the entries of one bin to the next is often much higher than expected by statistics. While artifacts from binning or transforming the raw information into human readable times are excluded, it is not known yet where this structure is coming from.

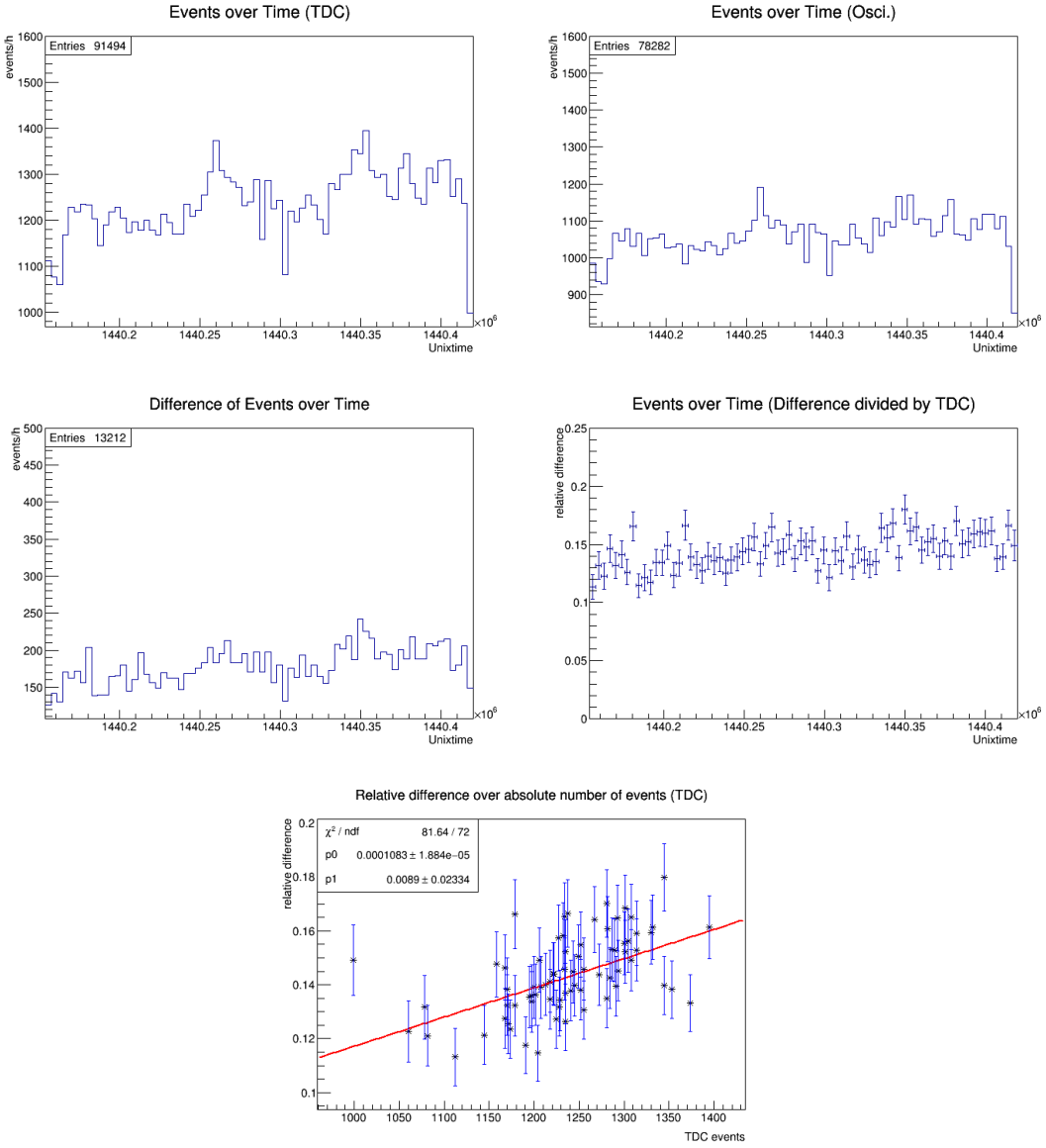

Figure 12.3.: Event rates of the drift-time spectra. In the upper line the event rates acquired with the TDC and the oscilloscope are shown respectively. The histograms below present the difference of the two as well as the difference normalized to the rates acquired with the TDC. The latter one is also indicating errors calculated by propagating Poisson errors of the difference and TDC distributions, assumed to be independent. The time is given in unix-time. The measurement started on August 21th 2015 at about quarter past 12 and lasted for about 74 hours. The relative difference as function of the absolute events of the TDC are displayed in the bottom figure and lineary fitted.

13. Timing studies of the trigger and readout system

While the principle functional capability of the trigger system including the detectors and the data acquisition has been already proven by the measurements of the muon lifetime and the drift-time spectra, only little is known so far about the actual time resolution and the response times of the detectors and electronics. For future research projects this is important to know, as a precise time measurement and a reliable reference time is needed for many questions and experimental setups. Dedicated timing measurements can be necessary depending on a specific future setup. Nevertheless a study was carried out to obtain some general insights common to most setups.

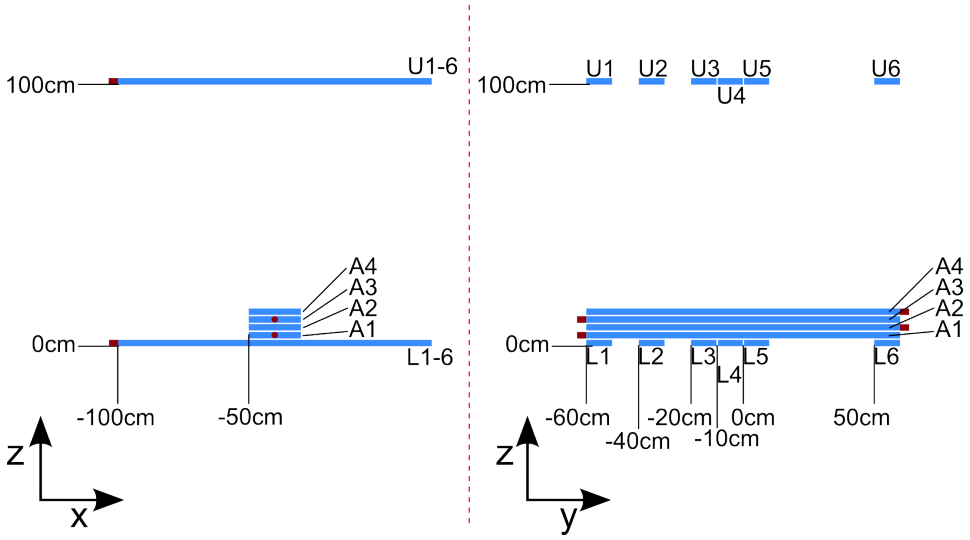

Figure 13.1.: Sketch of the configuration of the detectors for the timing study. The dark red structures represent the light guides and photomultipliers and are not to scale.

In figure 13.1 a sketch of the detector configuration is shown, which was used for this study. This configuration allows several measurements at once. The time of

flight of muons crossing the top and the bottom layer of detectors can be measured, as well as the signal time of muons crossing detectors at different distances to the photomultiplier. Finally an upper limit for the precision of a reference time obtained by the combination of signals from two stacked detectors with opposite orientation can be determined. For this study the trigger signal was generated from a logical OR of the detectors in y-orientation, while the TDC was run with a time resolution of 250 ps.

13.1. Studies on signal timing

First studies on the timing of the trigger signals were performed by using time of flight measurements. For these measurements the time difference between the signals of two detectors at the same y-position oriented in x-direction ($U1/L1$ - $U6/L6$) was taken. The distance between those detectors is 1 m, resulting in a time of flight of about 3.3 ns for a particle at the speed of light. It is expected that the measured times will be distributed around this value, not only due to the time resolution of the detectors and the readout system, but even more important due to the different time the emitted light insight the scintillator needs to reach the photomultiplier at one end of the detector with respect to the position at which the particle crosses the detector. The positions can be different for the involved detectors due to the angular distribution of cosmic muons.

Such a measured distribution is shown in figure 13.2, while the rest of them can be found in appendix B. It can be seen that the distribution is not well described by a Gaussian distribution or any other commonly used distribution. To get information on the time of flight nevertheless, a truncated mean considering 90% of the distribution is calculated. The truncated means, as well as the corresponding standard deviations are listed in table 13.1.

Several things can be seen out of these numbers as well as out of figure 13.2. The distributions are wide. The standard deviations of the truncated distributions are roughly half of the expected time of flight. This can easily be explained by the fact that for the upper detector only the y-position is determined while in x-direction the cosmic muon could cross at any position of the detector, leading to different propagation times inside the scintillator and therefore to different times of flight. The truncated means of the different detector pairs also differ. This can be explained partly with specific response times of the detectors, where no study has been performed on yet. Finally the truncated mean of all these distributions indicate a time of flight shorter than expected. In figure 13.2 a structure can be recognized at the

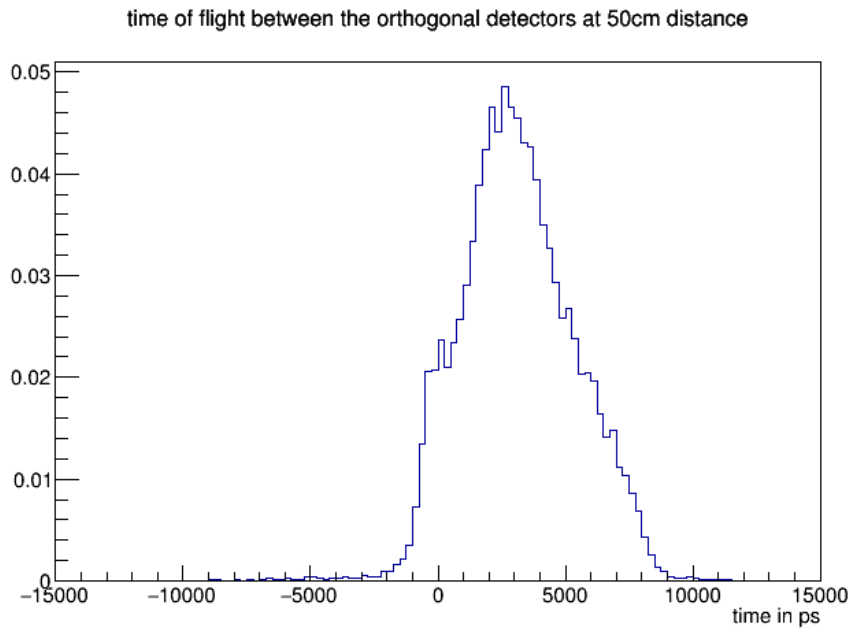

Figure 13.2.: Normalized distribution of the times of flight of the pair of detectors at 50 cm distance to the photomultiplier-side of the lowest detector with x-orientation (*U4* / *L4*).

low time flank of the distribution, that could be interpreted as a second peak. This structure can be found in all of the distributions.

In figure 13.3 the normalized signal time distributions of the two detectors used also in the distribution above are shown. The figures for the other pairs of detectors are all comparable and can be found in appendix B. The time is given relative to the mean of the signal times of the two lowest detectors with x-orientation (*A1*, *A2*). Those two detectors have their photomultiplier-end on opposite sides. By this the mean of the signal times should be a stable reference time as a long propagation time in one detector corresponds automatically to a short one in the other (see also chapter 13.3). For the shown distributions only events were chosen which have a signal in the lowest and highest detector with x-orientation (*A1*, *A4*), crossing through all of those detectors.

The distribution of the upper detector is a lot wider than the distribution of the lower one. This is expected, due to the event selection. Signals of the lower detector are only recorded, if the particles are crossing the detector in the y-range of the detectors with x-orientation (*A1*, *A4*), as those are lying directly above. But this is not true for the upper detector. Because of the distance to the detectors with

position	truncated mean [ps]	σ [ps]
0 cm	2882	1738
20 cm	3288	1725
40 cm	3157	1771
50 cm	3223	1798
60 cm	2961	1849
110 cm	2502	1718

Table 13.1.: Truncated means of the time of flight distributions. The position is given by the y-projection from the photomultplier side of the lowest detector with x-orientation (*A1*) towards the closer edge of the detector pair used for the measurement.

x-orientation the signal can be generated by a particle crossing the detector at every y-position, giving different propagation times.

The distribution of the upper detector shows on the high time side a second peak. This structure corresponds to the structure seen in the time of flight distribution and seems to be the reason for the too short time of flight. Although it is not finally understood yet, where this structure is coming from, the fact that this second peak is at the high time side of the distribution gives a first hint. The signal time is later, when the propagation time in the scintillator is longer.The peak is most probably resulting from particles crossing close to the end of the detector opposite to the photomultiplier, also explaining why it is not seen in the distribution of the lower detector. The light radiated along the direction opposite to the photomultiplier will be reflected towards the photomultiplier at the end of the detector. For a source close to the end the propagation time difference between the light radiated into photomultiplier direction and light radiated the opposite direction will not be very big. Overlapping of both parts could change the light intensity distribution arriving at the photomultiplier and therefore the electrical signal that will be discriminated. Further studies on this topic could be interesting.

13.2. Light propagation speed inside the detectors

The detector configuration used for these timing studies allows to measure the velocity of propagation of the light inside the scintillators. For this purpose the arrival time of a signal from a detector with y-orientation (*A1* - *A4*) is measured for different y-positions at which a muon is crossing. The information on this y-position is acquired by selecting only events where at both detectors with x-orientation

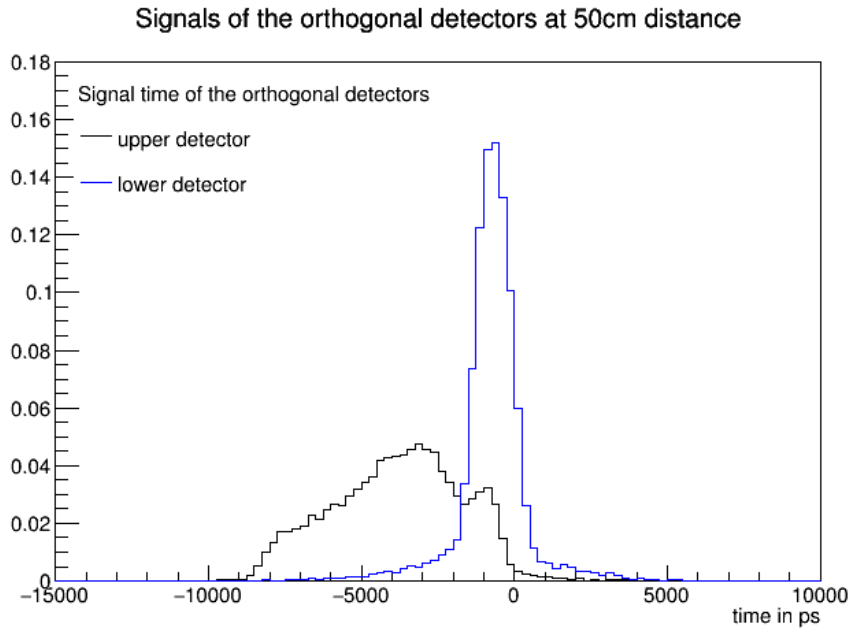

Figure 13.3.: Normalized distributions of the signal times of the pair of detectors (*U4/L4*) at 50 cm distance to the photomultiplier-side of the lowest detector with x-orientation (*A1*). The time is relative to the mean of the signals of the two lowest detectors with x-orientation (*A1*, *A2*).

(*U1/L1* - *U6/L6*) at a given y-position a signal is present. It can be stated that the muon was crossing vertically and therefore it was crossing the y-oriented detector at that position. In addition to this selection a reliable reference signal is also needed as the trigger time is given by the detectors with y-orientation (*A1* - *A4*), whose timing is studied. The signals of the lower detectors with x-orientation (*L1* - *L6*) at the corresponding y-position are taken as reference signals. The arrival time of the signals produced by particles crossing the detectors at different positions along their length are shown in figure 13.4. It can be seen that the time of a signal is depending on the distance of the spot a particle crosses the detector and the photomultiplier. Out of this information the propagation velocity of the light inside the scintillator can be determined.

For calculating this velocity a single time for each peak needs to be identified at first. As the peaks are not Gaussian-like, once more truncated means, including 90% of the data, are taken to represent the peaks. A table of the truncated means and the standard deviations of the truncated distributions of the peaks can be found in appendix B. In figure 13.5 those times are plotted as a function of the distance as well as a linear function fitted to them. For those fits the errors from the truncated means are taken as uncertainty on the time, while for the distance

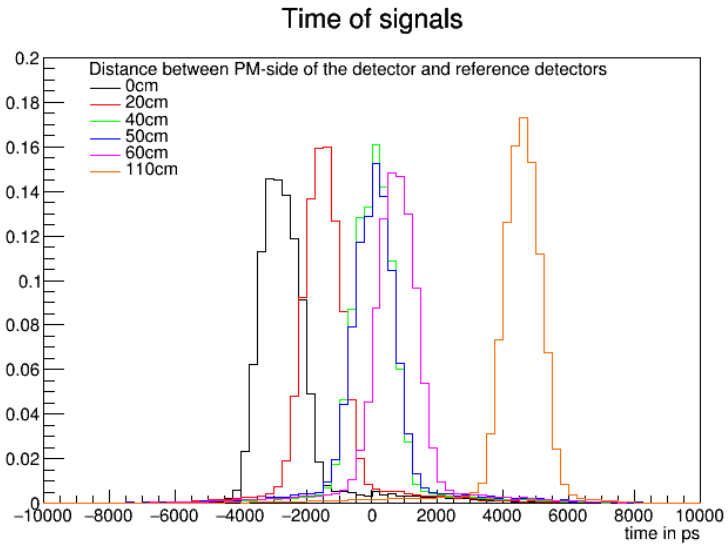

(a)

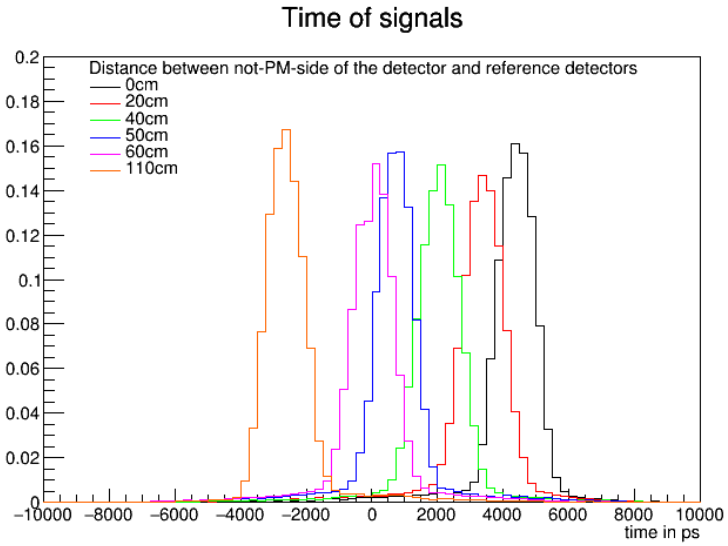

(b)

Figure 13.4.: Time of signals caused by particles crossing at different distances in y-direction to one end of the detector. In (a) the signals of the lowest detector with y-orientation (*A1*) are shown. The distances are given with respect to the end of the scintillator of this detector, where the photomultiplier is mounted. (b) illustrates the signals of the detector directly on top of the one in (a) (*A2*). The photomultiplier is opposite to the one of the detector below. Nevertheless the distances are measured towards the same side.

an uncertainty of 2 mm is assumed. This uncertainty on the positions includes on the one hand the uncertainties of the positioning of all involved detectors and on the other hand also the uncertainty due to the wrapping material of the detectors, as by different thicknesses of the wrapping the position of the sensitive scintillator material can only be determined up to a certain degree.

The fitting results for the propagation velocity are $(1.522 \pm 0.004) \cdot 10^8 \frac{\mathrm{m}}{\mathrm{s}}$ and $(1.503 \pm 0.004) \cdot 10^8 \frac{\mathrm{m}}{\mathrm{s}}$, respectively, taking only the statistical uncertainties into account. Obviously the statistical uncertainties are too small to represent the spread of the data points sufficiently. But there are also systematic uncertainties not taken into account, as for example different response times of the photomultipliers. A hint that such uncertainties give a relevant contribution is, that in both detectors, the velocity was measured with, the data points for a given position diverge from the fitted line in the same direction. A subtraction of one of the distributions from the other should eliminate most of the common systematic uncertainties. The resulting distribution is shown in figure 13.6. As expected, the data points correspond a lot better with the fit. In result a propagation velocity of $(1.532 \pm 0.004) \cdot 10^8 \frac{\mathrm{m}}{\mathrm{s}}$ is obtained, once more only taking the statistical uncertainties in account. The obvious amount of systematic uncertainties demonstrates the necessity of further studies on it, quantifying the different response times of the photomultipliers, for example.

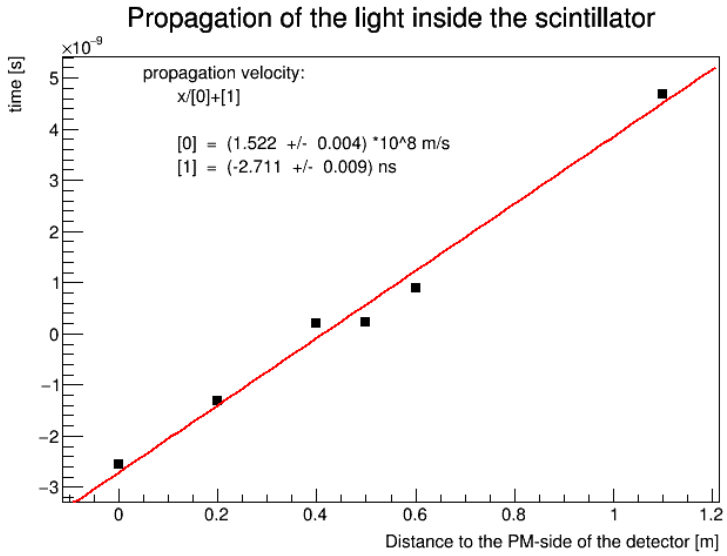

(a)

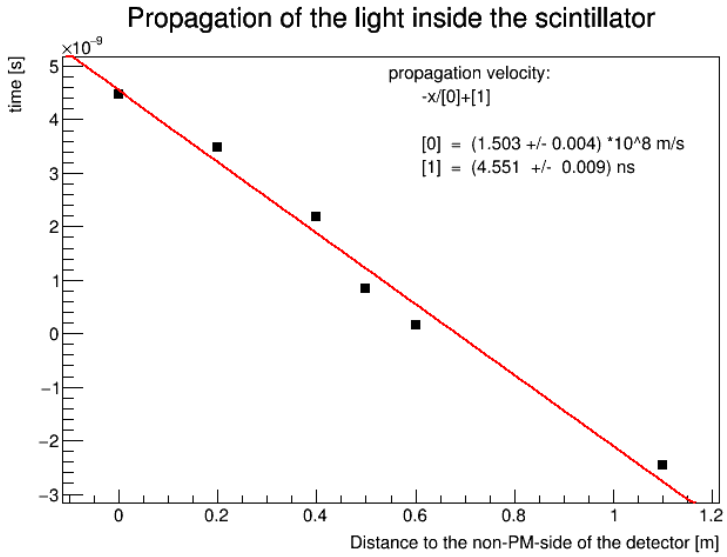

(b)

Figure 13.5.: Fitted propagation velocity of light inside the scintillators. (a) and (b) correspond to (a) and (b) in figure 13.4.

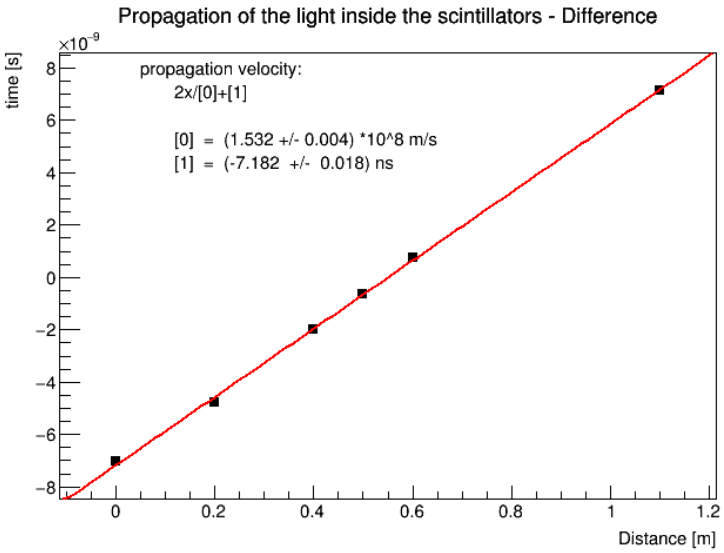

Figure 13.6.: Fitted propagation velocity out of the difference of the distributions of figure 13.5.

13.3. Precision of a time reference signal

Whenever the time of a signal has to be measured a known time reference inside the same event is necessary. The uncertainty of such a reference signal is therefore an important value to identify. In chapter 13.2 the propagation velocity of the light inside the scintillators were measured to be roughly half of the speed of light in vacuum. Therefore the time of a single detector signal will be shifted with respect to the position at which a particle has crossed the detector and is therefore not a suitable reference signal, in general. One way to minimize such signal shifts and to cover a given region with a few detectors, is to use the averaged signal of two detectors stacked on top of each other and having the photomultipliers on opposite sides. With this configuration a long distance between the crossing of the particle and the photomultiplier in one detector corresponds to a short distance in the second. Because of this geometrical fact the averaged signal should be self-stabilizing. In the following it will be studied how big the uncertainties on such a reference signal are.

The uncertainty on the reference signal consists of two independent components. One is the intrinsic distribution of the signal, having a certain width. The other one is due to geometric reasons. The average of the signals compensate different propagation times in case of vertically crossing particles, but in case of diagonally crossing particles the effect of propagation time will not cancel out but sum up.

To get information on the width of the distributions, vertically crossing particles at the y-positions of the detectors with x-orientation (*U1/L1-U6/L6*) are selected and the averaged signal of the two lowest detectors with y-orientation (*A1*,*A2*) are calculated with respect to the signal of the lower corresponding detector with x-orientation (*L1-L6*), similar to what was done for determining the propagation velocity in chapter 13.2. Unlike then, the distributions should all be centered at the same time now, due to the averaging of the two detectors. The distributions are shown in figure 13.7. It can be seen that all of the distributions look alike. They have a comparable width and are centered at the same time, except the distributions of signals caused by particles crossing at 50 cm and 60 cm distance in y-direction to the lower photomultiplier. In the measurement of the propagation velocity it was already seen that those two points were the only ones below the curve fitted to the data. This difference is thus caused very likely by a different response time of the photomultipliers of the detectors used at this distances (*L4*, *L5*). Nevertheless these shifts should be included in the uncertainty of the reference signal, as there is no data available on the response times of the photomultipliers yet, that would enable a recalibration in time of single detectors. Therefore all of the

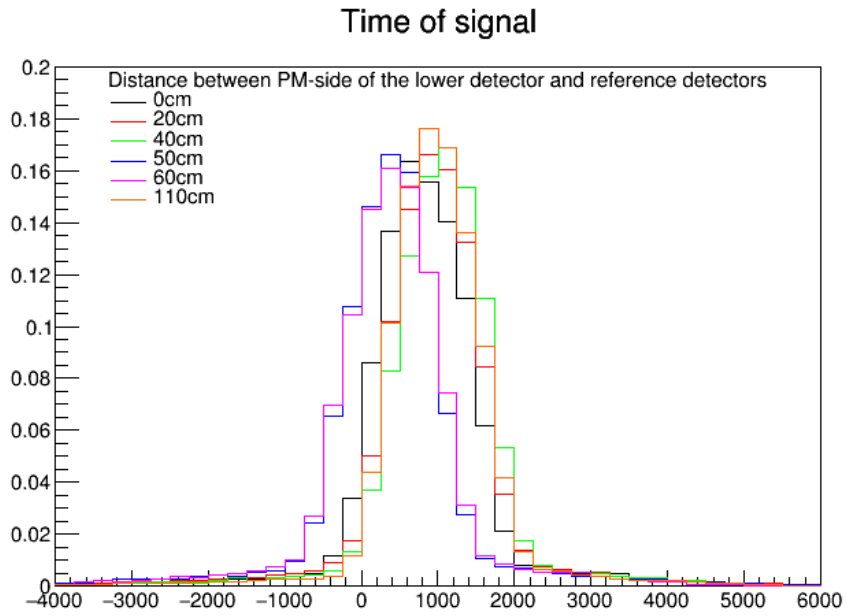

Figure 13.7.: Normalized distributions of reference signals. The time difference is given with respect to the corresponding lower detector with x-orientation (*L1-L6*).

measured distributions are summed up into one common distribution describing the reference signals. In figure 13.7 it can be seen that the single distributions are not Gaussian, but seem to have larger contributions from the tails in both directions. To characterize the differences to a Gaussian distribution the bins including 68% of the summed up distribution were identified. In case of a Gaussian distribution this is commonly known as the one-σ region. Caused by the bin width the 'one-σ region' is overestimated by taking whole bins. For this distribution the bins enclosing the 'one-σ region' include nearly 74% of the distribution. Looking at the multiples of this 'one-σ region' gives an impression, how Gaussian-like the distribution is. In the 'two-σ region' calculated from the overestimated 'one-σ region' are 92% of the distribution and in the 'three-σ region' almost 95%. This is significantly less than for a Gaussian distribution where the usual two-σ and three-σ regions include 95.5% and 99.7% of the data respectively. This shows also in numbers, that the distribution has bigger contributions from the tails than a Gaussian distribution. Nevertheless those tails include only a small amount of the entries and it seems reasonable to characterize the distribution by the width of its center. As shown in figure 13.8 a Gaussian function was fitted to the center of the distribution. The χ^2 of the fit is 55.8 with 5 degrees of freedom, showing that also for the center a Gaussian function is not describing the distribution perfectly. Also the mean

of the fitted Gaussian is slightly shifted with respect to a truncated mean of the distribution. Nevertheless a Gaussian function gives a reasonable estimation on the width of the center of the distribution. The standard deviation of this Gaussian is (610.6 ± 2.4) ps.

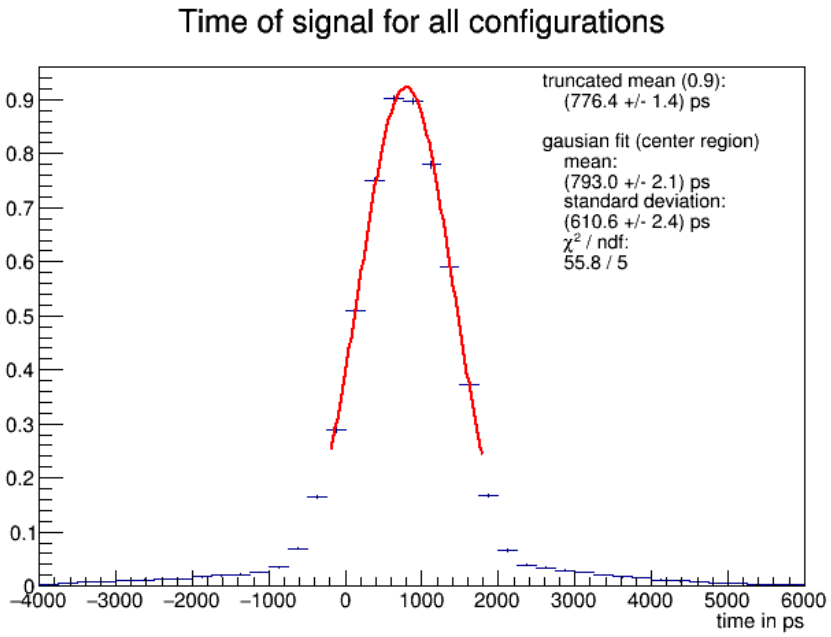

Figure 13.8.: Sum of the normalized distributions of reference signals. A Gaussian fit to the center of the distribution is also indicated.

The uncertainty due to geometrical reasons is estimated by identifying the time shift between a reference signal caused by a vertically crossing particle and a diagonally crossing particle. Again, the reference time is the averaged time of the signals of the two lowest detectors in y-direction (*A1*, *A2*) with respect to the signal of the lower detector with x-orientation and no distance in y-direction to the photomultiplier side of the lowest detector in y-direction (*L1*). Vertically crossing particles are selected by cutting on events with signals in the lower and the upper detector with x-orientation at 0 cm distance in y (*U1*, *L1*). Diagonally crossing particles are selected by cutting on events with signals in the lower detector with x-orientation at 0 cm distance in y (*L1*) and the upper one at 110 cm distance (*U6*). This results in particles crossing under an angle of approximately 47°. The distributions are shown in figure 13.9. The distribution caused by diagonally crossing particles is shifted to earlier times with respect to the distribution caused by vertically crossing particles. This is expected as the tilt results in a shorter distance to the photomultiplier in both detectors. For both distributions the truncated means were calculated. They are (957.9 ± 2.9) ps for the distribution of vertical crossings and (585.0 ± 11.8) ps for

the distribution of diagonal crossings. This results in a time shift of (372.9±12.2) ps between the two distributions.

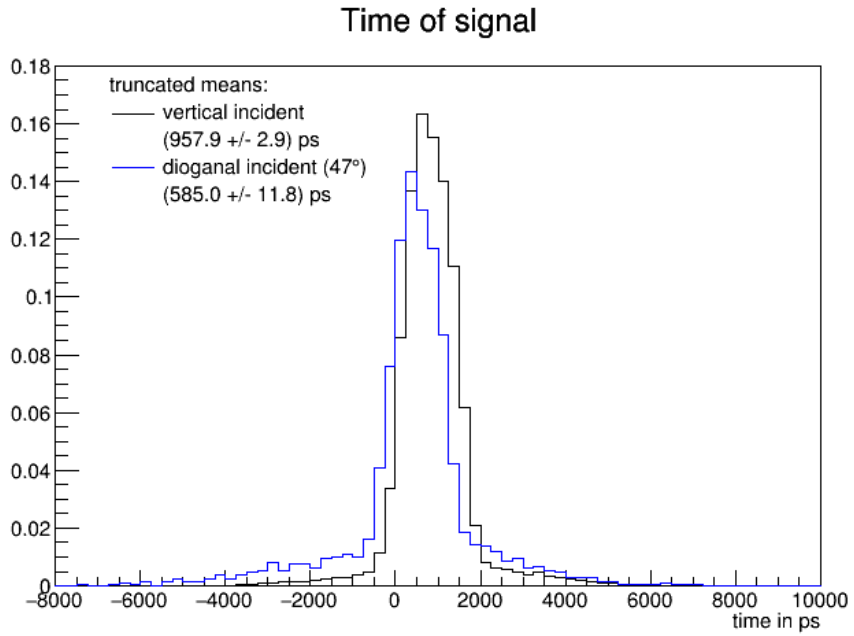

Figure 13.9.: Normalized distributions of reference signals for vertical and diagonal crossing particles. The time difference is given with respect to the lower detector with x-orientation and no distance to the photomultiplier side of the lowest detector with y-orientation (*L1*).

The two uncertainties are statistically independent and therefore sum up to 715.0 ps. Not included in this uncertainty are time shifts due to different electronic run times which can appear in complicated logical circuits for trigger and data acquisition reasons. In addition the non-Gaussian tails should also be kept in mind. Nevertheless even for configurations with big angles and complicated electronic circuits, it can be stated that the uncertainty on a reference signal, generated by averaging the signal times of two detectors lying directly on top of each other and having their photomultipliers on opposite sides, is less than a nanosecond.

14. Conclusion on the construction of the test facility

A test facility for gaseous detectors was designed and constructed at the University of Würzburg. The functional capability of the facility was proven and first studies on the timing of the triggering components were performed.

The test facility was designed in a flexible way for enabling many different future studies and it is big enough to handle the *ATLAS New Small Wheel* detector parts, the University of Würzburg will participate in building. Besides mechanical support structures, the facility consists of a gas supply system with two different pressure sections, a drift tube used for gas studies, a trigger system, as well as two different data acquisition systems. While one data acquisition system is an oscilloscope, the other system is based on a TDC within a VME environment. Programs were coded to control the measurement with the TDC and to handle the data afterwards. The trigger system is built of scintillation detectors, electronics for discriminating the signals and logic operations. A metal absorber in the frame of the facility allows also the discrimination between high and low momentum muons. 30 scintillation detectors were mounted providing a high flexibility in the setup design by their number.

The functional capability was proven already in the early test phase, among other studies, by performing also bachelor theses with the facility, measuring drift-time spectra with the drift tube as well as the muon lifetime with the trigger detectors. Thereby it is also demonstrated that the facility is suitable for teaching aspects. The possibility to use the facility for a permanent "muon lifetime experiment" as part of lab courses is being discussed.

In a first study it was demonstrated, that the data acquisition using the TDC or an oscilloscope respectively, are statistically equivalent. Nevertheless differences were seen. While the oscilloscope offers the opportunity to investigate the form of the

signal pulses, the TDC is only handling time information. But this advantage of the oscilloscope comes with a price. First of all the oscilloscope can only store up to 10^5 events per run, occupying already a lot of disc space with this relative small sample. In addition the efficiency of the oscilloscope is worse than the efficiency of the TDC. This is most probably due to a higher dead-time during writing the data to an external hard drive. Finally the oscilloscope is a standalone system and can not be integrated into the overall control system of the facility, therefore a manual synchronization is necessary whenever the oscilloscope is part of a bigger setup.

In studies on the timing of the trigger system the light propagation velocity in the scintillator material was measured with $1.532 \cdot 10^8 \frac{\mathrm{m}}{\mathrm{s}}$, having a statistical uncertainty of $0.004 \cdot 10^8 \frac{\mathrm{m}}{\mathrm{s}}$, while systematical uncertainties were not studied in detail. Furthermore some time of flight measurements were performed, resulting in too short times measured and showing interesting structures in the distributions. Such structures indicate that particles crossing at the photomultiplier distant end of the detector cause a different signal than those crossing somewhere else. This could be a hint, that a superposition of the light emitted directly towards the photomultiplier and the one emitted oppositely and being reflected is the reason for the too short times measured. Further studies on this could be an interesting topic for a future master thesis. Finally the uncertainty on a reference signal generated by averaging the times of the signals of two stacked detectors with their photomultipliers on opposite sides were measured. This uncertainty was identified with 715.0 ps. All of these measurements showed hints for varying response times of the detectors. Further studies on that issue could be performed for increasing timing accuracy.

Summary

This work consist of two independent parts, contributing both differently to the common goal of further development of particle detectors.

In the first part of the thesis detailed background simulation studies on the shielding of the planned *New Small Wheel* as part of the *ATLAS* detector upgrade are discussed. Results were communicated within the *ATLAS NSW* community, supporting the discussion on the *New Small Wheel* design. Besides the results reflected in the final design of the *New Small Wheel* shielding, it was also shown that further studies and engineering efforts on the mounting gaps in the cladding of the *Hub* part of the shielding should be undertaken.

In the second part of the thesis the design and the establishment of a local test facility for gaseous detectors at the University of Würzburg is presented. This facility opens up the possibility to contribute to the testing and further development of the *Micromegas* chambers of the *ATLAS New Small Wheel* upgrade project. Furthermore the facility is also built flexible enough to be used, without fundamental adaptions, for any kind of future research intention on that field, within *ATLAS* collaboration projects as well as within independent developments or studies of the University of Würzburg.

Several bachelor theses were carried out on the facility, already during the construction phase as well as during the verification of the functional demonstration. This shows that the facility can be operated also with little experience and therefore is appropriate for teaching purposes. In this way the facility is not only a benefit for detector development at the University of Würzburg but also for teaching purposes.

Appendices

A. Simulations Studies

Scoring volumes

name	r_{min} [cm]	r_{max} [cm]	z_{min} [cm]	z_{max} [cm]	tilt angle [°]
EI region					
EI CSC	93.1	210.9	750.0	760.0	-11.59
EI CSC	93.1	210.9	-760.0	-750.0	11.59
EI MDT-1	211.1	453.7	750.0	760.0	0
EI MDT-1	211.1	453.7	-760.0	-750.0	0
EI MDT-2	453.8	660.0	762.5	772.5	0
EI MDT-2	453.8	660.0	-772.5	-762.5	0
BI region					
BIS	465.0	475.0	-685.0	685.0	0
BIS8	457.0	467.0	685.1	729.9	0
BIS8	457.0	467.0	-729.9	-685.1	0

Table A.1.: Definition of the scoring volumes. The scoring volumes are the representations of the detectors for the simulations. All distances are given in respect to the interaction point.

General scenario - hit rates

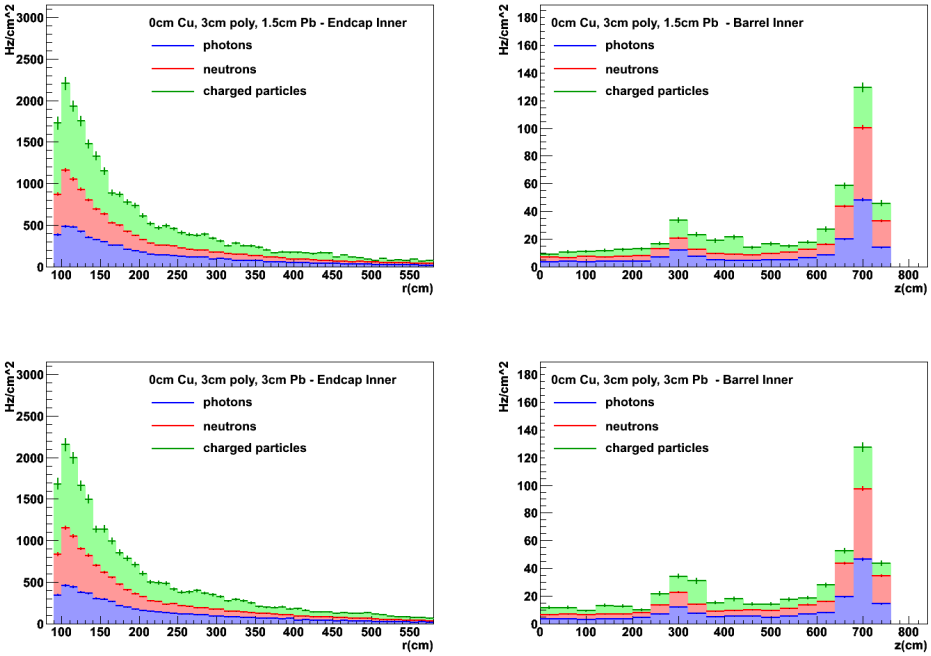

Figure A.1.: Hit rate distributions of adapted geometries. On the left hand side the rates in the EI region are displayed, on the right hand side the rates in the BI region can be seen. Presented are shielding compositions without a copper layer and a 3 cm thick layer of polyboron.

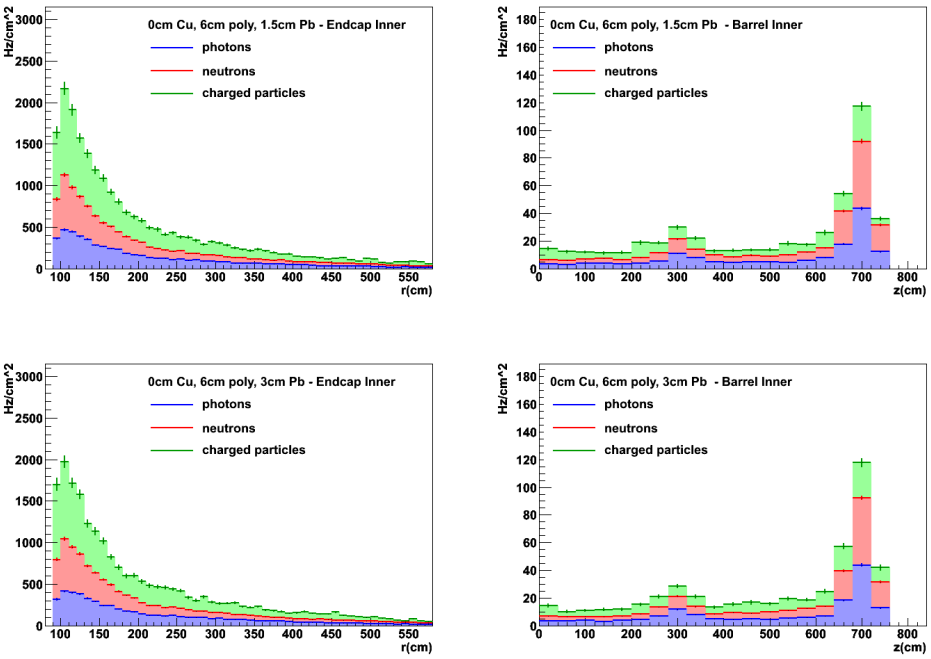

Figure A.2.: Hit rate distributions of adapted geometries. On the left hand side the rates in the EI region are displayedn, on the right hand side the rates in the BI region can be seen. Presented are shielding compositions without a copper layer and a 6 cm thick layer of polyboron.

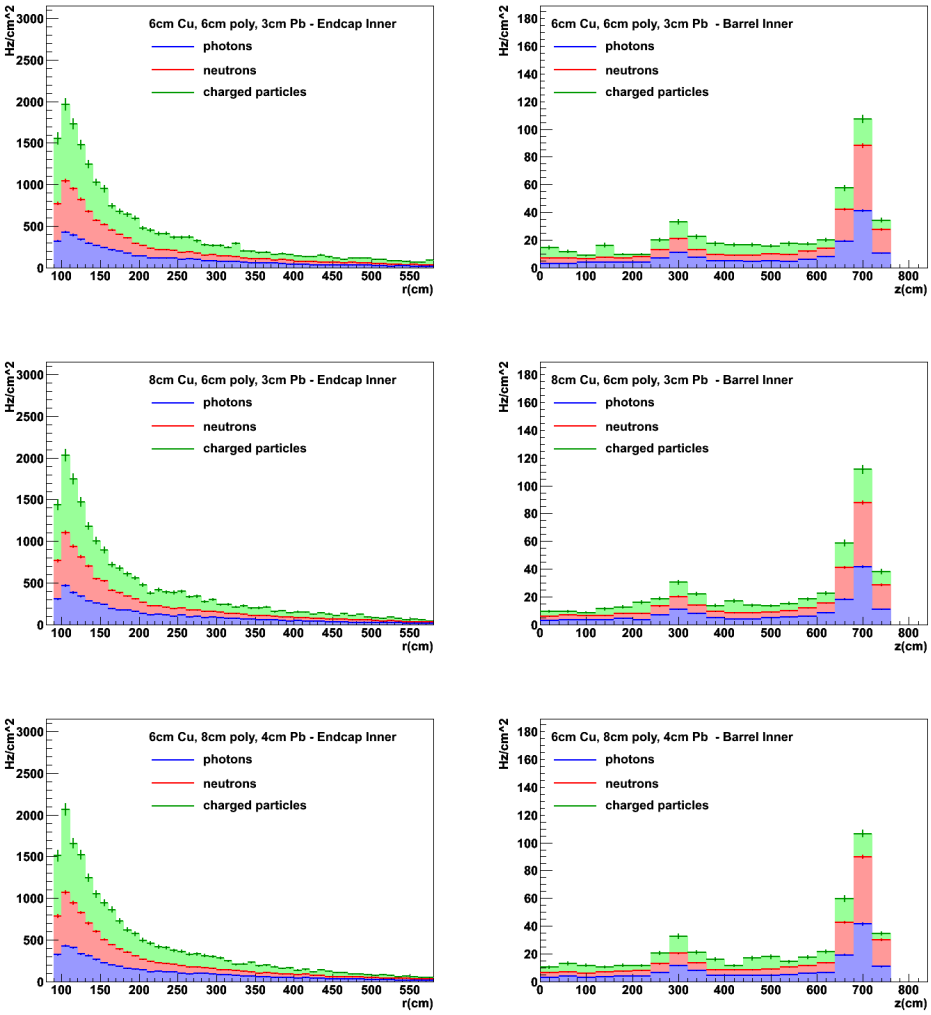

Figure A.3.: Hit rate distributionss of adapted geometries. On the left hand side the rates in the EI region are displayed, on the right hand side the rates in the BI region can be seen. Different shielding compositions with a copper layer are presented.

General scenario - hit rates with extended shielding

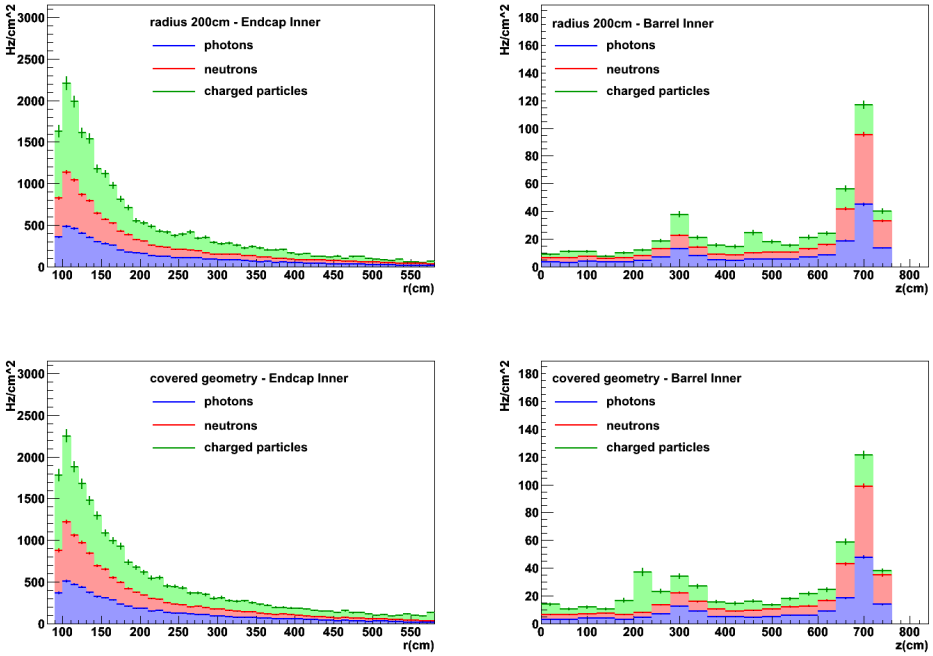

Figure A.4.: Hit rate distributions of adapted geometries with extended radius. On the left hand side the rates in the EI region are displayed, on the right hand side the rates in the BI region can be seen. In the upper row the rates for a "Cone shielding with an outer radius of 200 cm are presented. In the lower row the "Cone" shielding has a lead cover at the outer radius.

Restricted scenario - energy distributions

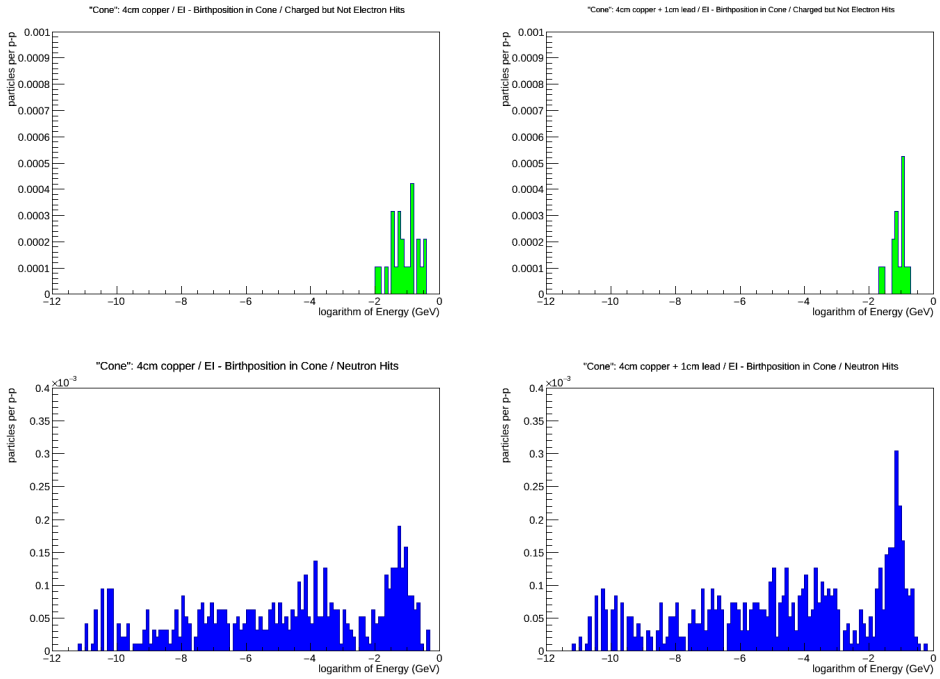

Figure A.5.: Energy distributions of shielding compositions including a copper layer. On the left the distributions of a shielding out of 4 cm of copper are displayed, while on the right the distributions of a shielding composed of 4 cm copper and 1 cm are presented. On the top the distributions of the charged particles without electrons and on the bottom the distributions of the neutrons are shown.

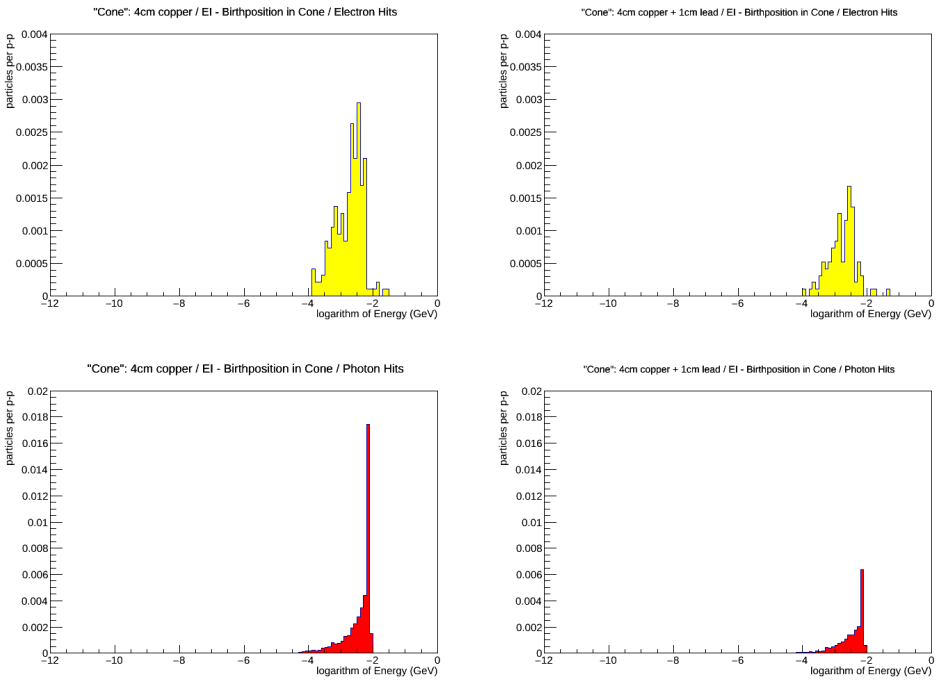

Figure A.6.: Energy distributions of shielding compositions including a copper layer. On the left the distributions of a shielding out of 4 cm of copper are displayed, while on the right the distributions of a shielding composed of 4 cm copper and 1 cm are presented. On the top the distributions of the electrons and on the bottom the distributions of the photons are shown.

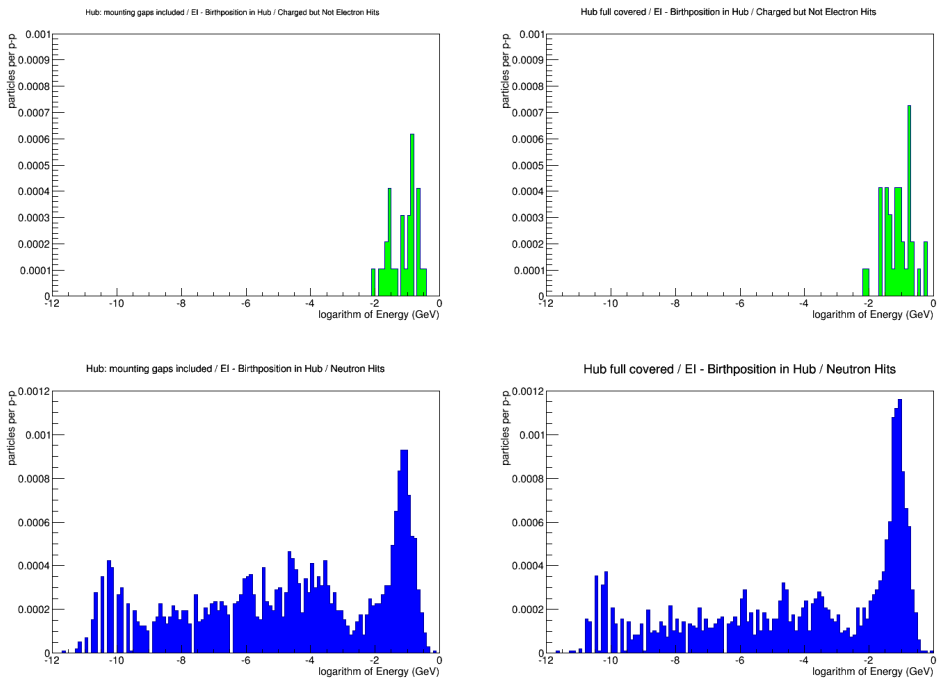

Figure A.7.: Energy distributions from particles with a birthposition in the Hub-region. The left column displays the energy distribution for a Hub with cladding gaps, the right one the distribution for a continuously covered Hub. The upper row presents charged particles without electrons, while the lower row gives the results for neutrons.

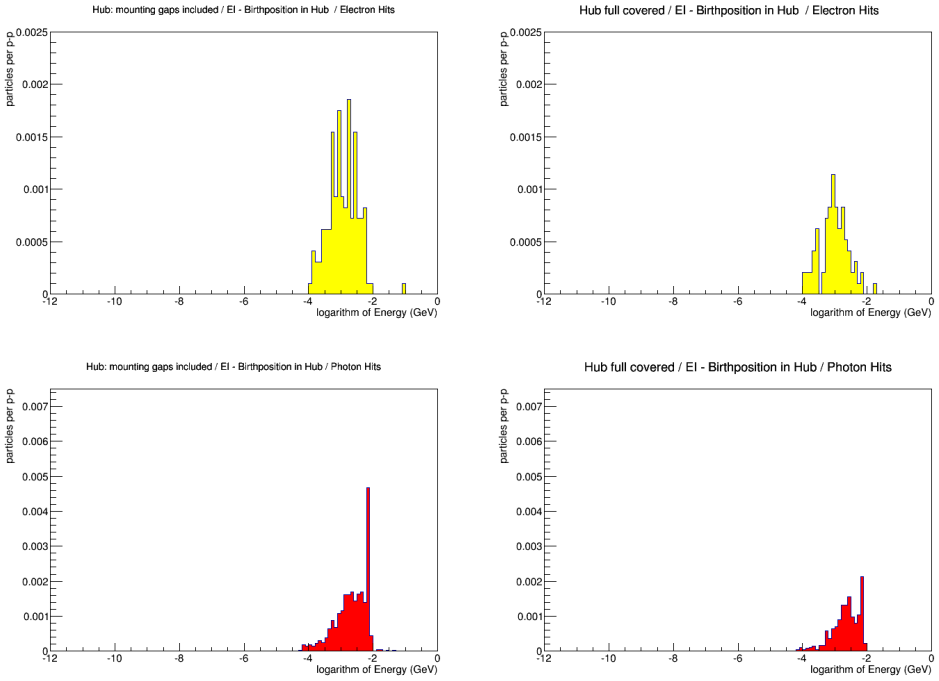

Figure A.8.: Energy distributions from particles with a birthposition in the Hub-region. The left column presents the energy distribution for a Hub with cladding gaps, the right one the distribution for a continuously covered Hub. The upper row displays electrons, while the lower row gives the results for photons.

B. Test Facility

Trigger detectors

detector ID	PMT ID	operating voltage [V]	efficiency	specific features
100-01	LA4611	1100	0.989	
100-02	LA4638	1150	0.980	
100-03	LA4612	1150	0.979	
100-04	LA4641	1250	0.984	
100-05	LA4643	1150	0.984	
100-06	LA4550	1100	0.986	
100-07	LA4650	1100	0.990	
100-08	LA4608	1150	0.983	
100-09	LA4646	1100	0.991	small breakout in the scintillator material; area polished
100-10	LA4604	1250	0.983	
100-11	LA4640	1150	0.982	
100-12	LA4609	1150	0.984	
100-13	LA4544	1150	0.989	breakout in the scintillator material (at the connection to the PMT); broken off corner of scintillation material (opposite the connection to the PMT); areas polished
100-14	LA4545	1200	0.989	small breakout in the scintillator material; area polished
200-01	LA4605	1400	0.986	
200-02	LA4645	1250	0.962	

200-03	LA4606	1350	0.957	
200-04	LA4546	1250	0.989	
200-05	LA4644	1450	0.937	
200-06	LA4551	1250	0.992	
200-07	LA4543	1250	0.990	bonding broken; repaired after efficiency measurement
200-08	LA4549	1250	0.955	
200-09	LA4607	1250	0.990	broken off corner of scintillation material (at the connection to the PMT); area polished before gluing
200-10	LA4601	1300	0.971	
200-11	LA4648	1250	0.957	
200-12	LA4547	1150	0.985	
200-13	LA4560	1300	0.939	
200-14	LA4553	1150	0.972	
700-01	LA4639	1450	0.993	
700-02	LA4642	1550	0.962	bonding broken (twice); efficiency measurement between the two incidents

Table B.1.: List of the trigger detector characteristics. The operating voltages and the efficiencies were identified in [39]. The detector ID contains also a reference to the detectors dimension, as the number before the hyphen indicates the width in millimeter.

Electronics of the trigger and data acquisition system

All electronics and supply units of the trigger and data acquisition of the test facility used during the work for this thesis are listed below:

- CAEN - Universal Multichannel Power Supply System [45]:
  - CAEN - 24 Channel Negative 3.5 kV / 3 mA - Mod. A1535SN [46]
  - CAEN - 12 Channel Negative 3.5 kV / 3 mA - Mod. A1535D [47]
  - CAEN - 12 Channel Negative / 12 Channel Positive 3.5 kV / 3 mA - A1535SM [46]
- WIENER, Plein & Baus Elektronik - NIM Crate Power Supply - UEP10M88 [48]
- NIM modules:
  - Fakultät für Physik LMU - 8 Channel Threshold Discriminator
  - CAEN - 16 Channel Constant Fraction Discriminator - Mod N843 (2 pcs.) [49]
  - CAEN - Dual Timer - Mod N93B [50]
  - Phillips Scientific - Octal Multifuntion Logic Unit - Mod. 757 (3 pcs.) [51]
- WIENER, Plein & Baus Elektronik - VME Minicrate 395 [52]
- VME modules:
  - WIENER, Plein & Baus Elektronik - VME Controller - VM-USB [53]
  - mesytec - 32+2 Channel Time Digitizer - MTDC-32 [41]
- Agilent Technologies - Digital Oscilloscope - DSO9254A

Time of flight measurements

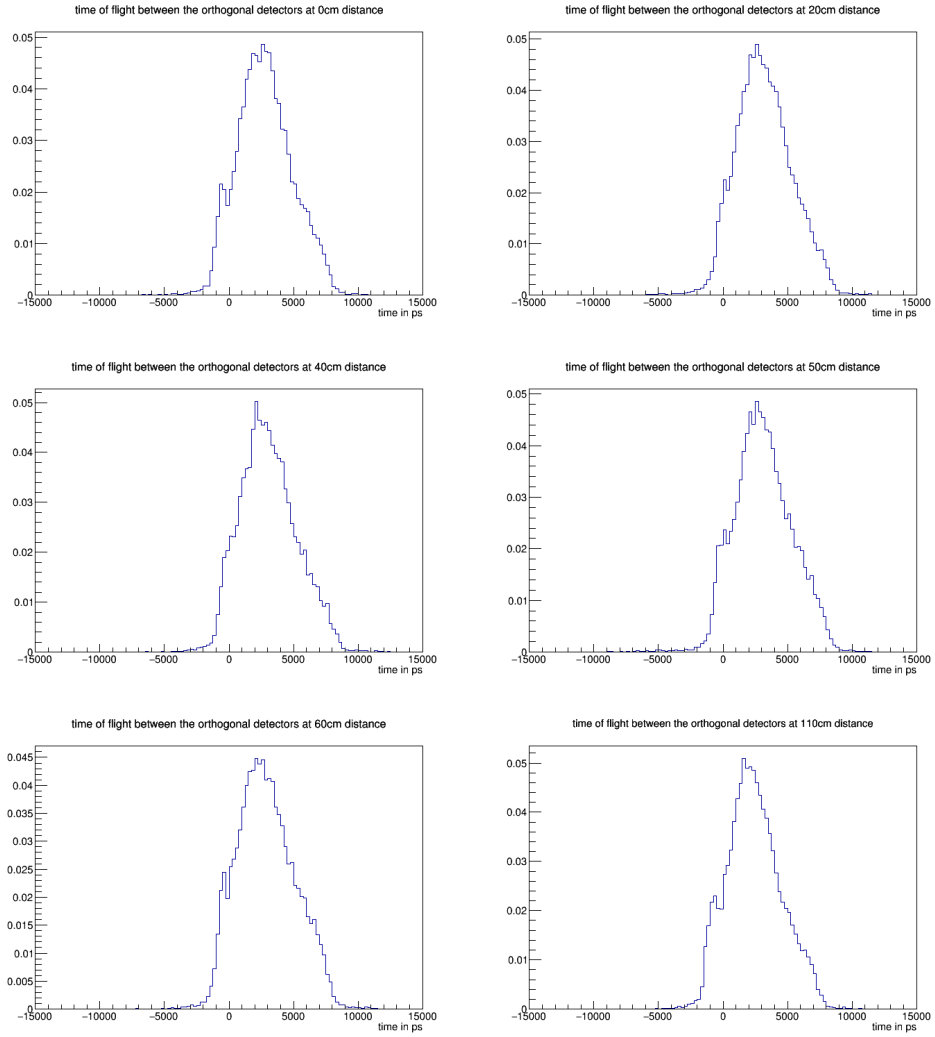

Figure B.1.: Normalized distributions of the times of flight of the pairs of detectors at 0 cm, 20 cm, 40 cm, 50 cm, 60 cm and 110 cm distance to the photomultiplier-side of the lowest detector with x-orientation.

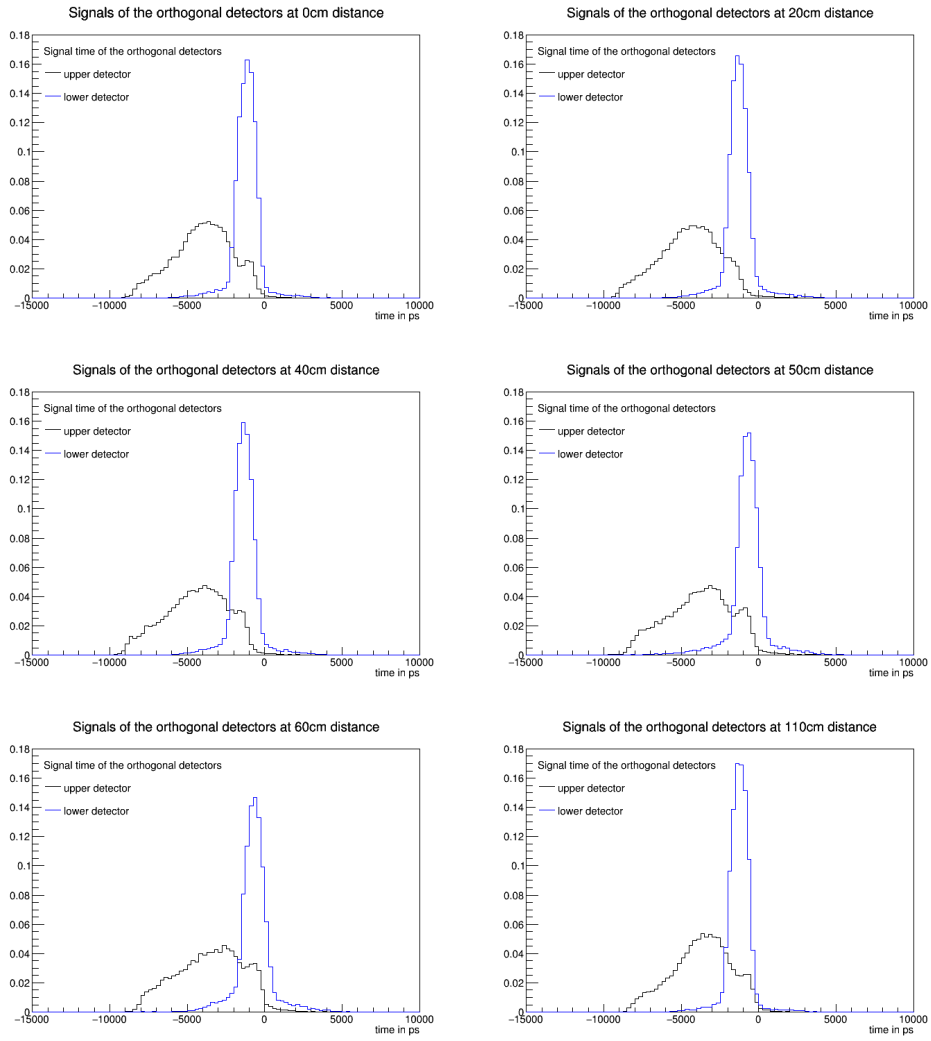

Figure B.2.: Normalized distributions of the signal times of the pairs of detectors at different distances to the photomultiplier-side of the lowest detector with x-orientation. The time is relative to the mean of the signals of the two lowest detectors with x-orientation.

Light propagation velocity

	detector A1 (PMT at 0 cm)		detector A2 (PMT opposite 0 cm)	
position [cm]	**mean [ps]**	**σ [ps]**	**mean [ps]**	**σ [ps]**
0	-2562 ± 4	616 ± 3	4480 ± 3	513 ± 2
20	-1319 ± 3	552 ± 2	3471 ± 3	589 ± 2
40	198 ± 3	517 ± 2	2176 ± 4	550 ± 2
50	225 ± 4	579 ± 3	847 ± 3	533 ± 2
60	892 ± 4	557 ± 2	159 ± 4	562 ± 3
110	4689 ± 3	465 ± 2	-2468 ± 3	490 ± 2

Table B.2.: Characteristics of truncated distributions for different positions a particle crosses the detector. In the truncated distributions 90% of the entries were taken into account.

Bibliography

[1] ATLAS Collaboration. Observation of a new particle in the search for the standard model higgs boson with the ATLAS detector at the LHC. *Physics Letters B*, 716(1):1 – 29, 2012.

[2] S. Chatrchyan, V. Khachatryan, A.M. Sirunyan, A. Tumasyan, W. Adam, et al. Observation of a new boson at a mass of 125 gev with the CMS experiment at the LHC. *Physics Letters B*, 716(1):30 – 61, 2012.

[3] Carl D. Anderson. The Positive Electron. *Phys. Rev.*, 43:491–494, March 1933.

[4] web presence of CERN. http://home.web.cern.ch/about - accessed on December 24th 2014.

[5] Convention for the Establishment of a European Organization for Nuclear Research - Paris, July 1st, 1953. 41st Session of Council.

[6] Lyndon Evans and Philip Bryant. The CERN Large Hadron Collider: Accelerator and Experiments. *Journal of Instrumentation*, 3(S08001), August 2008.

[7] AC Team. The four main LHC experiments - CERN-AC-9906026. http://cds.cern.ch/record/40525 - accessed on March 18th 2015.

[8] ATLAS Collaboration. The ATLAS Experiment at the CERN Large Hadron Collider. *Journal of Instrumentation*, 3(S08003), 2008.

[9] Joao Pequenao. Computer generated image of the whole ATLAS detector - CERN-GE-0803012-05. http://cds.cern.ch/record/1095924 - accessed on March 18th 2015.

[10] Joao Pequenao. Computer generated image of the ATLAS inner detector. http://cds.cern.ch/record/1095926 - accessed on March 18th 2015.

[11] William R. Leo. *Techniques for Nuclear and Particle Physics Experiments.* Springer-Verlag, 2nd edition, 1994.

[12] Claus Grupen and Boris Schwartz. *Particle Detectors.* Cambridge University Press, 2nd edition, 2008.

[13] Joao Pequenao. Computer generated image of the ATLAS Muons subsystem - CERN-GE-0803017-01. http://cds.cern.ch/record/1095929 - accessed on March 19th 2015.

[14] ATLAS Muon Collaboration. *ATLAS Muon Spectrometer - Technical Design Report*, volume Issue 1; Revision 1. June 1997.

[15] LHC / HL-LHC Plan. https://cds.cern.ch/record/1975962/files/new_timeplan_24Sept2014_1_image.png - accessed on March 25th 2015.

[16] webpage of the ATLAS Shielding Project. http://atlas.web.cern.ch/Atlas/GROUPS/Shielding/shielding.htm#part6 - accessed on March 24th 2015.

[17] ATLAS TWiki - Muon Trigger Public Results. https://twiki.cern.ch/twiki/bin/view/AtlasPublic/MuonTriggerPublicResults - accessed on June 24th 2015.

[18] ATLAS TWiki - TriggerMenuVersions. https://twiki.cern.ch/twiki/bin/viewauth/Atlas/TriggerMenuVersions - accessed on June 24th 2015 (Access restricted to ATLAS members).

[19] ATLAS Collaboration. *ATLAS New Small Wheel - Technical Design Report.* June 2013.

[20] J. Bougher, D. Brown, T. Koi, P. Sherwood, D. Wright, et al. A Flugg-based Cavern Background Simulation Application. https://cds.cern.ch/record/1540319.

[21] Ralph Engel. Phojet manual. https://wiki.bnl.gov/eic/upload/Phoman5c-2.pdf.

[22] P.R. Sala and S. Vanini. Flugg homepage. http://www.fluka.org/content/tools/flugg/index.html - accessed on March 31st 2015.

[23] S. Agostinelli, J. Allison, K. Amako, J. Apostolakis, H. Araujo, et al. Geant4 - a simulation toolkit. *Nuclear Instruments and Methods in Physics Research Section A: Accelerators, Spectrometers, Detectors and Associated Equipment*, 506(3):250 – 303, 2003.

[24] Giuseppe Battistoni, Francesco Broggi, Markus Brugger, Mauro Campanella, Massimo Carboni, et al. FLUKA. Online manual. http://www.fluka.org/fluka.php?id=man_onl - accessed on March 31st 2015.

[25] T. Koi, S. Weber, and C. Young. New Small Wheel Shielding Simulation. ATLAS Note: ATL-MUON-INT-2013-010 (Access restricted to ATLAS members). https://cds.cern.ch/record/1629886?ln=de.

[26] T. Koi, D. Marley, M. Morinaga, S. Weber, and C. Young. New Small Wheel Background Studies. ATLAS Note: ATL-MUON-INT-2015-002 (Access restricted to ATLAS members). https://cds.cern.ch/record/2113242/?ln=de.

[27] Charles Young. New Small Wheel Background. Talk. https://indico.cern.ch/event/407980/contribution/8/attachments/1126146/1608542/New_JD_Shielding.pdf - accessed on August 28th 2015.

[28] Erick J. Weinberg and D. L. Nordstrom, editors. *Physical Review D - particles, fields, gravitation, and cosmology - Part 1 Review of Particle Physics*, volume 86 of *3*. American Physical Society, July 2012.

[29] ATLAS New Small Wheel Collaboration. Micromegas Construction Manual, July 2014. https://edms.cern.ch/document/1400217/1.

[30] Donald E. Groom, Nikolai V. Mokhov, and Sergei I. Striganov. Muon stopping power and range tables 10 MeV - 100 TeV. *Atomic Data and Nuclear Data Tables*, 76(2), July 2001. http://pdg.lbl.gov/2014/AtomicNuclearProperties/adndt.pdf.

[31] Particle Data Group. Atomic and Nuclear Properties of Materials for more than 300 materials. http://pdg.lbl.gov/2014/AtomicNuclearProperties/ - accessed on July 31st 2015.

[32] Saint-Gobain Ceramics & Plastics, Inc. Premium Plastic Scintillators. Data sheet. http://www.crystals.saint-gobain.com/uploadedFiles/SG-Crystals/Documents/SGC%20BC400-404-408-412-416%20Data%20Sheet.pdf - accessed on August 4th 2015.

[33] Hamamatsu Photonics K.K. Photomultiplier Tube Assemblies. Online catalog. http://www.hamamatsu.com/resources/pdf/etd/PMT_78-85_e.pdf - accessed on August 4th 2015.

[34] Hamamatsu Photonics K.K. Photomultiplier tube R6427, R7056. Data sheet. http://www.hamamatsu.com/resources/pdf/etd/R6427_R7056_TPMH1187E.pdf - accessed on August 4th 2015.

[35] Stefan Czerwenka. Simulation von Lichtausbreitung innerhalb eines Szintillators und Lichtleiters, December 2012. Bachelor thesis. Physik und ihre Didaktik, Julius-Maximilians Univerisität Würzburg.

[36] Lukas Haupt. Lichtausbreitung in Szintillatoren und Verarbeitung von Photomultipliersignalen, April 2013. Bachelor thesis. Physik und ihre Didaktik, Julius-Maximilians Univerisität Würzburg.

[37] Saint-Gobain Ceramics & Plastics, Inc. BC-600 Optical Cement. Data sheet. http://www.crystals.saint-gobain.com/uploadedFiles/SG-Crystals/Documents/SGC%20BC600%20Data%20Sheet.pdf - accessed on August 6th 2015.

[38] KENT Deutschland GmbH. MS Clear HS. Data sheet. http://www.kenteurope.com/pdf.php?file=wp-content/uploads/ds/de/85839 - accessed on August 6th 2015.

[39] Lucas Klein. Effizienzbestimmung von Szintillationsdetektoren und Messung der Myon-Lebensdauer, August 2015. Bachelor thesis. Physik und ihre Didaktik, Julius-Maximilians Univerisität Würzburg.

[40] Stefan Czerwenka. Aufbau eines Gassystems für Gasdetektoren im Rahmen eines Höhenstrahlungsteststandes, April 2015. Master thesis. Physik und ihre Didaktik, Julius-Maximilians Univerisität Würzburg.

[41] mesytec GMBH & Co. KG. MTDC-32 V2.6_01. Manual. http://www.mesytec.com/datasheets/MTDC-32.pdf.

[42] ROOT data analysis framework. webpage. https://root.cern.ch/ - accessed on October 19th 2015.

[43] TTree class reference. https://root.cern.ch/doc/master/classTTree.html - accessed on October 19th 2015.

[44] Robin Boshuis. Messung von Driftzeitspektren kosmischer Myonen, June 2015. Bachelor thesis. Physik und ihre Didaktik, Julius-Maximilians Univerisität Würzburg.

[45] CAEN Electronic Instrumentation. User's Manual - Mod. SY2527-SY2527LC, February 2012. http://www.caen.it/servlet/checkCaenManualFile?Id=8225 - accessed on September 29th 2015.

[46] CAEN Electronic Instrumentation. Technical Information Manual - Mod. A1535S-AG535S, June 2013. http://www.caen.it/servlet/checkCaenManualFile?Id=9315 - accessed on September 29th 2015.

[47] CAEN Electronic Instrumentation. Technical Information Manual - Mod. A1535D, June 2013. http://www.caen.it/servlet/checkCaenManualFile?Id=9327 - accessed on September 29th 2015.

[48] WIENER Plein & Baus GmbH. NIM / CAMAC Crates - User & Service Manual, December 2010. http://file.wiener-d.com/documentation/NIM-CAMAC/WIENER_NIM-CAMAC_Crates_Manual_A1.pdf - accessed on September 29th 2015.

[49] CAEN Electronic Instrumentation. Technical Information Manual - Mod. N842-N843, July 2011. http://www.caen.it/servlet/checkCaenManualFile?Id=7720 - accessed on September 29th 2015.

[50] CAEN Electronic Instrumentation. Technical Information Manual - Mod. N93B, August 1991. http://www.caen.it/servlet/checkCaenManualFile?Id=5239 - accessed on September 29th 2015.

[51] Phillips Scientific. Octal Multifunction Logic Unit - NIM MODEL 757. data sheet. http://phillipsscientific.com/pdf/757ds.pdf - accessed on September 29th 2015.

[52] WIENER Plein & Baus GmbH. WIENER Mini Crate 395 - User Manual, June 2013. http://file.wiener-d.com/documentation/Crates_395/WIENER_395-mini-crate_v1.pdf - accessed on September 29th 2015.

[53] WIENER Plein & Baus GmbH. VM-USB - User Manual, November 2011. http://file.wiener-d.com/documentation/VM-USB/WIENER_VM-USB_Manual_9.03.1.pdf - accessed on September 29th 2015.

[54] Photograph by Dominik Köth, 2014.

List of Figures

All figures, graphics and photos not specifying a source are created by the author of this thesis.

Acknowledgments

Experimental high-energy particle physics is a very cooperative field of science. And also this thesis was not carried out behind closed doors. Therefore I want to thank all people, that contributed to this work in any manner.

First of all I want to thank my supervisor **Professor Raimund Ströhmer**. He gave me the opportunity to work on interesting topics and to build by myself a lab completely from scratch. Furthermore he was always happy to answer any question, to give good advise and to point out additional aspects, I did not think of. I want to thank the chair holder **Professor Thomas Trefzger**, too, for giving me the feeling of being very welcome in the group. I am very happy, that **Professor Matthias Schott**[1] and **Professor Werner Porod** agreed to be second and third assessor.

I am very thankful, that I always had somebody to ask, when needed. **Charles Young**[2] advised me very well on the background simulation topic. He introduced me patiently into this subject, that was new to me. **Giovanni Siragusa** and **André Zibell** gave me a lot of helpful advises on computing, electronics and physics in general during my time in the group.

Diverse discussions and help with small everyday problems were not less relevant for sure. I want to thank my colleagues **Manuel Schreyer**, **Jason Tam**, **Jochen Meyer** and **Verena Herget** for these discussions and help.

The test facility is designed to serve a lot of different purposes. Consequently several people already worked on the facility and even more will hopefully follow. Therefore I want to thank the Bachelor and Master students, working on the facility with me, for their share of the overall project. Especially I want to mention **Lucas Klein**, **Lukas Haupt**, **Robin Boshuis** and **Stefan Czerwenka**, whose works are partly reflected in this thesis.

[1] Johannes Gutenberg-Universität, Mainz, Germany
[2] SLAC National Accelorator Labroratory, Stanford, USA

Some aspects of the hardware part of the thesis were not possible to achieve without the assistance of additional helping hands. The student assistants **Dominik Köth** and **Jonathan Hohm** helped me enthusiastically to build the detectors. The **scientific workshops** of the Faculty of Physics and Astronomy of the University of Würzburg provided support for the project throughout tho whole time and built several components for the facility. I thank the assistants as well as the members of the workshop to enable me to construct the facility.

Purchasing components for the build-up of a lab at a German university includes a lot of administrative paperwork. I want to express my thanks to our secretaries **Karin Kuhns** and **Anna Weisensel** taking over a considerable part of that work, besides the usual administrative work they did for me.

I also want to thank all the members of the group of Physics and its Didactics. They contributed to a pleasant working atmosphere all the time. But even more they were always willing to help, no matter if they were members of the didactic or the particle physics subgroup. When, for example, the two tons of steel plates for the absorber had to be transported into the lab by hand, the whole group helped without complaining, even though that was not part of their job descriptions for sure.

Proofreading is a very important task, but also a very time consuming one. Therefore I want to point this out explicitly, though they were already mentioned before. I thank for proofreading: **André Zibell**, **Jochen Meyer** and **Verena Herget**.

Finally, I want to thank all those friends and colleagues, that I met throughout the years and I did not mention yet, for a lot of fascinating discussions on and around the topic.